MASTER

Formation of satellite droplets in dip-coating of well-defined heterogeneities on homogeneous hydrophobic substrates

van Gestel, M.A.C.

Award date:
2018

Technische Universiteit
Eindhoven
University of Technology

Department of Applied Physics
Fluid Dynamics
Mesoscopic Transport Phenomena
Building: Cascade
P.O. Box 513
5600 MB Eindhoven

Formation of satellite droplets in dip-coating of well-defined heterogeneities on homogeneous hydrophobic substrates

M.A.C. van Gestel, BSc.

December 3, 2018

Supervisors:
Prof. dr. A.A. Darhuber
Ir. B. He
Ir. J. Fonseca

Abstract

Consider the deposition of a film of Newtonian liquid on a flat plate being withdrawn from a liquid reservoir. The deposition only occurs above a critical velocity of the plate. This critical velocity solely depends on the contact angle and liquid parameters. When deposition is unwanted, while moving below the critical velocity such as in immersion lithography, small surface defects or heterogeneities can pin the contact line locally. The formation of residual satellite droplets underneath these surface defects is then caused by the break up process as well as the subsequent meniscus retraction. These satellite droplets can cause printing defects in the photo-lithography process.

Therefore the formation of satellite droplets in dip-coating of well-defined heterogeneities (patterns) on homogeneous substrates is studied using experimental work as well as numerical modelling. It is shown that the geometrical parameters of the pattern are the dominant factor in this process. The pinning feature of the contact line is influenced by the maximum slope of the pattern while the size of the satellite droplets depends on the geometrical parameters of the pattern, contact angle distribution and dip-coating velocity. The biggest satellite droplet radius and distance from the pattern edge scales roughly linear with the pattern dimension for pattern dimensions below the capillary length. For higher pattern dimensions a decrease in dependence is observed for decreasing dip-coating velocities. The biggest satellite droplet radius and distance from the pattern edge scales with the dip-coating velocity as a power law for small dip-coating velocities and small pattern dimensions, i.e. pattern dimensions smaller than capillary length. For increasing dip-coating velocities closer to the critical value exponential increase is observed. Although the experiments and numerical simulations show many similarities between the break up dynamics, the observed scaling is not reproduced. Possible causes for this are the differences in pattern dimension, contact angle distribution and smaller pattern slope and capillary numbers. The influence of pattern shape is studied experimentally by comparing between equilateral triangles, squares and circles. Equilateral triangles and square patterns leave bigger satellite droplets at a larger distance for the same dip-coating velocities and pattern dimensions compared to circular patterns. Both experimentally and numerically the trail of droplets decays in size following a power law with increasing scaling magnitude for decreasing dip-coating velocities. The total waterloss, i.e. the total volume of satellite droplets, scales similar with the dip-coating velocity compared to the the biggest satellite droplet.

Contents

Chapter 1

Introduction

Gordon Moore predicted the exponential growth of the number of transistors on an integrated circuit in 1965 [1]. The prediction, although only an extrapolation at that time, is well known as Moore's law today. So far this empirical prediction holds and is even used in the semiconductor industry to guide long-term planning [2]. The technique used to produce state-of-the-art integrated circuits, which are also known as microchips, is called *photo-lithography*.

A photo-lithography machine consists of three stages, as sketched in figure 1.1. First a light source, i.e. laser, produces the light used in the machine. In the second stage the light is transmitted through the reticle stage. In this stage the light is reflected from a plate, the reticle, in a defined pattern. In the third stage this pattern is then projected onto the silicon wafer stage where the actual microchips are produced.

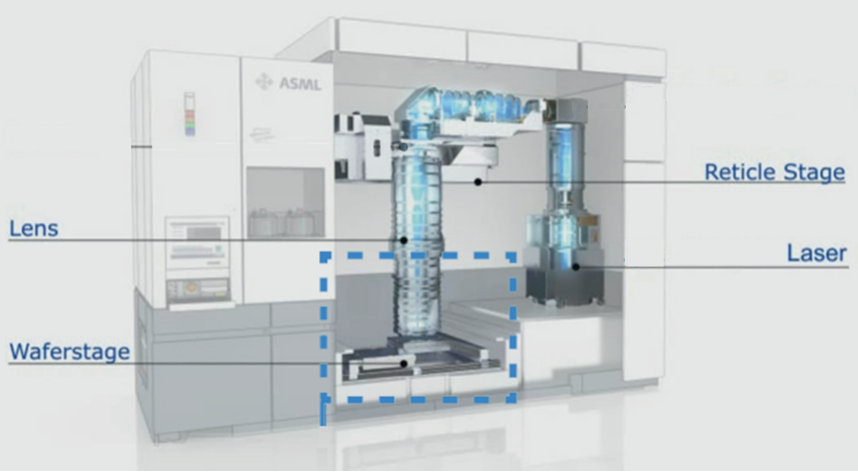

Figure 1.1: Schematic image of photo-lithography machine with three main stages highlighted. Image adjusted from Winkels [3].

Progress in the semiconductor industry is all about reducing the size of the components inside a microchip. Smaller components result in faster microchips that consume less power [4]. The smallest feature size a photo-lithography system can produce is set by the critical dimension CD of the optical expose system:

$$CD = k_1 \frac{\lambda}{n_1 \sin \phi} = k_1 \frac{\lambda}{NA}, \tag{1.1}$$

with k_1 a system dependent pre-factor, λ the wavelength of the light, ϕ the limiting angle of the lens, n_1 the index of refraction, and NA the numerical aperture of the imaging system. The

latter is an optical property taking into account how well the light is projected onto the silicon wafer. There are several ways to reduce the critical dimension CD. The first way is decrease the wavelength of the light being used, such as done in the new generation of photo-lithography machines where the wavelength decreased from deep ultraviolet (DUV) with $\lambda = 193$ nm to extreme ultra violet (EUV) with $\lambda = 13.5$ nm [5], [6].

Second is *immersion lithography*, where the critical dimension CD is refined by inserting a high index liquid $n_1 > 1$ into the gap between the lens and wafer surface which increases numerical aperture NA [7], [8]. Combined with multiple-patterning techniques the resolution can improve to sub 10 nm [9], [10].

1.1 Challenges in Immersion lithography

In current immersion lithography machines a layer of water ($n_1 = 1.44$) replaces the air ($n_1 = 1$) between the lens and wafer which increases the numerical aperture NA and enables to print smaller features. The water is confined inbetween the immersion hood and the wafer, with a distance of $\sim 100\,\mu$m apart, as illustrated in figure 1.2. Although the layer of water increases the resolution it also gives rise to several challenges. Due to the high throughput demanded by the industry the wafer moves with speeds up to ~ 1 m/s which induces large shear forces while any non-uniformities in the water may result in printing defects. These non-uniformities have a variety of causes such as imported particles [9], [11], chemical leaching of the photoresist [12]–[15], bubbles [16], and inhomogeneous heating [17].

Another challenge in immersion lithography is *film pulling*, which is illustrated in figure 1.2. Film pulling occurs either at the edge of the wafer or when contamination is present on the wafer. Both times the contact line pins on macroscopic level and a film is pulled [figure 1.2(a-b)]. When this film breaks, it leaves small droplets on the wafer [figure 1.2(c)]. These small droplets, depending on size and location, can cause printing defects [18], [19]. The residual droplets can cause printing defects in three ways [20]:

(i) watermarks due to the interaction between local photoresist and residual droplets [21], [22],

(ii) drying stains from materials dissolved in water while residual droplets evaporate [23],

(iii) bubbles from residual droplets impinging the advancing meniscus [16].

One way to reduce the number of defects in immersion lithography is to minimize the waterloss, i.e. keep a stable meniscus throughout the scanning process. Several studies for meniscus stability have been done. Investigation of the critical velocity, for which entrainment occurs even without contamination or the edge of the wafer, shows that an increase in static receding contact line increases the critical velocity [19], [24]. In current immersion hoods the waterloss is minimized by the use of air jets [25] or optimizing the water flows [26], which will both not be considered in this study. Other studies on meniscus stability focus on the formation of a corner tip instability [27], surface roughness on the wafer to increase the critical velocity [28] or study liquid entrainment for example by use of dip-coating [29]–[31].

In dip-coating a plate is vertically withdrawn from a liquid reservoir. In this study dip-coating of partially-wetting substrates is used to investigate the influence of heterogeneities (or defects) on the pinning of the contact line and the formation of residual (or satellite) droplets.

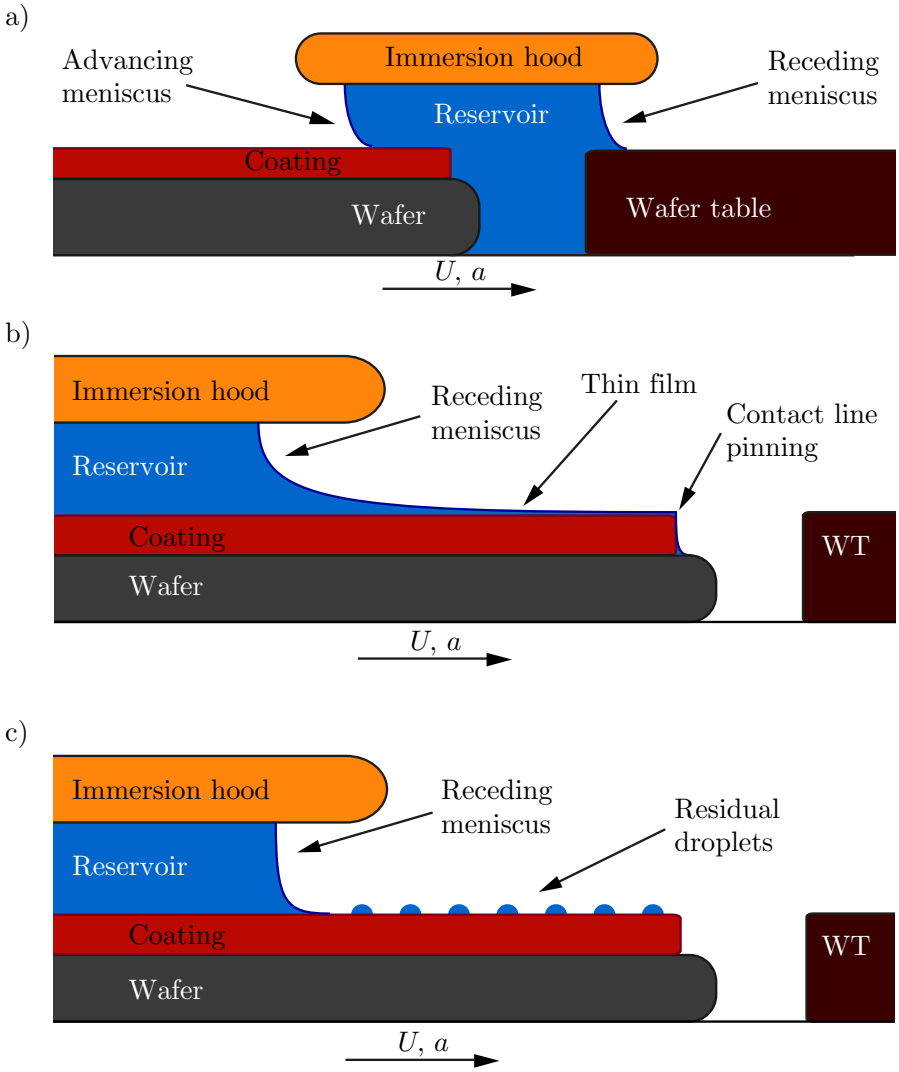

Figure 1.2: Illustration of film pulling in immersion lithography. The immersion hood confines the water between the immersion hood and the wafer. When the wafer moves with a velocity U the reservoir has an advancing and receding meniscus (a). The contact line pins on the edge of the wafer and a thin film is pulled (b). When the wafers moves further this thin film breaks up in tiny droplets (c).

1.2 Dimensional analysis

Dip-coating (DC) of partially wetting substrates from a viscous, non-volatile liquid (glycerol-water solution) is used to investigate the influence of defects on film pulling and then compared to immersion lithography where water is used. This liquid is chosen for practial reasons such as slow evaporation rate and slower break-up, by which the dynamics can be captured by a camera. A dimensional analysis according to Buckingham-π-theorem [32] gives the number of dimensionless parameters by $p' = n' - k'$ with p' the number of dimensionless parameters, n' the number of physical variables and k' the number of physical dimensions. Taking into account the fluid density ρ, the surface tension γ, the dynamic viscosity μ, the relevant length scale L_0, substrate scan velocity U, and gravitational acceleration g gives $n' = 6$ physical variables. The experiment is conducted in $k' = 3$ physical dimensions (length, mass and time) which leads to $p' = 3$ dimensionless parameters. The first dimensionless parameter is the Reynolds number:

$$Re = \frac{\rho U L_0}{\mu} \tag{1.2}$$

which compares fluid inertia to viscous forces. The second dimensionless parameters is the Bond number

$$Bo = \frac{\rho g L_0^2}{\gamma} \tag{1.3}$$

which compares gravitational forces and surface tension forces. The third dimensionless parameter is the capillary number:

$$Ca = \frac{\mu U}{\gamma} \tag{1.4}$$

which relates the viscous forces to the surface tension forces. Although there are several relevant length scales L_0, such as the initial film height, gap height of wafer-immersion hood, the defect sizes and the capillary length, the latter is used in this dimensional analysis. The capillary length l_c relates the capillary pressure to the hydrostatic pressure and is defined by:

$$l_c = \sqrt{\frac{\gamma}{\rho g}}. \tag{1.5}$$

The physical variables and the resulting dimensionless parameters are given for both typical industrial immersion (water) conditions and dip-coating (glycerol-water solution) in table 1.1.

Table 1.1: Parameters for film pulling under typical industrial immersion (water) conditions [9] and dip-coating (glycerol-water solution). The physical parameters taken into account for the dimensionless analysis according to Buckingham-π-theorem are shown.

parameter	unit	immersion (water)	dip-coating (glycerol-water)
ρ	liquid density [kg/m^3]	$\mathcal{O}(10^3)$	$\mathcal{O}(10^3)$
γ	surface tension [kg/m^3]	$\mathcal{O}(0.1)$	$\mathcal{O}(0.1)$
μ	dynamic viscosity [kg/ms]	$\mathcal{O}(10^{-3})$	$\mathcal{O}(0.1)$
L_0	Relevant length scale [m]	$\mathcal{O}(10^{-3})$	$\mathcal{O}(10^{-3})$
U	scan velocities [m/s]	$\mathcal{O}(0.1 \rightarrow 1)$	$\mathcal{O}(10^{-4} \rightarrow 10^{-3})$
g	gravitational acceleration [m/s^2]	$\mathcal{O}(10)$	$\mathcal{O}(10)$
Re	Reynolds number	$\mathcal{O}(10^2 \rightarrow 10^3)$	$\mathcal{O}(10^{-3} \rightarrow 10^{-2})$
Bo	Bond number	$\mathcal{O}(0.1)$	$\mathcal{O}(0.1)$
Ca	Capillary number	$\mathcal{O}(10^{-3} \rightarrow 10^{-4})$	$\mathcal{O}(10^{-4} \rightarrow 10^{-3})$

Chapter 2

Theory of film pulling

The moving meniscus can pin on the edge of the wafer or on possible contamination. A film is pulled and eventually breaks up in droplets possibly causing the printing defects in the photo-lithography process. In this chapter the theory needed to describe the film pulling and break up is discussed. First the conservation laws for fluid dynamics are given in section 2.1. In section 2.2 surface tension is discussed. Next in section 2.3 the solid-liquid interaction is discussed. When these two interfaces are separated by a distance h, an additional force per unit area arises. This disjoining pressure is discussed in section 2.4. In section 2.5 the thin film equation or lubrication approximation is derived from the Navier-Stokes equations. Next in section 2.6 dip-coating of flat surfaces and its boundary conditions for the solid-liquid-vapour system are implemented and derived scaling relations are discussed. Dip-coating of defects on flat surfaces is discussed in section 2.7.

2.1 Conservation laws

A fluid consists of molecules in constant motion and interactions with each other, and is therefore discrete at molecular scales. In many systems however macroscopic quantities are studied by applying conservation laws assuming a continuum, where the discrete molecular motion is assumed to behave as a continuous distribution. This assumption is valid for small Knudsen numbers $Kn = \lambda'/L_0 \ll 1$, with λ' the mean free path and L_0 the physical length scale. For a Knudsen number approaching or greater than one, the continuum assumption is no longer a good approximation and statistical methods should be used [32]. Taking the approximation for the film thickness from figure 1.2 as the physical length scale $L_0 \approx 5$ μm and the intermolecular spacing as an approximation for the mean free path $\lambda' \approx 2.5$ Å gives a Knudsen number $Kn \sim 10^{-5} \ll 1$. Thus the continuum approximation is valid and conservation laws can be used without having to consider molecular motion. Three conservation laws can be used to solve fluid dynamics problems, namely:

(i) conservation of mass, which in differential form is given by:

$$\frac{\partial \rho}{\partial t} + \nabla \cdot (\rho \mathbf{u}) = 0, \tag{2.1}$$

with ρ the density of the fluid, t the time and $\mathbf{u}$ the velocity vector. The liquids can be assumed to be incompressible (constant density ρ) which simplifies equation (2.1):

$$\nabla \cdot \mathbf{u} = 0. \tag{2.2}$$

(ii) conservation of momentum in three dimensions (3D):

$$\frac{\partial \rho \boldsymbol{u}}{\partial t} + \nabla \cdot (\rho \boldsymbol{u}\boldsymbol{u}) = \rho \boldsymbol{f} - \nabla p + \nabla \cdot \bar{\bar{\tau}}, \tag{2.3}$$

with $\boldsymbol{f}$ the vector containing body forces such as gravity, p the pressure, and $\bar{\bar{\tau}}$ the viscous stress tensor. Filling in the assumption for an incompressible flow and assuming the considered fluids behave as Newtonian fluids, i.e. the viscous stresses scale linear proportional to the local strain rate, results in:

$$\rho \left(\frac{\partial \boldsymbol{u}}{\partial t} + \boldsymbol{u} \cdot \nabla \boldsymbol{u} \right) = -\nabla P + \mu \nabla^2 \boldsymbol{u} = \nabla p + \rho \boldsymbol{g} + \mu \nabla^2 \boldsymbol{u}, \tag{2.4}$$

where P represents the total pressure including body-forces and μ the dynamic viscosity.

(iii) conservation of energy, which will not be taken into account in this study.

2.2 Surface Tension

A liquid is a condensed state in which molecules attract one another. Typically these microscopic cohesion forces contributing to the surface tension are van der Waals forces and hydrogen bonds. A molecule located in the bulk of the fluid feels these cohesive forces from neighbours in all directions evenly. In contrast, a molecule at the surface loses half of its cohesive interactions as illustrated in figure 2.1(a). This is the fundamental reason that a liquid minimizes its shape as much as possible. Dry sand at the beach for example does not stick together, whereas the moment it gets wet it does. The surface tension γ $[N/m]$ is a macroscopic parameter related to the molecular shortfall of cohesion forces at the surface. Macroscopically surface tension can be seen as the energy needed to increase the surface area by one unit or as the force per unit length.

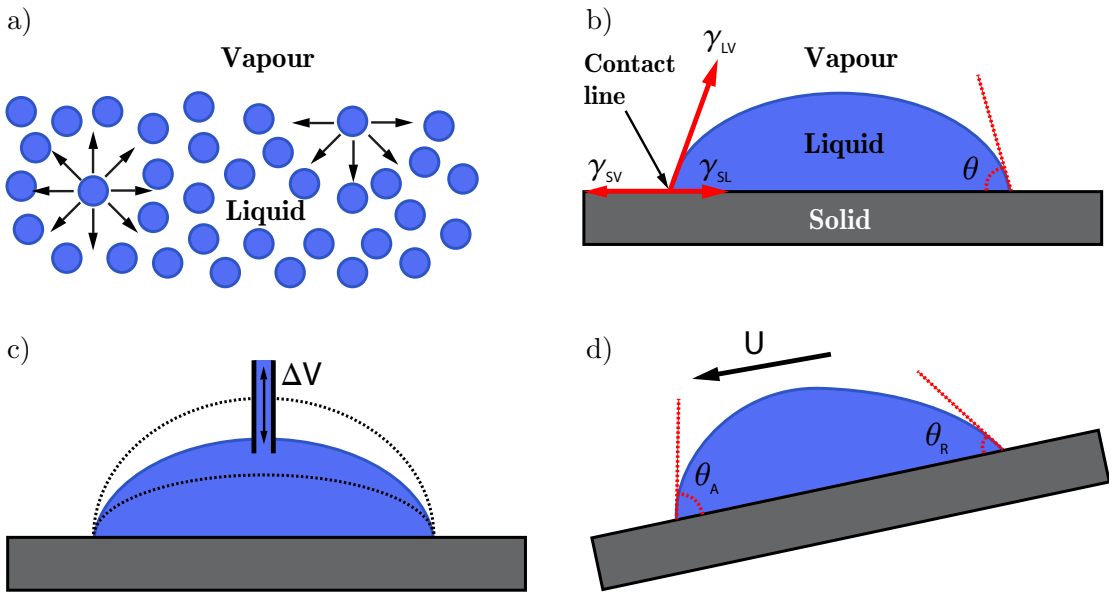

Figure 2.1: (a) Schematic representation of the molecular origin of surface tension. (b) Droplet on a solid illustrating the balance of cohesive versus adhesive forces results in the contact angle θ between the liquid-vapour and solid-liquid interfaces. (c-d) Droplets with changing contact angles due to a change in volume or a sliding droplet on a non-flat solid.

An important consequence of surface tension is the overpressure it creates in fluids trying to minimize their surface. The increase in pressure Δp when crossing the boundary between two

fluids is given by [33]:

$$\Delta p = \gamma \cdot \left(\frac{1}{R_1} + \frac{1}{R_2} \right), \tag{2.5}$$

with $C = \left(\frac{1}{R_1} + \frac{1}{R_2} \right)$ the curvature, R_1 and R_2 the radii of curvature of the surface. The increase in pressure Δp is also known as the Laplace pressure, named after the physicist who first described this phenomenon.

2.3 Wetting and hysteresis

After describing the molecular origin of why a fluid always wants to minimize its surface energy now the physics of a droplet on a substrate, i.e. sessile droplet, is described. The three phases liquid, vapour and solid meet at the contact line of the droplet, indicated in figure 2.1(b). The shape of the droplet is determined by the balance between cohesive forces of the liquid itself and the adhesive forces between the liquid-solid interface. Under ideal circumstances this leads to single contact angle θ describing the angle between the solid and the liquid-vapour interface at the contact line as described by Young's law[34]:

$$\gamma_{LV} \cos\theta = \gamma_{SV} - \gamma_{SL}. \tag{2.6}$$

Where the capillary forces γ of the solid-vapour (SV), liquid-vapour(LV) and solid-liquid(SL) acting on the contact line are balanced. Throughout the thesis the liquid-vapour surface tension will be denoted as γ. The balance describes how a liquid will spread when it is deposited on a surface. Two regimes of spreading are observed, namely total wetting and partial wetting. Where total wetting corresponds to a contact angle of $\theta = 0^o$ and partial wetting to $\theta > 0^o$. Partial wetting is subdivided in hydrophilic surfaces $0 < \theta < 90^o$ and hydrophobic surfaces $90 < \theta < 180^o$.

In many non-ideal physical situations the contact angle θ can assume a range of values due to heterogeneities in the surface on nanoscale $\mathcal{O}\left(10^{-9}\, m\right)$ [35]. These heterogeneities can have a chemical and physical component corresponding to inhomogeneities in contact angle θ or substrate topography. The variation in contact angle θ is illustrated in two situations in figure 2.1(c). The volume of a droplet is changed by a hollow needle. This change in volume changes the contact angle up to a critical value while the contact line is pinned. When increasing the volume beyond this critical value the contact line starts to move and the observed contact angle is called the advancing contact angle θ_A. In a similar way, decreasing the volume beyond the critical value yields a receding contact angle θ_R. The contact angles at the critical value, i.e. just before the contact line moves, are called the static advancing and receding contact angles. The difference in contact angle is defined as contact angle hysteresis $\Delta\theta$:

$$\Delta\theta = \theta_R - \theta_A. \tag{2.7}$$

The same difference in contact angle is observed in 2.1(d), where a droplet sliding with constant velocity U on a surface is illustrated. The dynamics of the contact angle θ is described by Cox-Voinov law [36]:

$$\theta^3 = \theta_0^3 \pm 9\gamma Ca \ln x/l', \tag{2.8}$$

with $\theta_R \leq \theta \leq \theta_A$ the dynamic contact angle, θ_0 the equilibrated contact angle and l' the molecular scale where the discrete character of the molecules becomes noticeable. The plus corresponds to the advancing contact lines and the minus to the receding contact lines.

2.4 Disjoining pressure

The disjoinining pressure $\Pi(h)$ is an additional force per unit area, which refers to all contributions to the pressure between two interfaces separated by a distance h, other than the hydrostatic

and capillary ones. These contributions can be divided in molecular, ionic-electrostatic, and structural components. The disjoining pressure is related to the Gibbs free energy G, according to the definition:

$$\Pi = -\frac{\partial G}{\partial h}, \tag{2.9}$$

and can be either attractive or repulsive depending on the film thickness h and material. In this study a phenomenological model composed of a long-range attractive and short-range repulsive potential is used [37]:

$$\Pi = \gamma\,(1-\cos\theta)\cdot\frac{(n-1)(m-1)}{n-m}\frac{1}{h^*}\left[\left(\frac{h^*}{h}\right)^n-\left(\frac{h^*}{h}\right)^m\right], \tag{2.10}$$

with n and m two constants and h^* the precursorlayer thickness. The Navier-Stokes equations do not allow liquid motion to or from perfectly dry regions of the substrate due to the stress singularity associated with a moving contact line. This is caused by the incompatibility between the usual no-slip condition, where the liquid meets the substrate, and the boundary condition on the liquid-vapour interface. This leads to the stress singularity where these two interfaces meet, i.e. the contact line. The wetting- or precursorlayer h^* regularizes this stress singularity associated with a moving contact line. An alternative model for the disjoining pressure is for example the diffusive interface model by Thiele et al [38], [39]. which assumes that interfaces have a non-zero thickness.

2.5 Theory of thin liquid films

In this section the theory to model the evolution of a thin liquid film on a solid substrate is discussed. Starting point are the Navier-Stokes equations (2.4) for an incompressible, Newtonian liquid and the continuity equation (2.2). Consider a thin film on a solid substrate with thickness profile $h(x,y,t)$ in the order of typical scale H, as illustrated in figure 2.2. The length scales L over which the film is stretched in the x and are y direction are much larger than the typical thickness H, i.e. the aspect ratio $\epsilon = H/L \ll 1$. Consequently, the interface slopes are small, $\left[\frac{\partial h}{\partial x}\right] = \left[\frac{\partial h}{\partial y}\right] \sim \frac{H}{L} = \epsilon \ll 1$.

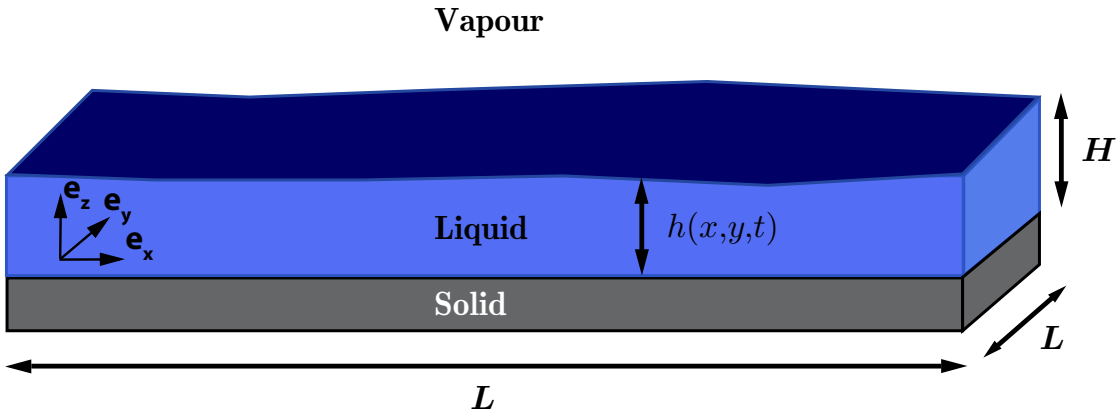

Figure 2.2: Illustration of a thin liquid film with thickness profile $h(x,y,t)$ on a solid substrate.

The following non-dimensional variables are introduced:

$$(\bar{x},\bar{y},\bar{z}) = \left(\frac{x}{L},\frac{y}{L},\frac{z}{H}\right), \quad (\bar{u},\bar{v},\bar{w}) = \left(\frac{u}{U},\frac{v}{U},\frac{w}{V}\right), \quad \bar{t} = \frac{U}{L}t, \quad \text{and} \quad \bar{P} = \frac{H^2}{\mu U L}P. \tag{2.11}$$

where U and V correspond to the velocity scales in and out of the xy-plane, respectively. The velocity components in the x, y and z direction are represented by u, v and w, respectively. Scaling the continuity equation with these non-dimensional variables gives:

$$\frac{U}{L}\frac{\partial \bar{u}}{\partial \bar{x}} + \frac{U}{L}\frac{\partial \bar{v}}{\partial \bar{y}} + \frac{V}{H}\frac{\partial \bar{w}}{\partial \bar{z}} = 0, \tag{2.12}$$

where now each term must be of comparable magnitude. This implies that the out of xy-plane velocity scale is related to the in xy-plane velocity scale as $V \sim \epsilon U$. Thus the horizontal velocity in the x and y directions is much higher than the typical vertical velocity in the z direction. The non-dimensionalized Navier-Stokes equations become:

$$\epsilon Re_H \left(\frac{\partial \bar{u}}{\partial \bar{t}} + \bar{u}\frac{\partial \bar{u}}{\partial \bar{x}} + \bar{v}\frac{\partial \bar{u}}{\partial \bar{y}} + \bar{w}\frac{\partial \bar{u}}{\partial \bar{z}} \right) = -\frac{\partial \bar{P}}{\partial \bar{x}} + \frac{\partial^2 \bar{u}}{\partial \bar{z}^2} + \epsilon^2 \left(\frac{\partial^2 \bar{u}}{\partial \bar{x}^2} + \frac{\partial^2 \bar{u}}{\partial \bar{y}^2} \right), \tag{2.13}$$

$$\epsilon Re_H \left(\frac{\partial \bar{v}}{\partial \bar{t}} + \bar{u}\frac{\partial \bar{v}}{\partial \bar{x}} + \bar{v}\frac{\partial \bar{v}}{\partial \bar{y}} + \bar{w}\frac{\partial \bar{v}}{\partial \bar{z}} \right) = -\frac{\partial \bar{P}}{\partial \bar{y}} + \frac{\partial^2 \bar{v}}{\partial \bar{z}^2} + \epsilon^2 \left(\frac{\partial^2 \bar{v}}{\partial \bar{x}^2} + \frac{\partial^2 \bar{v}}{\partial \bar{y}^2} \right), \tag{2.14}$$

$$\epsilon^3 Re_H \left(\frac{\partial \bar{w}}{\partial \bar{t}} + \bar{u}\frac{\partial \bar{w}}{\partial \bar{x}} + \bar{v}\frac{\partial \bar{w}}{\partial \bar{y}} + \bar{w}\frac{\partial \bar{w}}{\partial \bar{z}} \right) = -\frac{\partial \bar{P}}{\partial \bar{z}} + \epsilon^2 \frac{\partial^2 \bar{w}}{\partial \bar{z}^2} + \epsilon^4 \left(\frac{\partial^2 \bar{w}}{\partial \bar{x}^2} + \frac{\partial^2 \bar{w}}{\partial \bar{y}^2} \right), \tag{2.15}$$

for the x,y and z component, respectively. The Reynolds number $Re_H = \rho U H/\mu$ is based on the film height and is assumed to be small ($Re_H \ll 1$). Since the liquid films are characterized by small Re_H and aspect ratio ϵ the terms with ϵ^2 and ϵRe_H can be neglected, which reduces the Navier-Stokes equations to:

$$\mu \frac{\partial^2 u}{\partial z^2} = \frac{\partial P}{\partial x}, \tag{2.16}$$

$$\mu \frac{\partial^2 v}{\partial z^2} = \frac{\partial P}{\partial y}, \tag{2.17}$$

$$\frac{\partial P}{\partial z} = 0, \tag{2.18}$$

in the so-called lubrication approximation for the x,y and z component, respectively. Equation (2.18) indicated the pressure $P(x, y)$ is independent of z. The next step is the implementation of the boundary conditions depending on what system is studied, for example a solid-liquid-solid or solid-liquid-vapour system.

2.6 Dip-coating of flat surfaces

A sketch of the dip-coating system is given in figure 2.3(b) where the solid moves with constant velocity U in the y-direction. Now first the boundary conditions and derivation of the lubrication equation for this dip-coating system, i.e. solid-liquid-vapour system, are discussed.

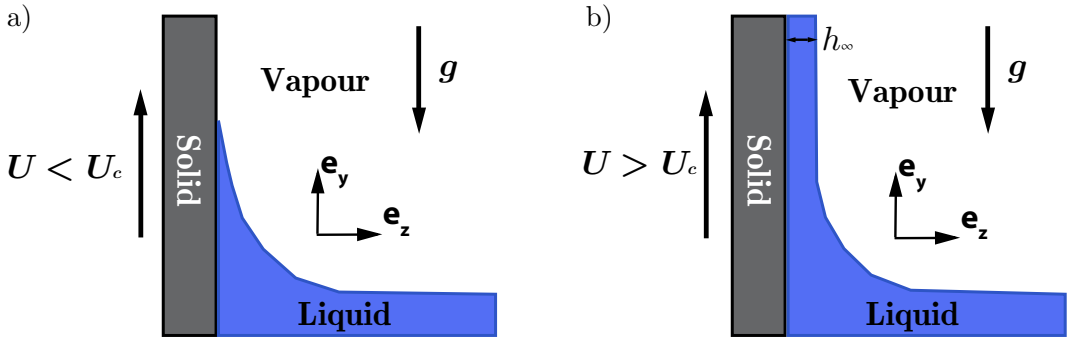

Figure 2.3: Sketch of the dip-coating system for a partial wetting liquid $\theta > 0^o$. For small dip-coating velocities (a) a stable meniscus is formed and there is no entrainment or film pulling. For large dip-coating velocities (b) liquid entrains and a film is pulled.

At the solid-liquid interface a no-slip and no-penetration boundary condition is assumed, setting the velocity components:

$$\boldsymbol{u}(z=0) = (0, U, 0). \tag{2.19}$$

At the liquid-vapour interface, $z = h(x, y, t)$ the boundary conditions is set by the stress balance:

$$p_{vap} - p - \boldsymbol{n_i} \cdot \left(\bar{\bar{\boldsymbol{T}}}_{\boldsymbol{liq}} - \bar{\bar{\boldsymbol{T}}}_{\boldsymbol{vap}} \right) \cdot \boldsymbol{n_i} + \gamma \boldsymbol{n_i} \left(\nabla \cdot \boldsymbol{n_i} \right) = 0, \tag{2.20}$$

$$\boldsymbol{t_i} \cdot \left(\bar{\bar{\boldsymbol{T}}}_{\boldsymbol{liq}} - \bar{\bar{\boldsymbol{T}}}_{\boldsymbol{vap}} \right) \cdot \boldsymbol{n_i} + \boldsymbol{t_i} \cdot \nabla_s \gamma = 0, \tag{2.21}$$

normal and tangential to the interface, respectively. Furthermore $\boldsymbol{n_i}$ and $\boldsymbol{t_i}$ are the normal and tangential unit vectors. The liquid and vapour stress tensors are represented by $\bar{\bar{\boldsymbol{T}}}_{\boldsymbol{liq}}$ and $\bar{\bar{\boldsymbol{T}}}_{\boldsymbol{vap}}$, respectively. In both directions the stress in the vapour can be neglected due to the viscosity contrast ($\mu_{vap} \ll \mu_{liq} = \mu$) with the liquid. Filling in the liquid stress tensors and again simplifying by sorting out the dominant terms with $\epsilon \ll 1$ gives:

$$p = p_{vap} + \rho g y - \gamma \left(\frac{\partial^2 h}{\partial x^2} + \frac{\partial^2 h}{\partial y^2} \right) = 0, \tag{2.22}$$

for the normal stress boundary condition on the liquid-vapour interface and

$$\mu \frac{\partial u}{\partial z} (z = h) = \frac{\partial \gamma}{\partial x} \quad \text{and} \quad \mu \frac{\partial v}{\partial z} (z = h) = \frac{\partial \gamma}{\partial y}, \tag{2.23}$$

for the tangential stress boundary condition. The hydrostatic pressure is represented by $\rho g y$. Integrating the x and y component of the lubrication equations (2.16) and (2.17) gives:

$$u = \frac{1}{\mu} \frac{\partial P}{\partial x} \frac{z^2}{2} + z f_1(x, y, t) + g_1(x, y, t), \tag{2.24}$$

$$v = \frac{1}{\mu} \frac{\partial P}{\partial y} \frac{z^2}{2} + z f_2(x, y, t) + g_2(x, y, t), \tag{2.25}$$

for the x and y component of the velocity, respectively. The pressure is independent of z thus equal to its value at the liquid-vapour interface, $P = \rho g y - \gamma \left(\frac{\partial^2 h}{\partial x^2} + \frac{\partial^2 h}{\partial y^2} \right)$. Now implementing the derived boundary conditions to find the integration parameters f and g yields:

$$u = \frac{1}{\mu} \frac{\partial P}{\partial x} \left(\frac{z^2}{2} - hz \right) + \frac{1}{\mu} \frac{\partial \gamma}{\partial x} z, \tag{2.26}$$

$$v = \frac{1}{\mu} \frac{\partial P}{\partial y} \left(\frac{z^2}{2} - hz \right) + \frac{1}{\mu} \frac{\partial \gamma}{\partial y} z + U. \tag{2.27}$$

From these expressions for velocity components u and v the volume fluxes Q_x and Q_y can be determined by integrating over the film height:

$$Q_x = \int_0^h u dz = -\frac{1}{3\mu} \frac{\partial P}{\partial x} h^3 + \frac{h^2}{2\mu} \frac{\partial \gamma}{\partial x} \tag{2.28}$$

$$Q_y = \int_0^h v dz = -\frac{1}{3\mu} \frac{\partial P}{\partial y} h^3 + \frac{h^2}{2\mu} \frac{\partial \gamma}{\partial y} + Uh. \tag{2.29}$$

The volume fluxes can be combined with the continuity equation (2.2) by integrating over the local film thickness h:

$$\int_0^h \left(\frac{\partial u}{\partial x} + \frac{\partial v}{\partial y} + \frac{\partial w}{\partial z} \right) dz = 0. \tag{2.30}$$

Now using the integration rule of Leibniz yields:

$$\frac{\partial Q_x}{\partial x} + \frac{\partial Q_y}{\partial y} - \frac{\partial h}{\partial x}u(h) - \frac{\partial h}{\partial y}v(h) + w(h) - w(0) = 0, \tag{2.31}$$

where $w(0) = 0$ because of the boundary condition (2.19) and $w(h)$ can be found by taking the material derivative of the function $f(x, y, z, t) = h(x, y, t) - z = 0$:

$$\frac{Df}{Dt} = \frac{\partial f}{\partial t} + u\frac{\partial f}{\partial x} + v\frac{\partial f}{\partial y} + w\frac{\partial f}{\partial z} = -\frac{\partial h}{\partial t} + u\frac{\partial h}{\partial x} + v\frac{\partial h}{\partial y} + w = 0. \tag{2.32}$$

Now combining equations (2.31) and (2.32) gives the lubrication equation in terms of volume fluxes:

$$\frac{\partial h}{\partial t} + \frac{\partial Q_x}{\partial x} + \frac{\partial Q_y}{\partial y} = 0, \tag{2.33}$$

or when the volume fluxes in equations (2.28) and (2.29) are filled in:

$$\frac{\partial h}{\partial t} + \frac{\partial}{\partial x}\left[\frac{h^2}{2\mu}\frac{\partial \gamma}{\partial x} - \frac{h^3}{3\mu}\frac{\partial P}{\partial x}\right] + \frac{\partial}{\partial y}\left[\frac{h^2}{2\mu}\frac{\partial \gamma}{\partial y} - \frac{h^3}{3\mu}\frac{\partial P}{\partial y} + Uh\right] = 0. \tag{2.34}$$

Where the pressure P is defined by:

$$P = \rho g y - \gamma\left(\frac{\partial^2 h}{\partial x^2} + \frac{\partial^2 h}{\partial y^2}\right) - \Pi, \tag{2.35}$$

which consists of the hydrostatic pressure, Laplace pressure and the disjoining pressure defined by equation (2.10). The latter also regulates the stress singularity associated with a moving contact line. Assuming no or negligible shear stress at the liquid-vapour interface, equation (2.34) reduces to:

$$\frac{\partial h}{\partial t} + \frac{\partial}{\partial x}\left[\frac{h^3}{3\mu}\frac{\partial P}{\partial x}\right] + \frac{\partial}{\partial y}\left[\frac{h^3}{3\mu}\frac{\partial P}{\partial y} + Uh\right] = 0. \tag{2.36}$$

This lubrication equation for the dip-coating system describes the withdrawal with constant velocity U of a solid plate immersed in a wetting liquid.

The steady state for low Reynolds numbers was first analysed by Landau, Levich and Derjaguin [40], [41]. For small Reynolds numbers the film thickness far away from the reservoir h_∞ depends on the balance between viscous and capillary forces, i.e. the capillary number $Ca = \mu U/\gamma$. The force balance then simplifies from equation (2.17) to:

$$\mu\frac{\partial^2 u}{\partial z^2} = -\gamma\frac{\partial \kappa}{\partial x}, \tag{2.37}$$

with κ the meniscus curvature. This scales as:

$$\frac{\mu U}{h_\infty^2} \sim \frac{\gamma\kappa}{l} \tag{2.38}$$

with l the length scale of the dynamic meniscus. In this scaling there are two unknowns, l and h_∞. Introducing the capillary length $l_c = \sqrt{\frac{\gamma}{\rho g}}$ as the radius of curvature of the static meniscus. The small slope approximation of the meniscus curvature then gives a relation between l and l_c:

$$\frac{1}{l_c} = \kappa \approx \frac{\partial^2 h}{\partial y^2} \sim \frac{h_\infty}{l^2}, \tag{2.39}$$

from which follows

$$l \sim \sqrt{h_\infty l_c}. \tag{2.40}$$

Now combining equations (2.38) and (2.40) gives the scaling relation also known as Landau-Levich-Derjaguin law [40], [41]:

$$h_\infty \sim l_c Ca^{2/3}, \tag{2.41}$$

which describes the film thickness h_∞ for the viscous-capillary regime. The law is valid for small capillary numbers $Ca \ll 1$ since for higher capillary numbers the static and dynamic menisci do not match.

A similar argument can also be used for the high-speed regime when capillary forces no longer play a role. The film regime is then characterized by the balance of viscous forces and gravity:

$$\mu \frac{\partial^2 u}{\partial z^2} = \rho g, \tag{2.42}$$

which leads to the scaling law:

$$h_\infty \sim l_c Ca^{1/2}, \tag{2.43}$$

which is known as Derjaguin's law [42], [43].

As discussed the lubrication equation and derived scaling laws are valid for small slopes $\left[\frac{\partial h}{\partial x}\right] = \left[\frac{\partial h}{\partial y}\right] \sim \frac{H}{L} = \epsilon \ll 1$ and small Reynolds numbers (inertial effects are neglected). For partially wetting liquids, i.e. increasing contact angles θ, the lubrication approximation is not valid.

2.7 Dip-coating of defects on flat surfaces

In the previous section the lubrication equation for dip-coating of a flat homogeneous substrate is derived. In this section the model is adjusted to model the dip-coating of a defect. A defect can have both a topographic and a chemical component.

To model the topographic component of the defect on the flat substrate the equation for the location of the liquid air interface $h'(x, y, t)$ is given by [44]:

$$h'(x, y, t) = h(x, y, t) + s(x, y, t), \tag{2.44}$$

with $h(x, y, t)$ the film thickness and $s(x, y, t)$ the substrate height. The lubrication equation is given by:

$$\frac{\partial h}{\partial t} + \frac{\partial}{\partial x}\left[\frac{-h^3}{3\mu}\left(\frac{\partial P}{\partial x}\right)\right] + \frac{\partial}{\partial y}\left[\frac{-h^3}{3\mu}\left(\frac{\partial P}{\partial y} + Uh\right)\right] = 0, \tag{2.45}$$

with P the pressure defined by:

$$P = \left(\frac{\partial^2}{\partial x^2} + \frac{\partial^2}{\partial y^2}\right)\left(-\gamma h'\right) + \rho g y - \Pi. \tag{2.46}$$

Where Π denotes the disjoining pressure (equation (2.10)), also discussed in section 2.4, which is implemented to model the moving contact line. The contact angle distribution $\theta(x, y, t)$ is used to model the chemical component of the defect.

The satellite droplets underneath the defects after dip-coating are a consequence of the break up of the liquid bridge between the pattern and retracting meniscus. This break up is governed by the Rayleigh-Plateau instability [43], [45]. The Rayleigh-Plateau instability of a cylindrical free surface, i.e. ligament, states that the surface tension has a destabilizing effect on the liquid-vapour interface. Due to the surface tension the liquid wants to minimize its surface energy which causes small perturbations in the liquid-vapour interface, i.e. capillary waves, to be amplified. These waves modulate the mean curvature of the liquid surface and generate gradients of Laplace pressure, which further amplify the perturbation till break up into droplets. The break up of liquid filaments (or rivulets) on a partially wetting solid substrate is studied

numerically by Ghigliotti et al. [46]. They showed that the hydrophobicity of the substrate promotes the break up of the rivulet and decreases the spacing of the formed droplets.

The influence of the geometrical parameters of a Gaussian surface defect on a droplet moving down an inclined surface is studied by Park and Kumar [47]. Using the lubrication framework and similar disjoining-pressure model as described in sections 2.5 and 2.4, respectively, they showed that the critical sliding angle strongly relates to the maximum slope (height divided by width s_0/a) of the defect rather than its height or width individually. Also comparing a dent (or groove, negative height) and bump (positive height) with similar slopes magnitude showed that the dent has a smaller critical sliding angle compared to the bump. For a dent with too small width, capillary action causes the dent to fill quickly at a small critical sliding angle.

Chapter 3

Dip-coating setup

The purpose of this chapter is to describe the liquid entrainment by a single heterogeneity on a partially wetted substrate dip-coated from a liquid reservoir. First in section 3.1 an overview of the dip-coating setup is given and the sample manufacturing procedure, which creates the well-defined heterogeneities on the substrate, is discussed. Second in section 3.2 the results are presented and discussed. Finally in section 3.3 conclusions are given regarding the results. The experimental results and conclusions will be complemented by numerical simulations in chapter 4.

3.1 Experimental setup

In this section the dip-coating setup is discussed. First an overview is of the setup is given. Next in paragraph 3.1.1 the sample manufacturing process is described. The measured parameters for the materials used, are discussed in paragraph 3.1.2. Finally in paragraph 3.1.3 the experimental procedure is given.

Figure 3.1(a) illustrates the dip-coating setup where a sample is pulled out of a liquid reservoir with a constant velocity U. The sample surface is always oriented parallel to the direction of withdrawal. The sample is attached into the sample holder which is mounted onto a Newport XMS160 computer-controlled translation stage. The translation stage can operate velocities within a range $U = [0 - 20]$ mm/s. The samples are manufactured from silicon-oxide wafers (Si-Mat Prime, $\langle 1\,0\,0 \rangle$) using photo-lithography to define heterogeneities (patterns). In paragraph 3.1.1 the manufacturing procedure is fully described. An illustration of a manufactured sample, including the pattern, is given in figure 3.1(b-c). The pattern is both a topographic and chemical heterogeneity with a certain shape, pattern dimension a, contact angle θ_{pr} and thickness h_{pr}. Figure 3.1(d) shows a photograph of the setup with the different components. The camera (Basler acA1280-60gm, Mitutoyo M Plan APO 2x/0.055) is used to capture the dynamics of the liquid entrainment. In all the experiments the reservoir liquid is a glycerol-water solution, of which the relevant properties are the viscosity $\mu = 220 \pm 20\,\mathrm{mPa \cdot s}$, the surface tension $\gamma = 60.9 \pm 0.5\,\mathrm{mN/m}$ and the density $\rho = 1.26\,\mathrm{g/cm^3}$ [48]. The main benefits of using glycerol, are its non-volatility and and its relatively high viscosity, which enables experiments corresponding to relatively high values of Ca at moderate speeds. Glycerol is a hygroscopic liquid, which means it absorbs moist in the air. During the experiments the reservoir liquid, i.e. glycerol is exposed to the air. To make sure the relevant properties do not change over time during the experiments the supplied anhydrous glycerol (Fluka 49770) is let to equilibrate with the air humidity before the glycerol is used in the experiments. The relevant liquid properties of the equilibrated glycerol are measured in paragraph 3.1.2. In order to minimize the influence of airborne particle contamination the setup is placed in a closed

environment that is continuously provided with filtered air and the samples are always stored in clean and closed sample-boxes.

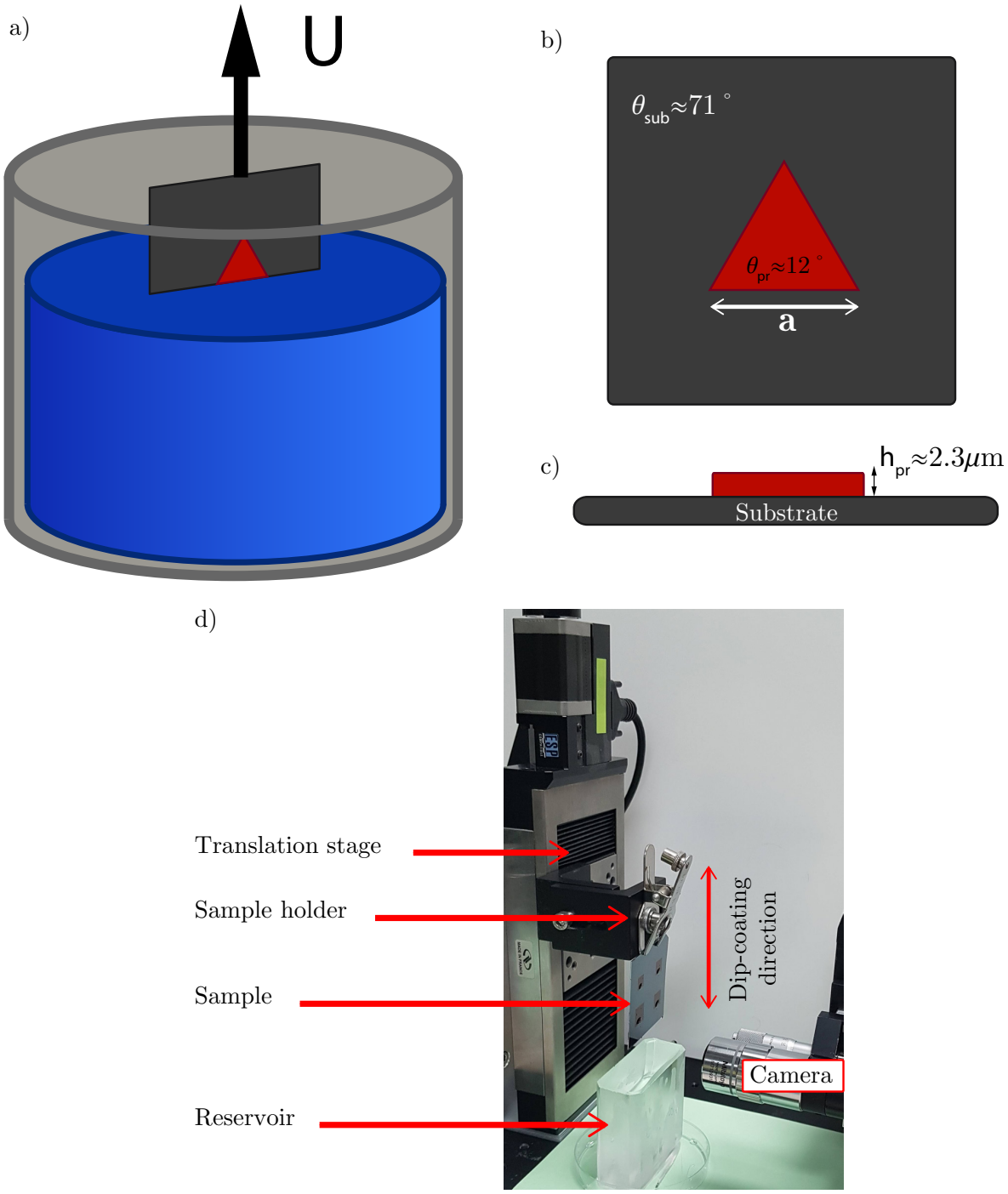

Figure 3.1: (a) Sketch of dip-coating process where a sample is pulled out of the liquid reservoir with a velocity U. (b) Top-view of the sample, where the grey represents the wafer with a receding contact angle $\theta_{sub} \approx 71°$ and the red the pattern with a receding contact angle $\theta_{pr} \approx 12°$, and pattern dimension a. (c) Side-view of the sample to illustrate the height difference $h_{pr} \approx 2.3 \pm 0.1\,\mu$m. (d) Photograph of the dip-coating setup with an overview of the different components.

3.1.1 Sample procedure

Samples were manufactured from 5x5 cm silicon-oxide wafers using photo-lithography. The sample fabrication procedure, involving four consecutive steps, is discussed below and depicted

schematically in figure 3.2. A more detailed step-by-step recipe is added in the Appendix.

(a) The substrate is thoroughly cleaned with ultrapure water (Millipore Direct-Q3, 18.2 $M\Omega cm$). After the substrate is completely dry, positive photoresist (Allresist, AR-P 3510T) is spin-coated onto the substrate using a Brewer Science 200X spin-coating machine [3.2(a)]. For a smooth and homogeneous layer the spin coating process is divided in two steps. First the substrate is rotated at 200 RPM for 10 s with a maximum acceleration of 100 RPM/s to gradually thin the manually applied thick layer of photoresist. Second the substrate is rotated at 4000 RPM for 60 s with a maximum acceleration of 200 RPM/s to thin the layer to a thickness of $h_{pr} \approx 2.3 \pm 0.1\,\mu$m. After the spin-coating process the substrate is baked at a temperature of 110 °C for approximately 90 s to promote the adhesion.

(b) Next the photoresist layer is exposed by an UV lamp (Karl Suss MJB3UV 300-400) using a custom printed plastic mask to define the pattern. As shown in figure 3.2(b) all photoresist except the pattern itself is exposed by the UV light.

(c) After exposure the sample is developed using a 1:10 diluted with distilled water developer solution (Allresist, AR300-26). As shown in figure 3.2(c) the exposed areas of the sample are rinsed by the developer and only the pattern remains. To promote the adhesion of the remaining photoresist (pattern) the sample is baked at a temperature of 115 °C for 90 s.

(d) In the last step of the sample preparation the sample is first put in a UV Ozone cleaner (Jelight 42-220) for 15 minutes, where a photo-sensitized oxidation process removes contaminant molecules. Second the sample is put in a Tricholoro(1H,1H,2H,2H-perflorooctyl)silane (PFOTS, Sigma Aldrich, 448931) diluted by anhydrous heptane (Sigma Aldrich, 226654) bath for 2 hours, where a PFOTS monolayer is formed on the sample that renders the silicon oxide surface regions (i.e. those not covered by photoresist) hydrophobic. After 2 hours the sample is put in an anhydrous hexan (Sigma Aldrich, 227064) bath for 20 seconds to remove the residual PFOTS solution. Finally the sample is baked at a temperature of 115°C for 30s to promote the formation of the monolayer and evaporate the remaining solution.

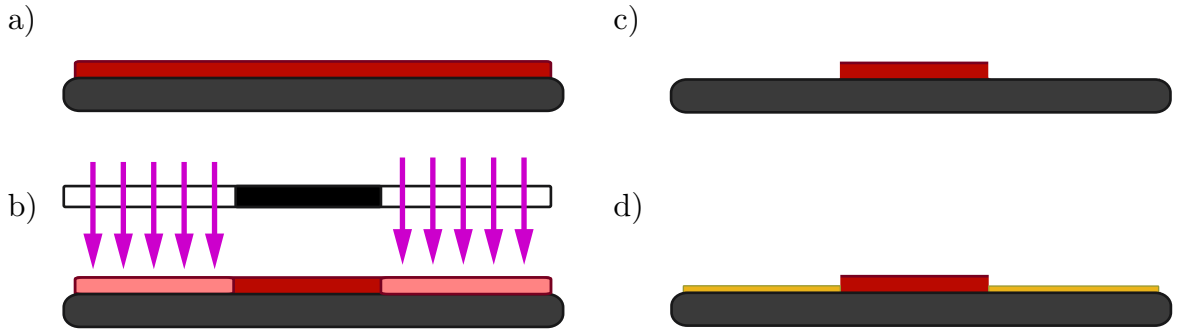

Figure 3.2: (a-d) Main steps of photo-lithography process (see text) to make samples with a well-defined heterogeneity (pattern) on its surface.

The samples comprise thus both a topographic and chemical heterogeneity with a certain shape (circle, square or equilateral triangle), pattern dimension a, and thickness h_{pr} as illustrated in figure 3.1(b,c).

3.1.2 Material parameters

In this paragraph the measurements of the relevant liquid properties of glycerol, contact angles of the liquid-PFOTS and liquid-photoresist and the thickness of the spin-coated photoresist are discussed.

Contact angle

The contact angles are measured of the liquid-PFOTS and liquid-photoresist interfaces. Both the static advancing and receding contact angle are measured by the dynamic sessile droplet method, which is discussed in section 2.3. In this method a droplet is put between the substrate and a needle which controls the in- and outflow of the liquid. The needle is connected to a syringe (BD Plastipak 3ml) via a tube. The in- and outflow are controlled by the syringe pump (Kd Scientific Legato 180). For both the static advancing and receding contact angle measurements the in- and outflow is set to $2\,\mu$l/min. The droplet expands or contracts and the dynamics are captured with the camera (Basler acA1280-60gm, Mitutoya M Plan APO 2x/0.055). A snapshot is taken just before contact line moves due to the expanding or contracting droplet. The contact angle is determined manually by placing two lines: one on the liquid-PFOTS interface and one parallel to the liquid-air interface close to the contact line as depicted in figure 3.3. The results are summarized in table 3.1.

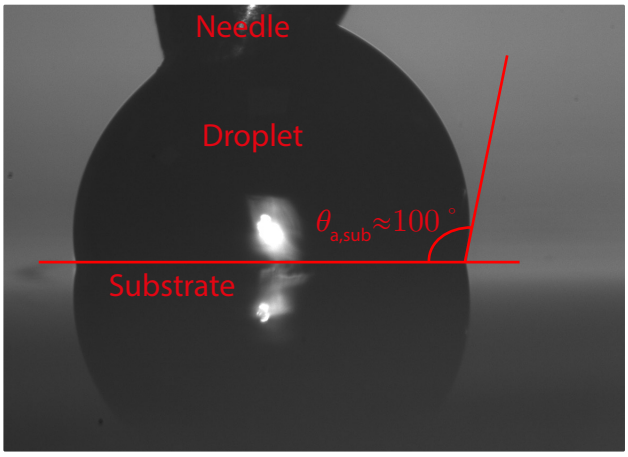

Figure 3.3: Snapshot of static advancing contact angle measurement of the substrate (PFOTS) and glycerol. The static advancing contact angle is given by $\theta_{sa,sub} = 100 \pm 2\,^o$

Table 3.1: Results of static advancing and receding contact angle measurements with glycerol on the PFOTS and photoresist.

symbol	description	liquid-PFOTS	liquid-photoresist
θ_{sa}	Static advancing contact angle [^{o}]	100 ± 2	88 ± 2
θ_{sr}	Static receding contact angle [^{o}]	71 ± 2	12 ± 2

Surface Tension

The surface tension of glycerol is measured via the Wilhelmy Plate method which requires a wetting platinum plate to make contact with the liquid surface [49]. The surface tension γ is given by:

$$\gamma = \frac{m'g}{2L'}, \tag{3.1}$$

with m' the mass pulled by the plate in contact with the liquid, $g = 9.81\,\mathrm{m/s^2}$ gravity constant and $L' = 1.047\,\mathrm{cm}$ the length of plate which comes in contact with the liquid. Before a measurement the plate is cleaned with distilled water and held in a natural gas flame to clean it from all possible contamination which could influence the wettability of the surface. The results of three different liquids are given in table 3.2. The lower than expected value for the

glycerol-water solution could be caused by surfactant contaminant due to the ozone-cleaning of the photoresist.

Table 3.2: Results of Wilhelmy Plate surface tension measurements of ultra-pure water, anhydrous glycerol and glycerol. The surface tension is calculated with equation (3.1) and the errorbars via error propagation (Appendix A.1).

liquid	mass m' $[g]$	surface tension [mN/m]	surface tension literature [mN/m]
Ultrapure Water	0.155 ± 0.001	72.6 ± 0.5	72.75 [50]
Glycerol-water	0.130 ± 0.001	60.9 ± 0.5	-
Anhydrous glycerol	0.126 ± 0.001	59.0 ± 0.5	62.5 [50]

Viscosity

The viscosity μ is measured with a viscometer (BrookField DV-II+ Pro) which measures the viscosity via a rotating sensing element in the fluid. The torque necessary to maintain a certain angular velocity determines the viscosity. In table 3.3 the results are presented.

Table 3.3: Results of viscosity measurements of anhydrous glycerol and glycerol. In the last column the literature value is given for the anhydrous glycerol at a temperature of $T = 25^o$.

liquid	temperature T $[^oC]$	viscosity measured [mPa $\cdot$ s]	viscosity literature [mPa $\cdot$ s]
Anhydrous glycerol	27 ± 1	710 ± 10	934 [50]
Glycerol-water	28 ± 1	220 ± 20	-

Thickness photoresist

The thickness of the spin coated layer photoresist and thus the height of the printed patterns h_{pr}, as illustrated in 3.1(c) is determined by the material properties of the photoresist and the spin-coating settings. The layer thickness is measured using Atomic Force Microscopy (AFM) where for two different sample patterns edges the height $h(x)$ was measured as a function of the spatial coordinate x. The results of this measurements are depicted in figure 3.4, with a resulting layer thickness of $h_{pr} \approx 2.3 \pm 0.1\,\mu$m. Due to the limitations of the AFM the relatively steep slope of the pattern edge might not be measured accurately. The slope is roughly estimated by $h_{pr}/c \approx 0.2 \pm 0.1$, with c the transition length. The resulting layer thickness h_{pr} and transition length c are the mean and standard deviation of the two measured sample patterns.

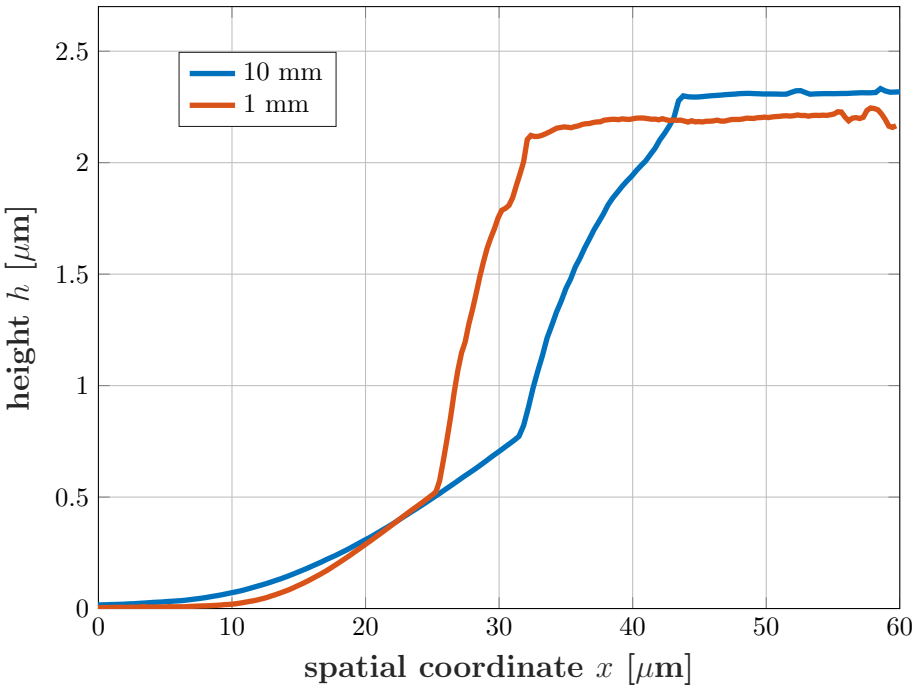

Figure 3.4: Image of the height profile taken with an AFM at the edge of the pattern with pattern dimensions $a = 1\,\text{mm}$ and $a = 10\,\text{mm}$. The thickness of the photoresist after spin-coating is given by $h_{pr} \approx 2.3 \pm 0.1\,\mu\text{m}$. The slope is roughly estimated by $h_{pr}/c \approx 0.2 \pm 0.1$, with c the transition length.

3.1.3 Experimental procedure

The dip-coating speed U, the pattern dimension a and pattern shape are systematically varied to elucidate the liquid entrainment due to a single surface 'defect' or heterogeneity. Figure 3.5 shows a typical image of a series of 'satellite droplets' formed underneath a rectangle of width $a = 4\,\text{mm}$ dip-coated at a speed of $U = 6\,\text{mm/s}$ as a result of the liquid entrainment process taken by an upright optical microscope. The liquid entrainment is quantified by extracting both the radius and the distance of the biggest satellite droplet under the defect using the images from an upright microscope (Olympus BX51). The distance of the biggest satellite droplet is defined as the distance from the pattern edge to the center of the droplet. The objectives used of the microscope and corresponding calibration values are summarized in table 3.4. The calibration values are determined by taking an image of a calibration target with known dimensions. The error made during conversion from pixels to meters is less than 0.5% and therefore neglected in the rest of this thesis.

Table 3.4: Objectives used in the upright optical microscope with corresponding calibration values. The calibration values are determined by dividing a known calibration target by the manually determined length in pixels. The error in the calibration values are determined from reproducibility to be less than 0.5% and therefore neglected in the rest of this thesis.

name	magnification	Numerical Aperature (NA)	calibration [nm/pixel]
Mplan Apo	1.25x	0.04	3733
Mplan Apo	2.5x	0.08	1859
LMplan FL N	5x	0.13	927.9
Uplan FL	10x	0.3	465.2
Mpan FL	50x	0.8	93.0

The droplets in figure 3.5 are not perfectly circular but slightly elongated in the vertical

(dip-coating) direction. This is due to contact angle hysteresis of the substrate. The Rayleigh-Plateau instability breaks up the vertical orientated rivulet into a trail of droplets. The droplets want to minimize its surface energy so in a perfectly flat homogeneous substrate this would lead to a spherical (topview) droplet. Due to small heterogeneities (insignificant compared to the well-defined patterns studied) the moving contact line can pin locally to the substrate resulting in contact angle hysteresis. During the break up of the vertical orientated rivulet the bottom and top contact lines of the droplets tends to move the most to minimize its surface energy resulting in the observed elongated droplets. The dynamic break up process is captured with the camera (Basler acA1280-60gm, Mitutoyo M Plan APO 2x/0.055) depicted in 3.1(d).

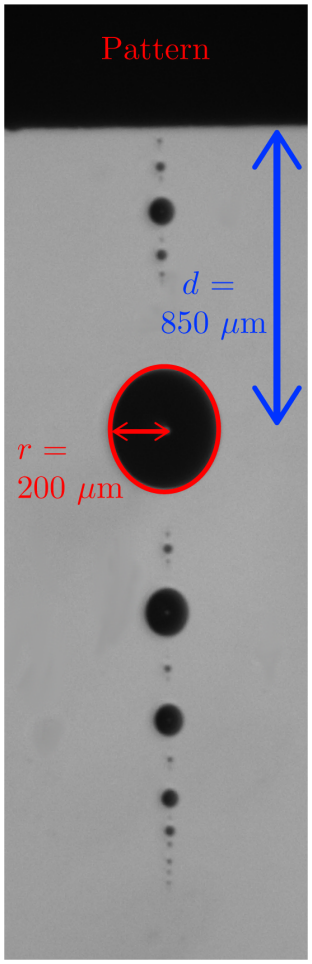

Figure 3.5: Typical image of a dip-coating experiment with residual droplets underneath the pattern taken by the upright optical microscope. In this case the pattern was a square with pattern dimension $a = 4\,\text{mm}$ and dip-coating velocity of $U = 6\,\text{mm/s}$. The droplets are not perfectly spherical but at bit elongated in the vertical (dip-coating) direction.

The images are analysed via a semi-automatic script (added in Appendix) where manually an ellipse is placed over the boundary of the droplet and a line is drawn between the pattern edge and the droplet boundary. Due to the slightly elongated droplets the radius is actually the equivalent radius defined by:

$$r = \sqrt{a'b'}, \tag{3.2}$$

with a' and b' the semi-major and semi-minor axis of the ellipse. Throughout the thesis the equivalent radius will be denoted by the radius r. The script first expresses the radius and distance of the biggest satellite droplet in pixels. With the calibration values depicted in table 3.4 these are converted to meters.

The dip-coating setup has been described, and now a set of systematic experiments is done where the pattern shape, pattern dimension a and dip-coating velocity U are varied and both the break up and residual droplets are captured and analysed.

3.2 Results and discussion

In this section the dip-coating results are presented and discussed. First the quantitative results of the analysed images for the dip-coating experiments are presented and discussed for each shape in sections 3.2.1-3.2.3. Second the effect of the varied parameters; dip-coating velocity, pattern dimension and pattern shape are discussed in sections 3.2.4, 3.2.5 and 3.2.6, respectively. Finally in section 3.2.7 the satellite droplet decay in size is discussed.

The critical dip-coating velocity, which solely depends on the contact angle, is given by $U_c = 6.5 \pm 0.5\,\mathrm{mm/s}$. For the dip-coating velocities $U > U_c$ a film will be pulled independent of any heterogeneities on the sample. All experiments are repeated, with the same input parameters, for at least four times. Since experiments with lower dip-coating velocities $U < 4\,\mathrm{mm/s}$ showed higher reproducibility, these were repeated only three times. The errorbars in all the experimental graphs are given by the standard deviation of these repeated experiments.

3.2.1 Squares

In figure 3.6 the radius of the biggest satellite droplet is given as a function of a square pattern with pattern dimension a for different dip-coating velocities U. Both an increase in pattern dimension a and dip-coating velocity U result in a bigger satellite droplet. For dip-coating velocities $U < \frac{U_c}{6}$ a transition is observed for the pattern dimension approaching the capillary length $a = l_c \approx 2\,\mathrm{mm}$. Both regimes ($a < l_c$ and $a > l_c$) are fitted with a power law fit given by:

$$r \sim a^{p_r}, \tag{3.3}$$

with p_r the exponent of the power law. Below the capillary length ($a < l_c$) the radius of the biggest satellite droplet scales linear with the pattern dimension a. Above the capillary length $a > l_c$ for the largest dip-coating velocities the radius of the biggest satellite droplet still scales linear with the pattern dimension a, while the lower velocities show significant decrease in scaling from linear ($p_r = 1$) to $p_r = 0.23$ and 0.26 for $U = 0.25$ and $1\,\mathrm{mm/s}$, respectively. The transition, which occurs around the capillary length l_c for lower dip-coating velocities ($U < 1\,\mathrm{mm/s}$) shifts to larger pattern dimensions for larger dip-coating velocities ($U > 3\,\mathrm{mm/s}$).

In Figure 3.7 the distance of the biggest satellite droplet is given as a function of a square pattern with pattern dimension a for different dip-coating velocities U. This distance is defined by the pattern edge and center of the satellite droplet. An increase in pattern dimension a and dip-coating velocity U result in a larger distance of the biggest satellite droplet. Again a transition is observed for the pattern dimension approaching the capillary length $a = l_c \approx 2\,\mathrm{mm}$. Both regimes ($a < l_c$ and $a > l_c$) are fitted with a power law fit given by:

$$d \sim a^{p_d}, \tag{3.4}$$

with p_d the exponent of the power law. Below the capillary length ($a < l_c$) the distance of the biggest satellite droplet scales approximately linear $p_d = 0.98$ with the pattern dimension a. For pattern dimensions larger than the capillary length $a > l_c$ and for large DC velocities, the distance of the biggest satellite droplet still scales approximately linear with the pattern dimension a, while the lower velocities show significant decrease in scaling from approximately linear ($p_d = 0.98$) to $p_d = 0.32$, 0.67 and 0.54 for $U = 0.25$, 1 and $3\,\mathrm{mm/s}$, respectively. The highest dip-coating velocities show relatively large standard deviations. Due to the high dip-coating velocity the rivulet increases in length and the break-up is less reproducible compared

to lower velocities. This has a larger effect on the distance compared to the radius of the biggest satellite droplet. Although the fit exponent $p_d = 0.67$ for $U = 1\,\mathrm{mm/s}$ is larger than $p_d = 0.54$ for $U = 3\,\mathrm{mm/s}$, this is not as expected. One explanation could be the few outliers causing a less accurate fit.

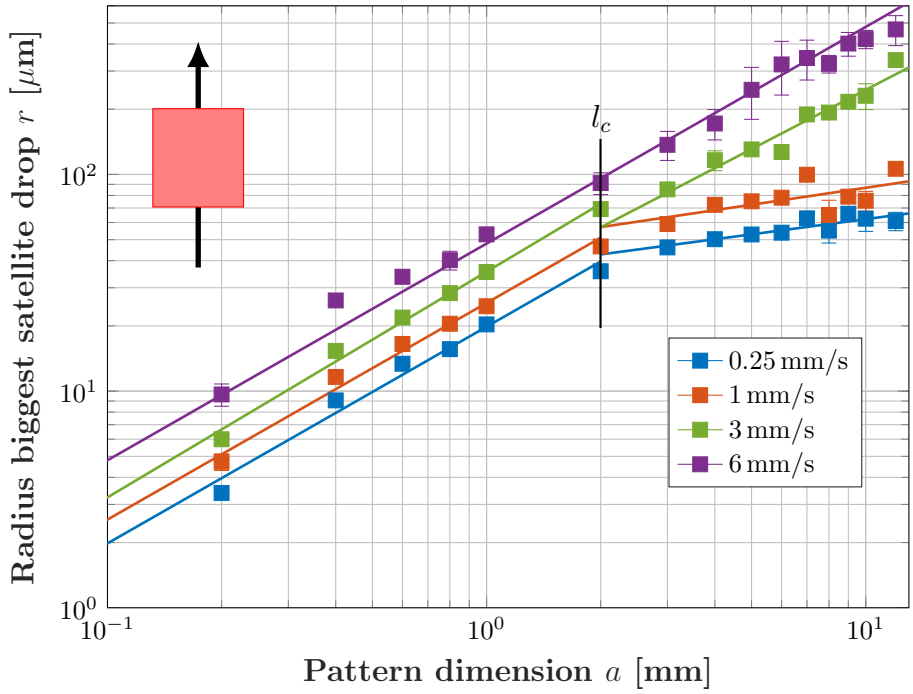

Figure 3.6: Radius of biggest satellite droplet versus the pattern dimension a for a square pattern shape at different dip-coating velocities. The critical dip-coating velocity is given by $U_c = 6.5 \pm 0.5\,\mathrm{mm/s}$. The data is fitted with power laws above and below the capillary length l_c. The exponent of the fit p_r below the capillary length ($a < l_c$) is given by $p_r = 1$. The exponents of the fits above capillary length ($a > l_c$) are given by $p_r = 0.23, 0.26, 0.9$ and 1. The errorbars correspond to the standard deviation.

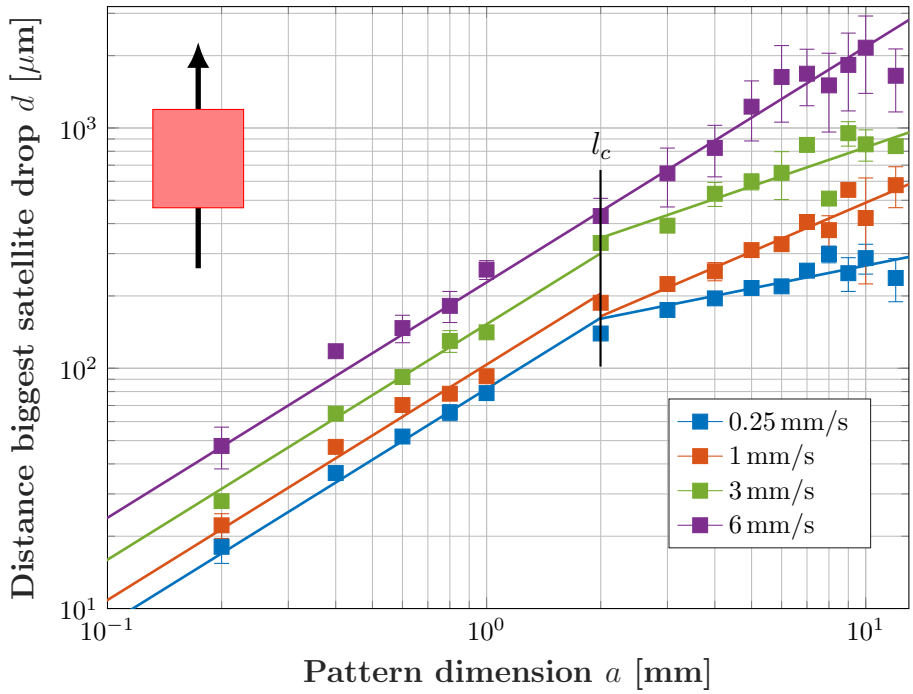

Figure 3.7: Distance of biggest satellite droplet versus the pattern dimension a for a square pattern shape at different dip-coating velocities. The critical dip-coating velocity is given by $U_c = 6.5 \pm 0.5\,\mathrm{mm/s}$. The data is fitted with power laws above and below the capillary length. The exponent of the fit below the capillary length ($a < l_c$) is given by $p_d = 0.98$. The exponents of the fits above capillary length ($a > l_c$) are given by $p_d = 0.32, 0.67, 0.54$, and 0.98. The errorbars correspond to the standard deviation.

Figures 3.8 and 3.9 show the radius and distance of the biggest satellite droplet as a function of the dip-coating velocity U for different pattern dimensions a. This is the same data as depicted in figures 3.6 and 3.7, but with the dip-coating velocity U and pattern dimension a switching places between legend and x-axis. Both figures still show an increase in dip-coating velocity U or pattern dimension a results in a larger and further displaced satellite droplet, however gives more detail in the influence of the dip-coating velocity U. Dip-coating velocities $U < 2\,\mathrm{mm/s}$ are fitted with power laws given by:

$$r \sim U^{q_r} \tag{3.5}$$

$$d \sim U^{q_d} \tag{3.6}$$

with q_r and q_d the exponents of the power law fits. For small pattern dimensions ($a < l_c$) the radius and distance of the biggest satellite droplet scales with $q_r = 0.21$ and $q_d = 0.20$, respectively, with small dip-coating velocities ($U < 2\,\mathrm{mm/s}$). For dip-coating velocities approaching the critical dip-coating velocity $U \to U_c = 6.5 \pm 0.5\,\mathrm{mm/s}$ however, exponential behaviour is observed. This exponential behaviour is characterized by an exponential fit given by:

$$r \sim e^{k_r U} \tag{3.7}$$

$$d \sim e^{k_d U} \tag{3.8}$$

with k_r and k_d the exponential fit parameters. For square patterns with pattern dimensions $a < 6\,\mathrm{mm}$ and DC velocities close to the critical value $2 < U < U_c\,\mathrm{mm/s}$ the exponential fit parameters are given by $k_r \approx 0.15 \pm 0.01$ and $k_d \approx 0.17 \pm 0.02$. Both k_r and k_d are the mean of the individual parameters which are given in the caption. The error corresponds to the standard deviation of this mean. Figures 3.8 and 3.9 show the observed scaling transition (power to exponential law) moves to lower DC velocities U for higher pattern dimensions $a > l_c$.

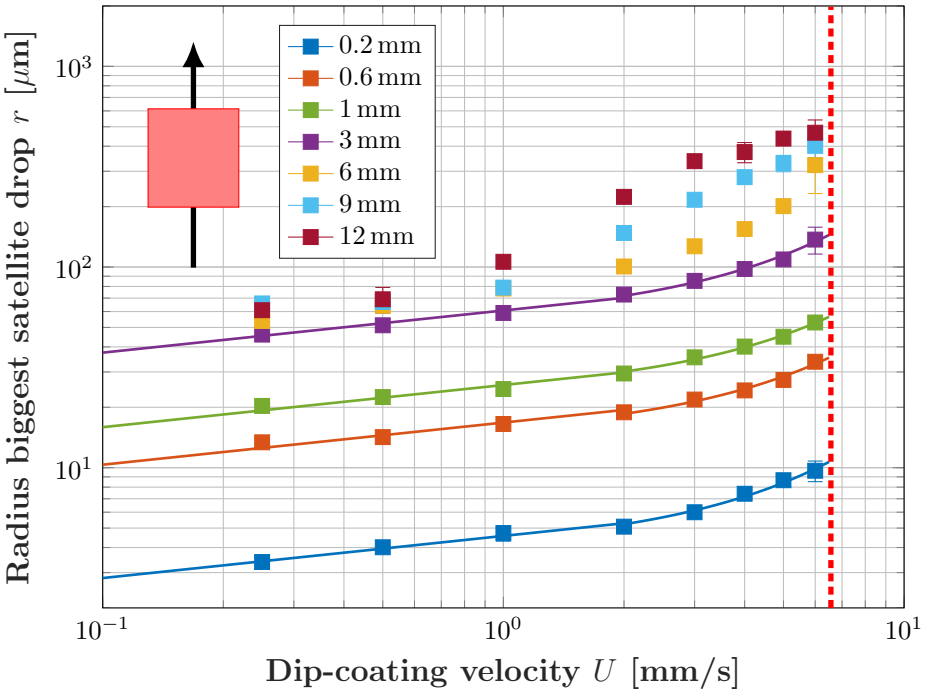

Figure 3.8: Radius of biggest satellite droplet versus the dip-coating velocity U for a square pattern shape at different pattern dimensions a. The critical dip-coating velocity is given by $U_c = 6.5 \pm 0.5\,\mathrm{mm/s}$ illustrated by the dashed red line. The data is fitted with power laws for small DC velocities $U < 2\,\mathrm{mm/s}$ and small pattern dimensions $a < 6\,\mathrm{mm}$. The exponent of this fit is given by $q_r = 0.21$. The data for big DC velocities $2 < U < U_c\,\mathrm{mm/s}$ and small pattern dimensions $a < 6\,\mathrm{mm}$ is fitted with an exponential fit which yields $k_r = 0.16, 0.14, 0.14, 0.16$ from $a = 0.2\,\mathrm{mm}$ to $a = 3\,\mathrm{mm}$. The errorbars correspond to the standard deviation.

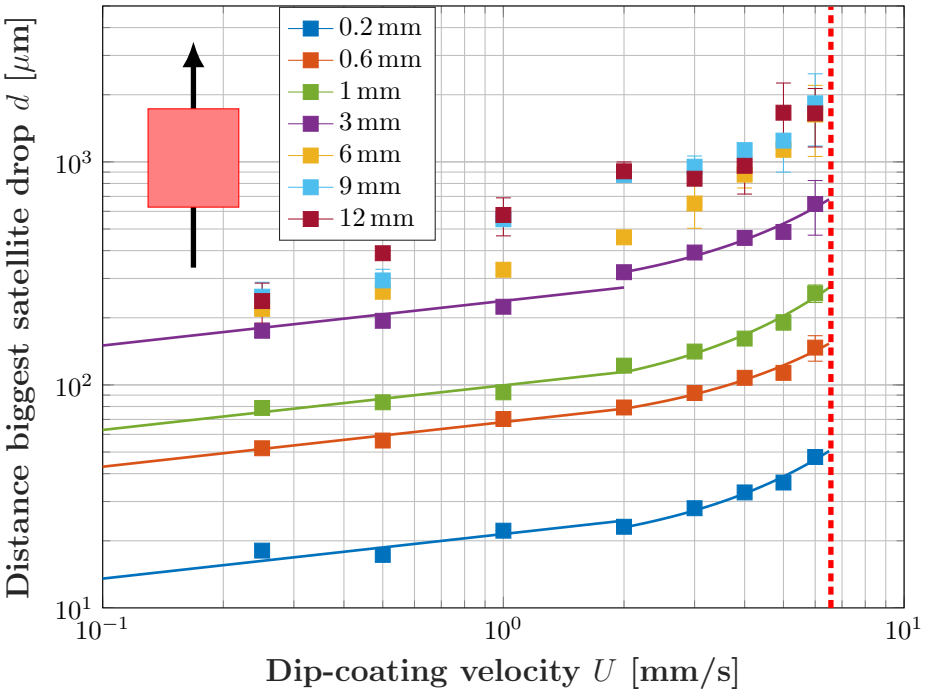

Figure 3.9: Distance of biggest satellite droplet versus the dip-coating velocities U for a square pattern shape at different pattern dimensions a. The critical dip-coating velocity is given by $U_c = 6.5 \pm 0.5\,\mathrm{mm/s}$ illustrated by the dashed red line. The data is fitted with power laws for small dip-coating velocities $U < 2\,\mathrm{mm/s}$ and small pattern dimensions $a < 6\,\mathrm{mm}$. The exponent of this fit is given by $q_d = 0.20$. The data for big DC velocities $2 < U < U_c\,\mathrm{mm/s}$ and small pattern dimensions $a < 6\,\mathrm{mm}$ is fitted with an exponential fit which yields $k_d = 0.18, 0.15, 0.19, 0.17$ from $a = 0.2\,\mathrm{mm}$ to $a = 3\,\mathrm{mm}$. The errorbars correspond to the standard deviation.

3.2.2 Triangles

In figures 3.10 and 3.11 the radius and distance of the biggest satellite droplet is given as a function of a triangle pattern with pattern dimension a for different dip-coating velocities U. Both an increase in pattern dimension a and dip-coating velocity U result in a bigger and further displaced satellite droplet. For dip-coating velocities $U < \frac{U_c}{6}$ a transition is observed for the pattern dimension approaching the capillary length $a = l_c \approx 2\,\mathrm{mm}$. Below the capillary length ($a < l_c$) the radius and distance of the biggest satellite droplet scales approximately linear $p_r = 0.89$ and $p_d = 0.90$, respectively, with the pattern dimension a. For pattern dimensions larger than the capillary length ($a > l_c$) the pattern dimension scales with $p_r = 0.33, 0.56, 0.94$ and 1.16 corresponding to the dip-coating velocities $U = 0.25, 1, 3$ and $6\,\mathrm{mm/s}$ to the radius of the biggest satellite droplet, respectively.

For pattern dimensions larger than the capillary length ($a > l_c$) again the smallest dip-coating velocities show a significant decrease in scaling from approximately linear ($p_r = 0.89$) to $p_r = 0.33$ and $p_r = 0.56$ for $U = 0.25$ and $U = 1\,\mathrm{mm/s}$ for the radius of the biggest satellite droplet. Also the distance of the biggest satellite droplet shows a similar decrease in scaling from approximately linear ($p_d = 0.90$) to $p_d = 0.24$ and $p_d = 0.55$ for dip-coating velocities $U = 0.25$ and $U = 1\,\mathrm{mm/s}$ for pattern dimensions larger than the capillary length $a > l_c$. The larger velocities $U = 3$ and $U = 6\,\mathrm{mm/s}$ show a slight increase in scaling with $p_r = 0.94$ and $p_r = 1.16$ for the radius of the biggest satellite droplet as a function of larger pattern dimensions $a > l_c$. However the relatively large offset of both fits for $a < l_c$ with $a > l_c$ is not physical. The transition will occur smoothly and not abruptly as suggested by this offset. It appears the transition, which occurs around the capillary length l_c for lower ($U < 1\,\mathrm{mm/s}$) dip-coating velocities shifts to larger pattern dimensions for larger ($U > 3\,\mathrm{mm/s}$) dip-coating velocities.

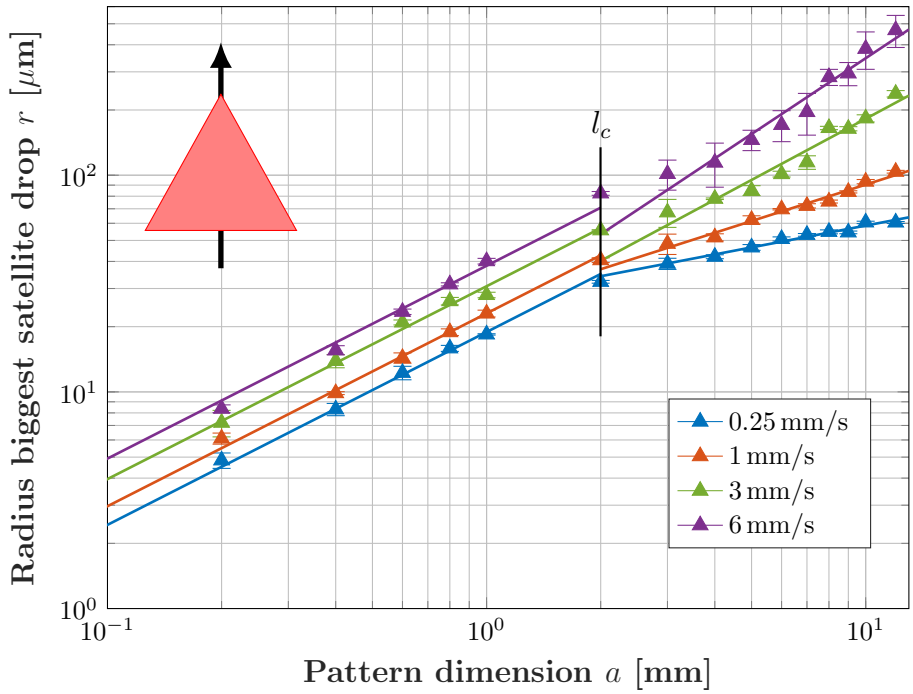

Figure 3.10: Radius of biggest satellite droplet versus the pattern dimension a for a triangle pattern shape at different dip-coating velocities U. The critical dip-coating velocity is given by $U_c = 6.5 \pm 0.5\,\mathrm{mm/s}$. The data is fitted with power laws for the pattern dimension above and below the capillary length. The exponent of the fit below the capillary length ($a < l_c$) is given by $p_r = 0.89$. The exponents of the fits above capillary length ($a > l_c$) are given by $p = 0.33, 0.56, 0.94$ and 1.16. The errorbars correspond to the standard deviation.

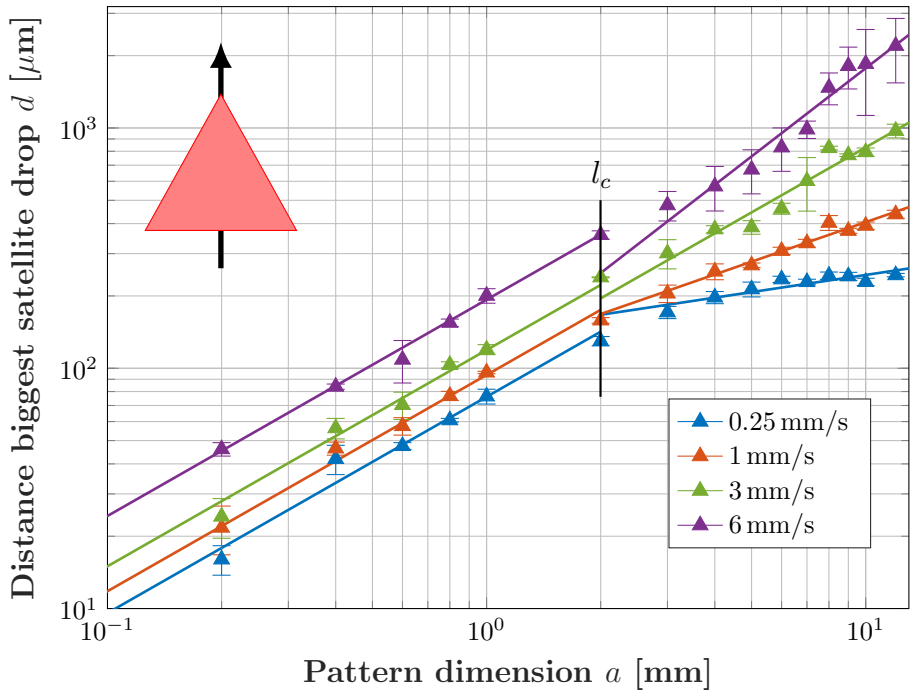

Figure 3.11: Distance of biggest satellite droplet versus the pattern dimension a for a triangle pattern shape at different dip-coating velocities U. The critical dip-coating velocity is given by $U_c = 6.5 \pm 0.5\,\mathrm{mm/s}$. The data is fitted with power laws for the pattern dimension above and below the capillary length. The exponent of the fit below the capillary length ($a < l_c$) is given by $p_d = 0.9$. The exponents of the fits above capillary length ($a > l_c$) are given by $q = 0.24, 0.55, 0.90$ and 1.22. The errorbars correspond to the standard deviation.

Figures 3.12 and 3.13 show the radius and distance of the biggest satellite droplet as a function of the dip-coating velocity U for different pattern dimensions a. This is the same data as depicted in figures 3.10 and 3.11, but with the dip-coating velocity U and pattern dimension a switching places between legend and x-axis. Both figures still show an increase in dip-coating velocity U or pattern dimension a results in a larger and further displaced satellite droplet, however gives more detail in the influence of the dip-coating velocity U. For small pattern dimensions ($a < 6\,\mathrm{mm}$) the radius and distance of the biggest satellite droplet scale both with $q_r = q_d = 0.18$, with small dip-coating velocities ($U < 2\,\mathrm{mm/s}$). For dip-coating velocities approaching the critical dip-coating velocity $U \to U_c = 6.5 \pm 0.5\,\mathrm{mm/s}$ exponential behaviour is observed. The exponential behaviour is quantified by fitting with equation (3.8) which yields $k_r \approx 0.09 \pm 0.04$ and $k_d \approx 0.16 \pm 0.02$. Both k_r and k_d are the mean of the individual fit parameters which are given in the caption. The error corresponds to the standard deviation of this mean. As also observed in figures 3.10 and 3.11 for higher pattern dimensions $a > l_c$ the observed scaling transition moves to lower dip-coating velocities U.

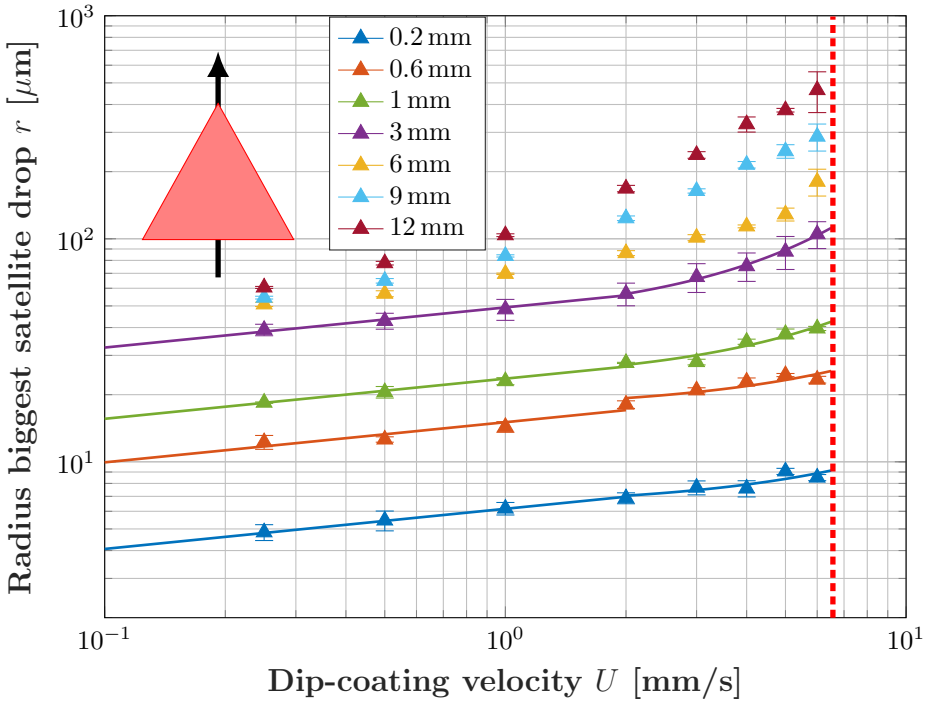

Figure 3.12: Radius of biggest satellite droplet versus the dip-coating velocity U for a triangle pattern shape at different pattern dimensions a. The critical dip-coating velocity is given by $U_c = 6.5 \pm 0.5\,\mathrm{mm/s}$ illustrated by the dashed red line. The data is fitted with power laws for small dip-coating velocities $U < 2\,\mathrm{mm/s}$ and small pattern dimensions $a < 6\,\mathrm{mm}$. The exponent of these fits is given by $q_r = 0.18$. The data for big DC velocities $2 < U < U_c\,\mathrm{mm/s}$ and small pattern dimensions $a < 6\,\mathrm{mm}$ is fitted with an exponential fit which yields $k_r = 0.06,\ 0.06,\ 0.1,\ 0.15$ from $a = 0.2\,\mathrm{mm}$ to $a = 3\,\mathrm{mm}$. The errorbars correspond to the standard deviation.

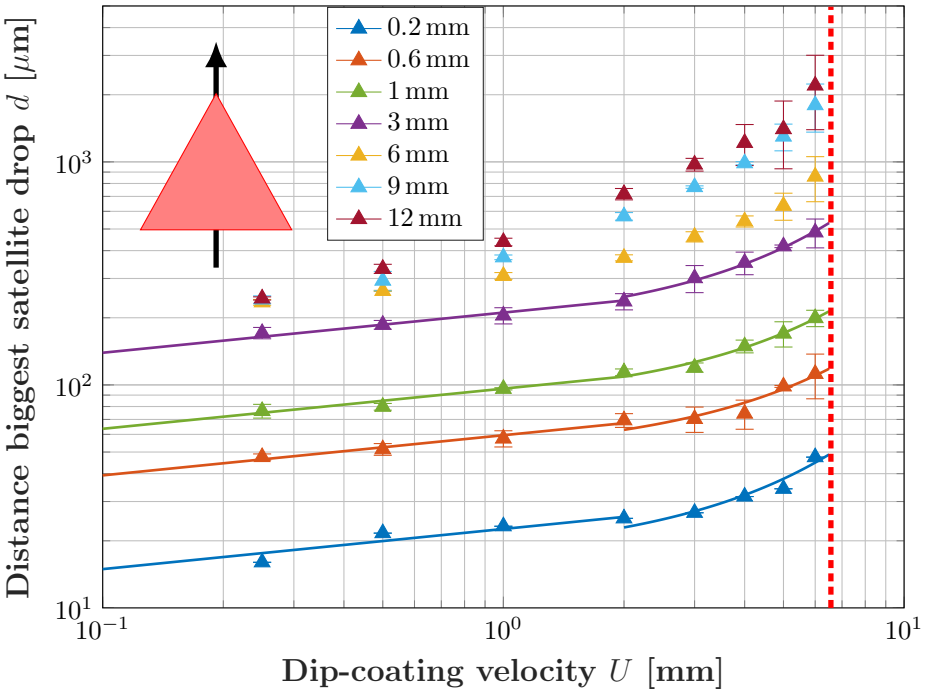

Figure 3.13: Distance of biggest satellite droplet versus the dip-coating velocities U for a triangle pattern shape at different pattern dimensions a. The critical dip-coating velocity is given by $U_c = 6.5 \pm 0.5\,\mathrm{mm/s}$ illustrated by the dashed red line. The data is fitted with power laws for small dip-coating velocities $U < 2\,\mathrm{mm/s}$ and small pattern dimensions $a < 6\,\mathrm{mm}$. The exponent of these fits is given by $q_d = 0.18$. The data for big DC velocities $2 < U < U_c\,\mathrm{mm/s}$ and small pattern dimensions $a < 6\,\mathrm{mm}$ is fitted with an exponential fit which yields $k_d = 0.17, 0.14, 0.15, 0.17$ from $a = 0.2\,\mathrm{mm}$ to $a = 3\,\mathrm{mm}$. The errorbars correspond to the standard deviation.

3.2.3 Circles

In figures 3.14 and 3.15 the radius and distance of the biggest satellite droplet is given as a function of the pattern dimension (or diameter) a for circular patterns for different dip-coating velocities U. Both an increase in pattern dimension a and dip-coating velocity U result in a bigger and further displaced satellite droplet. For dip-coating velocities $U < \frac{U_c}{6}$ a transition is observed for the pattern dimension approaching the capillary length $a = l_c \approx 2\,\mathrm{mm}$. Below the capillary length ($a < l_c$) the radius and distance of the biggest satellite droplet scales with pattern dimension a to the power $p_r = 0.82$ and $p_d = 0.50$, respectively. For pattern dimensions larger than the capillary length ($a > l_c$) the pattern dimension scales with $p_r = 0.32, 0.38, 0.64$ and 0.82 corresponding to the dip-coating velocities $U = 0.25, 1, 3$ and $6\,\mathrm{mm/s}$ to the radius of the biggest satellite droplet, respectively. For the distance of the biggest satellite droplet the pattern dimension a scale with $p_d = 0.37, 0.53, 0.83$ and 0.78 corresponding to the dip-coating velocities $U = 0.25, 1, 3$ and $6\,\mathrm{mm/s}$.

For pattern dimensions larger than the capillary length ($a > l_c$) again the smallest dip-coating velocities show a significant decrease in scaling from approximately linear ($p_r = 0.82$) to $p_r = 0.32$ and $p_r = 0.38$ for $U = 0.25$ and $U = 1\,\mathrm{mm/s}$ for the radius of the biggest satellite droplet. Also the distance of the biggest satellite droplet shows a similar decrease in scaling from an exponent $p_d = 0.50$ to $p_d = 0.37$ for dip-coating velocity $U = 0.25$ for pattern dimensions larger than the capillary length $a > l_c$. The transition, which occurs around the capillary length $a \approx l_c$ for lower ($U < 1\,\mathrm{mm/s}$)) dip-coating velocities shifts to larger pattern dimensions for larger ($U > 3\,\mathrm{mm/s}$)) dip-coating velocities.

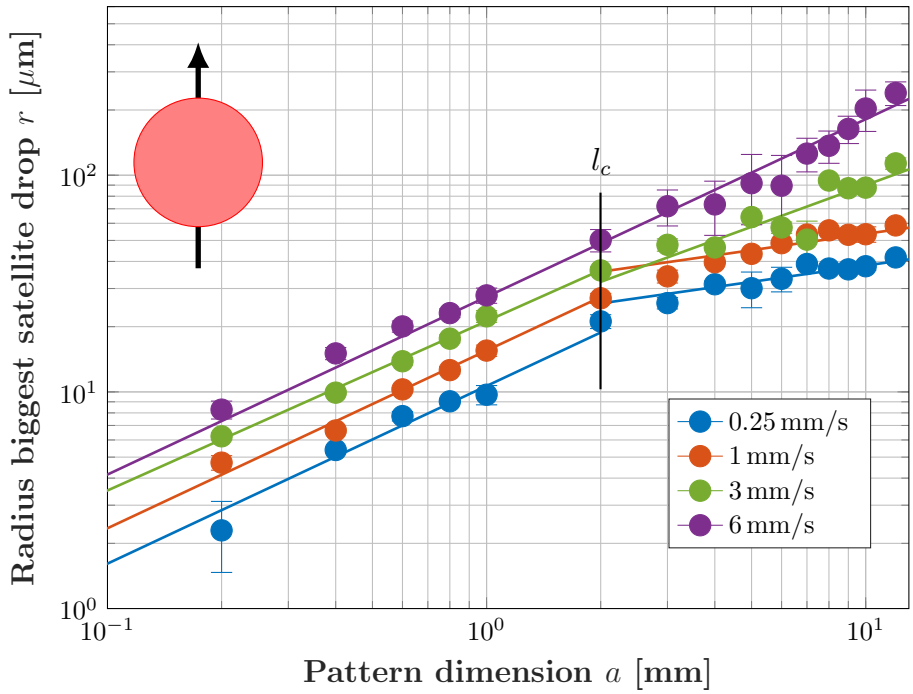

Figure 3.14: Radius of biggest satellite droplet versus the pattern dimension a for a circle pattern shape at different dip-coating velocities. The critical dip-coating velocity is given by $U_c = 6.5 \pm 0.5\,\mathrm{mm/s}$. The data is fitted with power laws for the pattern dimension a above and below the capillary length l_c. The exponent of the fit below the capillary length ($a < l_c$) is given by $p_r = 0.82$. The exponents of the fits above capillary length ($a > l_c$) are given by $p_r = 0.32, 0.38, 0.64$ and 0.82. The errorbars correspond to the standard deviation.

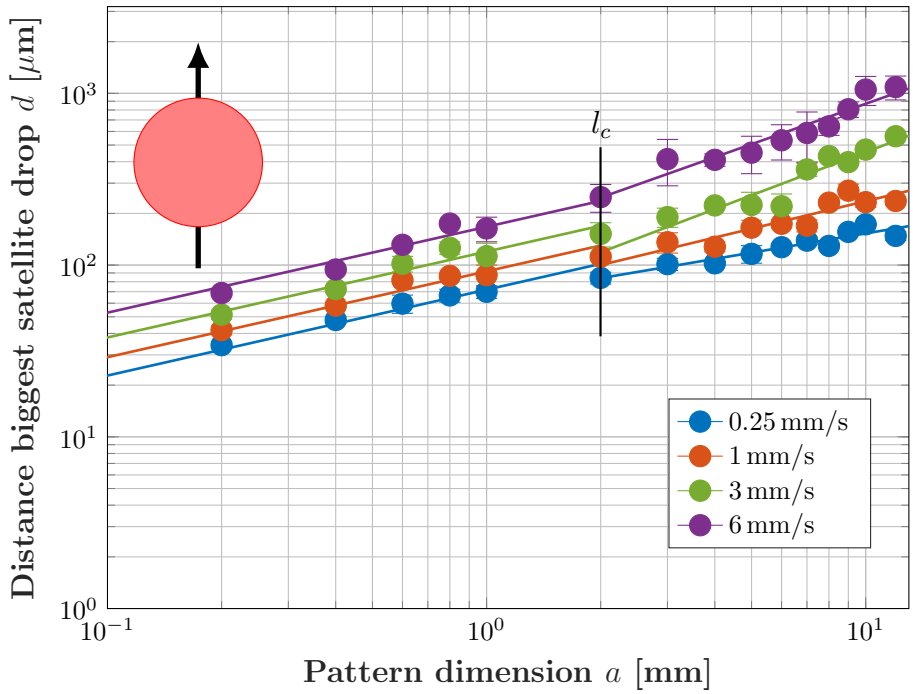

Figure 3.15: Distance of biggest satellite droplet versus the pattern dimension a for circle pattern shape at different dip-coating velocities. The critical dip-coating velocity is given by $U_c = 6.5 \pm 0.5\,\mathrm{mm/s}$. The data is fitted with power laws for the pattern dimension a above and below the capillary length l_c. The exponent of the fit below the capillary length ($a < l_c$) is given by $p_d = 0.50$. The exponents of the fits above capillary length ($a > l_c$) are given by $p_d = 0.37, 0.53, 0.83$ and 0.78. The errorbars correspond to the standard deviation.

Figures 3.16 and 3.17 show the radius and distance of the biggest satellite droplet as a function of the dip-coating velocity U for different pattern dimensions a. This is the same data as depicted in figures 3.14 and 3.15, but with the dip-coating velocity U and pattern dimension a switching places between legend and x-axis. Both figures still show an increase in dip-coating velocity U or pattern dimension a results in a larger and further displaced satellite droplet, however gives more detail in the influence of the dip-coating velocity U. For small pattern dimensions ($a < 6\,\mathrm{mm}$) the radius and distance of the biggest satellite droplet scale with $q_r = 0.28$ and $q_d = 0.18$, with small dip-coating velocities ($U < 2\,\mathrm{mm/s}$). For dip-coating velocities approaching the critical dip-coating velocity $U \to U_c = 6.5 \pm 0.5\,\mathrm{mm/s}$ exponential behaviour is observed. The exponential behaviour is quantified by fitting with equation (3.8) which yields $k_r \approx 0.12 \pm 0.02$ and $k_d \approx 0.14 \pm 0.07$. Both k_r and k_d are the mean of the individual parameters which are given in the caption. The error corresponds to the standard deviation of this mean. As also observed in figures 3.14 and 3.15 for higher pattern dimensions $a > l_c$ the observed scaling transition moves to lower dip-coating velocities U.

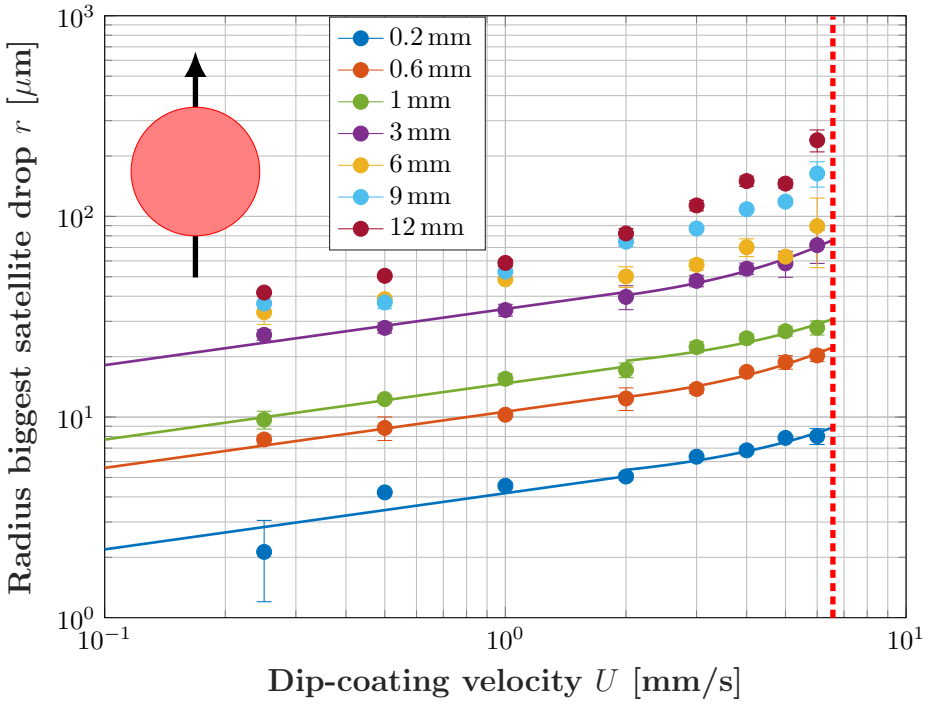

Figure 3.16: Radius of biggest satellite droplet versus the dip-coating velocity U for a circle pattern shape at different pattern dimensions a. The critical dip-coating velocity is given by $U_c = 6.5 \pm 0.5\,\mathrm{mm/s}$ illustrated by the dashed red line. The data is fitted with power laws for small dip-coating velocities $U < 2\,\mathrm{mm/s}$ and small pattern dimensions $a < 6\,\mathrm{mm}$. The exponent of these fits is given by $q_r = 0.28$. The data for big DC velocities $2 < U < U_c\,\mathrm{mm/s}$ and small pattern dimensions $a < 6\,\mathrm{mm}$ is fitted with an exponential fit which yields $k_r = 0.11, 0.13, 0.11, 0.14$ from $a = 0.2\,\mathrm{mm}$ to $a = 3\,\mathrm{mm}$. The errorbars correspond to the standard deviation.

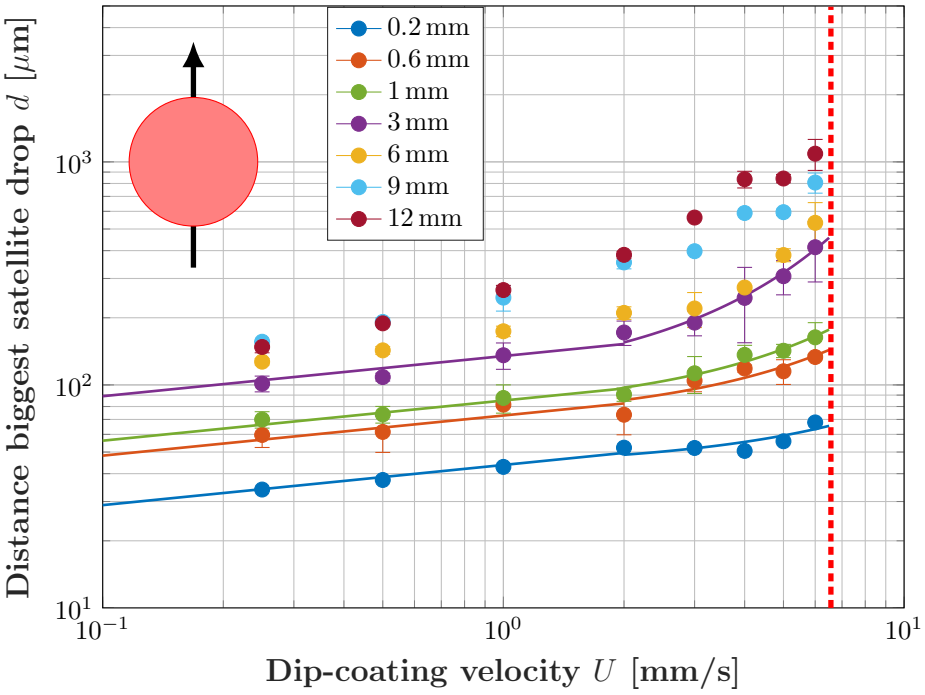

Figure 3.17: Distance of biggest satellite droplet versus the dip-coating velocities U for a circle pattern shape at different pattern dimensions a. The critical dip-coating velocity is given by $U_c = 6.5 \pm 0.5\,\mathrm{mm/s}$ illustrated by the dashed red line. The data is fitted with power laws for small dip-coating velocities $U < 2\,\mathrm{mm/s}$ and small pattern dimensions $a < 6\,\mathrm{mm}$. The exponent of these fits is given by $q_d = 0.18$. The data for big DC velocities $2 < U < U_c\,\mathrm{mm/s}$ and small pattern dimensions $a < 6\,\mathrm{mm}$ is fitted with an exponential fit which yields $k_d = 0.07, 0.12, 0.13, 0.24$ from $a = 0.2\,\mathrm{mm}$ to $a = 3\,\mathrm{mm}$. The errorbars correspond to the standard deviation.

3.2.4 Effect of dip-coating velocity

The graphs in previous paragraphs all show an increase in droplet radius and distance for increasing dip-coating velocities. For small dip-coating velocities $U < 2\,\mathrm{mm/s}$ and small pattern dimensions $a < l_c$ power laws predicts the scaling behaviour between the dip-coating velocity U and the radius and distance of the biggest satellite droplet given by $r \sim U^{q_r}$ and $d \sim U^{q_d}$. These scaling parameters q_r and q_d are summarized in table 3.5. For all shapes the radius and distance of the biggest satellite droplet scale with the small pattern dimension $a < l_c$ to the power $q_r = q_d \approx 0.2$ for small dip-coating velocities $U < 3\,\mathrm{mm/s}$. For higher dip-coating velocities $2 < U < U_c\,\mathrm{mm/s}$ exponential behaviour is observed, given by $r \sim e^{k_r U}$ and $d \sim e^{k_d U}$, of which the fit parameters are summarized in table 3.5.

Table 3.5: Summary of the scaling parameters derived from power law and exponential fits to the experimental dip-coating data in previous paragraphs 3.2.1, 3.2.2 and 3.2.3 for small pattern dimensions $a < 6\,\text{mm}$. The values of q_r and q_d correspond to the power law scaling for small DC velocities $0.25 < U < 2\,\text{mm/s}$, while the values of k_r and k_d correspond to the exponential fit parameters for higher DC velocities $2 < U < U_c\,\text{mm/s}$. The latter is defined by the mean over the different pattern dimensions including standard deviation.

Shape	Radius biggest satellite droplet r	Distance biggest satellite droplet d
Square	$q_r = 0.21$	$q_d = 0.20$
Triangle	$q_r = 0.18$	$q_d = 0.18$
Circle	$q_r = 0.28$	$q_d = 0.18$
Square	$k_r \approx 0.15 \pm 0.01$	$k_d \approx 0.17 \pm 0.02$
Triangle	$k_r \approx 0.09 \pm 0.04$	$k_d \approx 0.16 \pm 0.02$
Circle	$k_r \approx 0.12 \pm 0.02$	$k_d \approx 0.14 \pm 0.07$

With the graphs from previous paragraph in mind figure 3.18 shows snapshots of a square pattern with pattern dimension $a = 1\,\text{mm}$ and two different dip-coating velocities $U = 1$ and $U = 6\,\text{mm/s}$ moving through the meniscus. In both cases first the meniscus pins to the pattern as shown in figure 3.18(a) and (e). A liquid (or capillary) bridge is formed between the pattern and the liquid reservoir. While the sample moves further up the liquid bridge becomes more elongated and narrower due to the dewetting. At some point a thin rivulet remains, as depicted in figure 3.18(b) and (f). This thin rivulet breaks up in droplets due to Rayleigh-Plateau instabilities, as shown in figure 3.18(c) and (g). After the break-up of the rivulet the meniscus retracts to its original position and the droplets are left under the pattern as shown in figure 3.18(d) and (h).

The effect of the dip-coating velocity is best described by figure 3.18(b),(c),(f) and (g). The length and width of the rivulet, just before break up, increases for higher dip-coating velocities U. Due to the longer and thicker rivulet the break-up will also result in larger satellite droplets at a bigger distance from the pattern. This is also confirmed by the quantitative data.

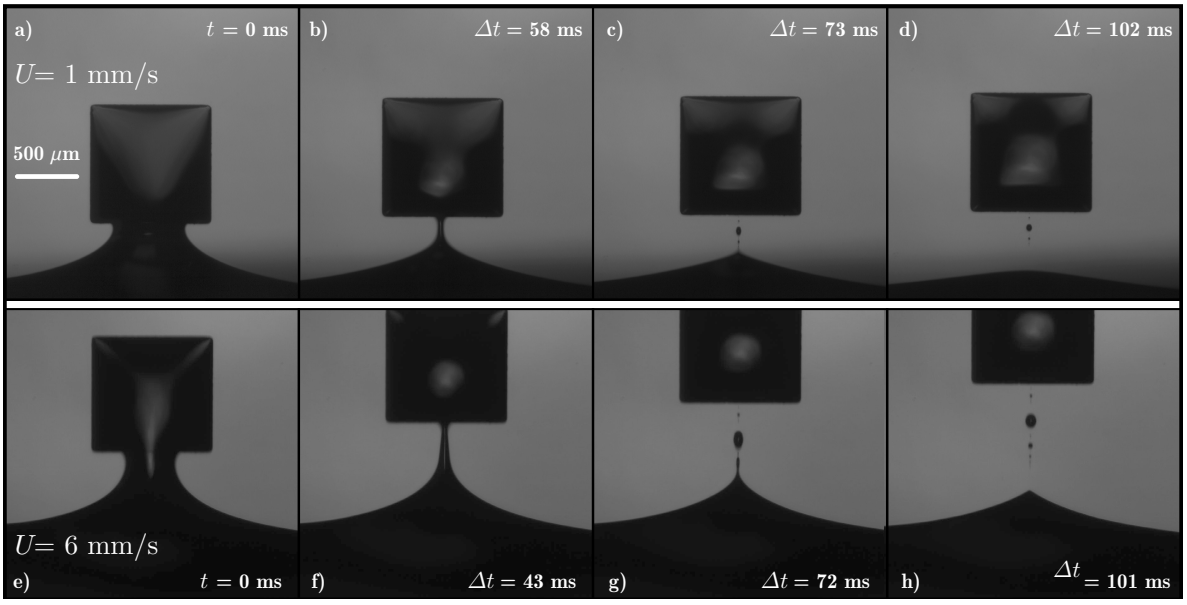

Figure 3.18: Snapshots of the captured break up process under the (black) square pattern with pattern dimension $a = 1\,\text{mm}$ at two different dip-coating velocities $U = 1\,\text{mm/s}$ (top) and $U = 6\,\text{mm/s}$ (bottom). In all snapshots the dip-coating direction is from bottom to top and the liquid reservoir is located in the bottom. In both videos $t = 0$ is arbitrarily set for the first frames (a) and (e).

3.2.5 Effect of pattern dimension

The graphs in previous paragraphs all show an increase in droplet radius and distance for increasing pattern dimension a. For small pattern dimensions $a < l_c$ power laws predicts the scaling behaviour between the pattern dimension a and the radius and distance of the biggest satellite droplet, namely $r \sim a^{p_r}$ and $d \sim a^{p_d}$. These scaling parameters p_r and p_d are summarized in table 3.6. For all shapes the radius and distance of the biggest satellite droplet scaling dependence decreases from $p_r = p_d \approx 0.9$ to $p_r = p_d \approx 0.2$ for the big pattern dimension $a > l_c$ and for small dip-coating velocities $U < 3\,\mathrm{mm/s}$. One possible causes for this is the more dominant role of gravitational forces for pattern dimensions $a > l_c$ which results in less liquid on the pattern for smaller DC velocities. Another possible cause is the retraction of liquid back onto the pattern which is illustrated in figure 3.19. In this figure the break up process under a square pattern with pattern dimension $a = 12\,\mathrm{mm}$ and DC velocity $U = 1\,\mathrm{mm/s}$ is visualized. The point where the liquid bridge breaks is now further displaced from the pattern edge [figure 3.19(a-b)]. The retraction of liquid in the liquid bridge onto the pattern is indicated by the arrows [figure 3.19(b-c)]. The retraction also pulls the liquid bridge slightly back to the pattern. This results in a smaller satellite droplet at a smaller distance from the pattern edge.

Table 3.6: Summary of the scaling parameters derived from power law fits to the experimental dip-coating data in previous paragraphs 3.2.1, 3.2.2 and 3.2.3 for dip-coating velocities U and small pattern dimensions $a < l_c$. The numbers correspond to the scaling parameter p_r and p_d in the radius and distance of the biggest satellite droplet $r \sim a_r^p$ and $d \sim a_d^p$, respectively.

Shape	p_r Radius biggest satellite droplet	p_d Distance biggest satellite droplet
Square	1.0	0.98
Triangle	0.89	0.90
Circle	0.82	0.50

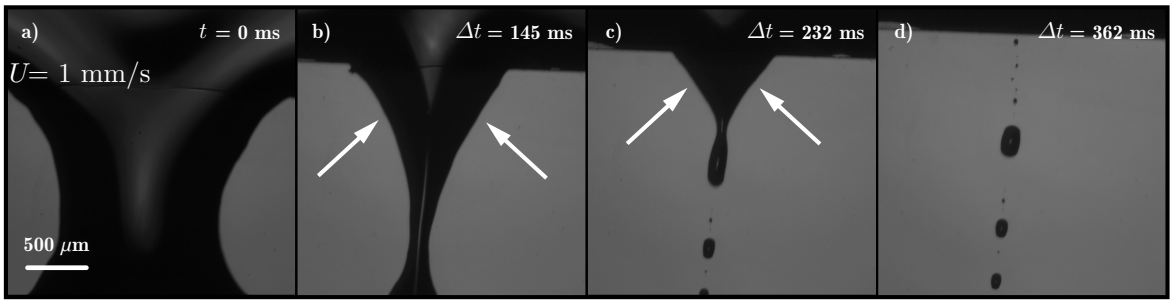

Figure 3.19: Snapshots of the captured break up process under the (black) square pattern with pattern dimension $a = 12\,\mathrm{mm}$ at dip-coating velocity $U = 1\,\mathrm{mm/s}$. The meniscus in all snapshots is located in the bottom. The time $t = 0$ is arbitrarily set for the first frame (a).

To visualize the break up in more detail snapshots are shown of a square pattern with pattern dimension $a = 7\,\mathrm{mm}$ and two different dip-coating velocities in figure 3.20. Comparing this to figure 3.18 shows that a larger pattern dimension results in a bigger liquid bridge, i.e. an longer and thicker rivulet just before break-up. The size of the rivulet just before break up is determined by the geometrical parameters of the pattern and the DC velocity. This would also explain the different scaling parameter for the distance as a function of the pattern dimension. The influence of shaped is discussed in more detail in the next paragraph 3.2.6.

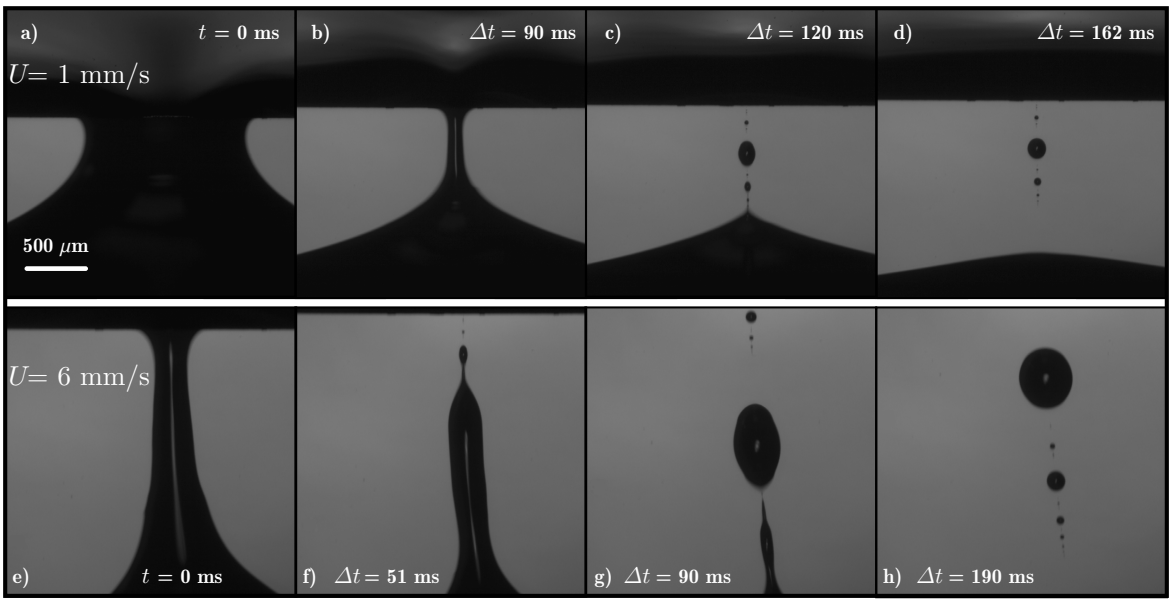

Figure 3.20: Snapshots of the captured break up process under the (black) square pattern with pattern dimension $a = 7\,\text{mm}$ at two different dip-coating velocities $U = 1\,\text{mm/s}$ (top) and $U = 6\,\text{mm/s}$ (bottom). The meniscus in all snapshots is located in the bottom. In both videos $t = 0$ is arbitrarily set for the first frames (a) and (e).

3.2.6 Effect of shape

In this paragraph the effect of the pattern shape is discussed. In figure 3.21 the radius of the biggest satellite droplet is plotted versus the pattern dimension a (a) and pattern area A (b) for the lowest and highest DC velocity and all shapes. The circular patterns show a significant decrease in radius for the same pattern dimension a and area A for both DC velocities compared to the squares and triangles. The data for the triangle and square shaped patterns overlap when plotted versus the pattern area A. A possible explanation for this is the similar shape of the bottom edge of the pattern, i.e. horizontal with sharp corners. Thus the pattern area A relates directly to the volume of liquid left on the pattern while the shape of the bottom edge determines the break-up of the liquid bridge. The smooth shape of the bottom edge for circular patterns could then be the cause for a relatively longer stable liquid bridge before break-up, while more liquid retracts back to the liquid reservoir and subsequently leaving a smaller satellite droplet. This is argument is in line when compared with the dynamics of the break-up process, of which snapshots are shown of a circle and square shaped pattern with pattern dimension $a = 4\,\text{mm}$ and DC velocity $U = 6\,\text{mm/s}$ in figure 3.23. The break-up from the circle shaped pattern results in a smaller liquid-bridge compared to the square shaped pattern.

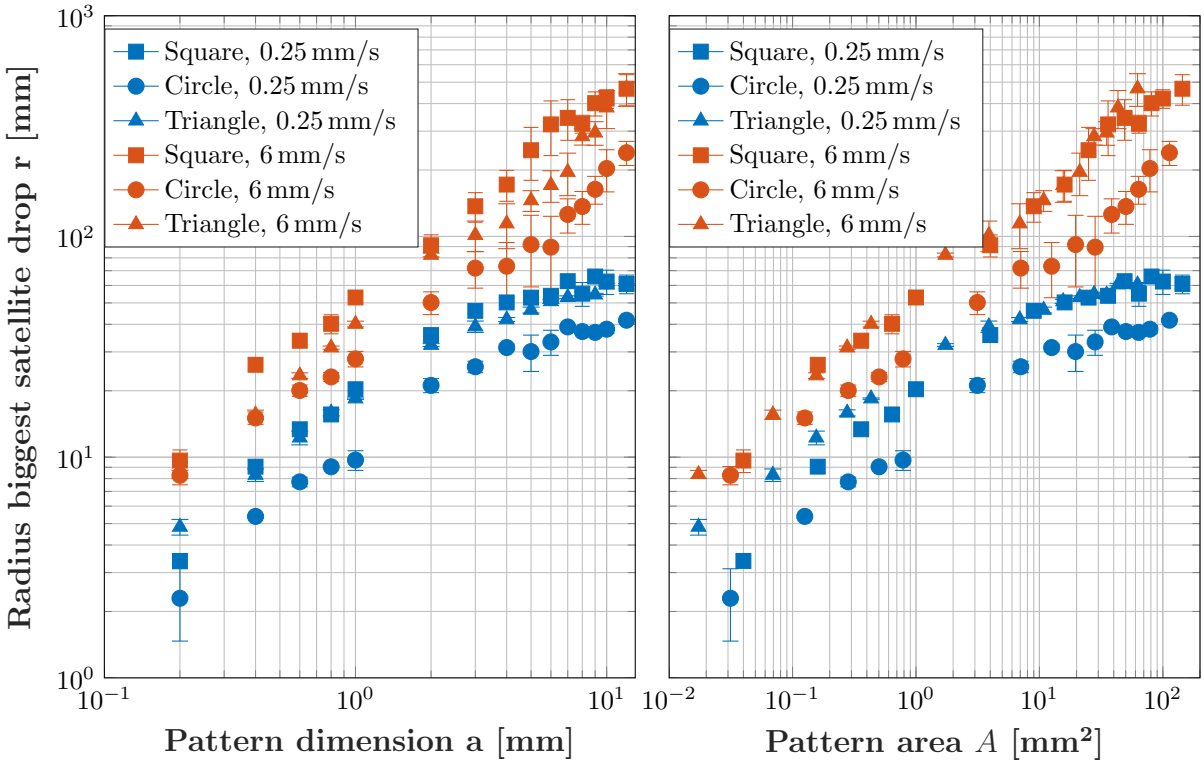

Figure 3.21: Radius of the biggest satellite droplet versus the pattern dimension a (a) and pattern area A (b) for square, circle and triangle shaped patterns at dip-coating velocities $U = 0.25$ and 6 mm/s. The critical dip-coating velocity is given by $U_c = 6.5 \pm 0.5$ mm/s.

In figure 3.22 the distance of the biggest satellite droplet is plotted versus pattern dimension a (a) and pattern area A (b) for the lowest and highest DC velocity and all shapes. The circular patterns show a significant decrease in distance of the largest satellite droplet for pattern dimensions roughly smaller than the capillary length $a < l_c$ and area A for both DC velocities compared to the squares and triangles. This observation is in line with the hypothesis of different effects of the pattern area A and bottom edge. The different shape of bottom edge for circular patterns would then also explain the difference in the scaling behaviour for distance versus pattern dimensions.

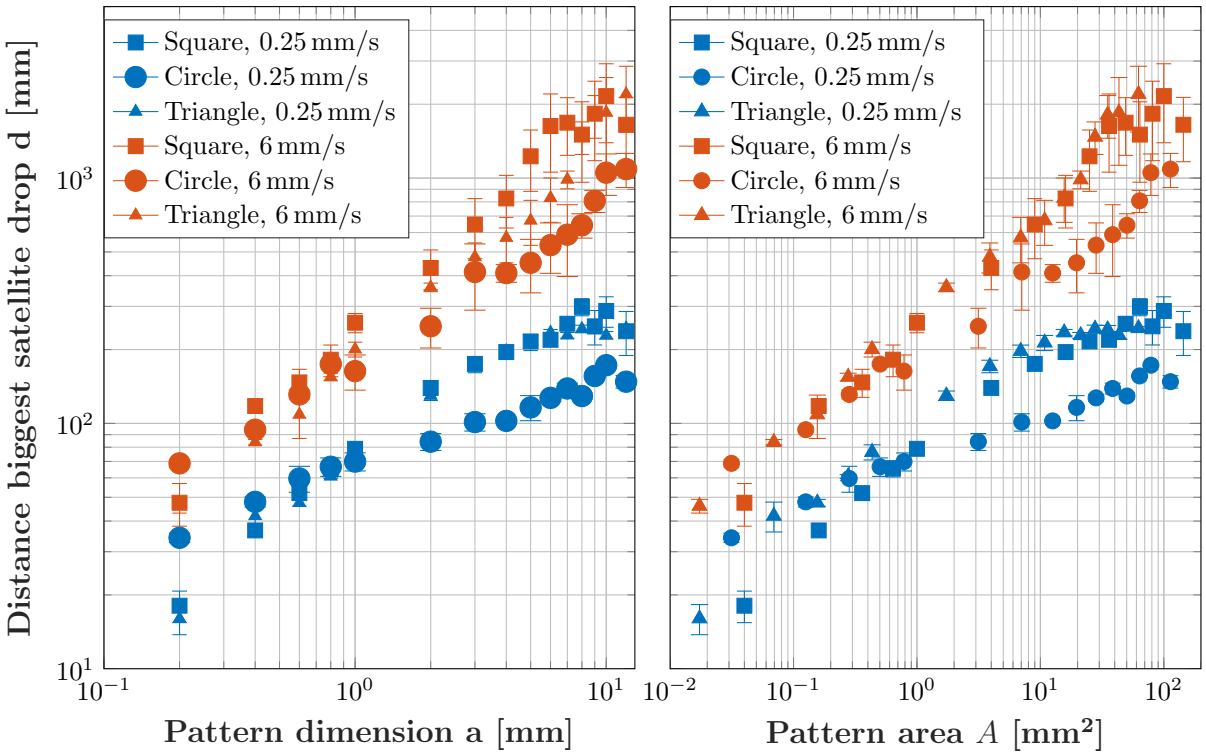

Figure 3.22: Distance of the biggest satellite droplet versus the pattern dimension a (a) and pattern area A (b) for square, circle and triangle shaped patterns at dip-coating velocities $U = 0.25$ and 6 mm/s. The critical dip-coating velocity is given by $U_c = 6.5 \pm 0.5$ mm/s.

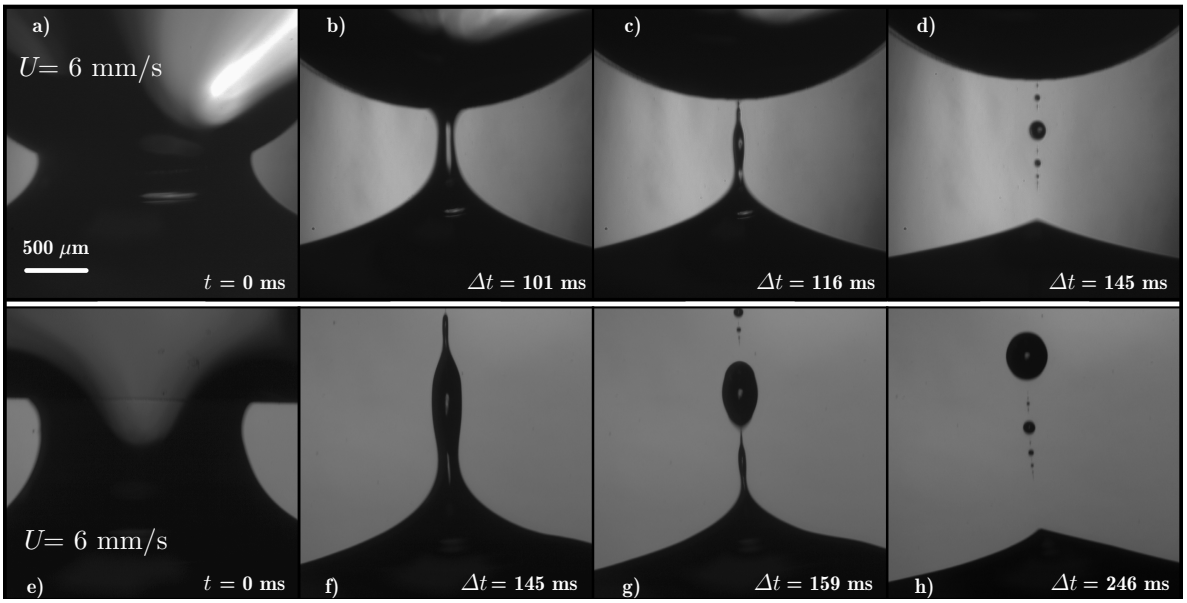

Figure 3.23: Snapshots of the captured break up process under a circle (top) and square (bottom) pattern with pattern dimension $a = 4$ mm at dip-coating velocity $U = 6$ mm/s. The meniscus in all snapshots is located in the bottom and the pattern is moving up. In both videos $t = 0$ is arbitrarily set for the first frames (a) and (e).

3.2.7 Decay of satellite droplets

Figure 3.24 shows the decay in radius of satellite droplets as a function of the droplet index N for different relative DC velocities U/U_c for pattern dimensions $a = 12$ mm (a) and $a = 0.8$ mm

(b). The fits resemble a power law given by:

$$r \sim N^{-p'}, \tag{3.9}$$

with p' the fit parameter. The power law fit parameters are given by $p' = 1.81$, 1.69, 1.78 and 1.94 from closest to the critical DC velocity $U/U_c = 0.92$ to $U/U_c = 0.077$ for pattern dimension $a = 12\,\text{mm}$. For pattern dimension $a = 0.8\,\text{mm}$ the fit parameters are given by $p' = 1.61$, 1.79, 2.13 and 2.39. Thus a slight increase in scaling magnitude is observed for decreasing dip-coating velocities. The only exception is $U/U_c = 0.92$ for $a = 12\,\text{mm}$, which could be due to the uncertainties. The increase in scaling magnitude is more distinct for the smaller pattern dimension $a = 0.8\,\text{mm}$.

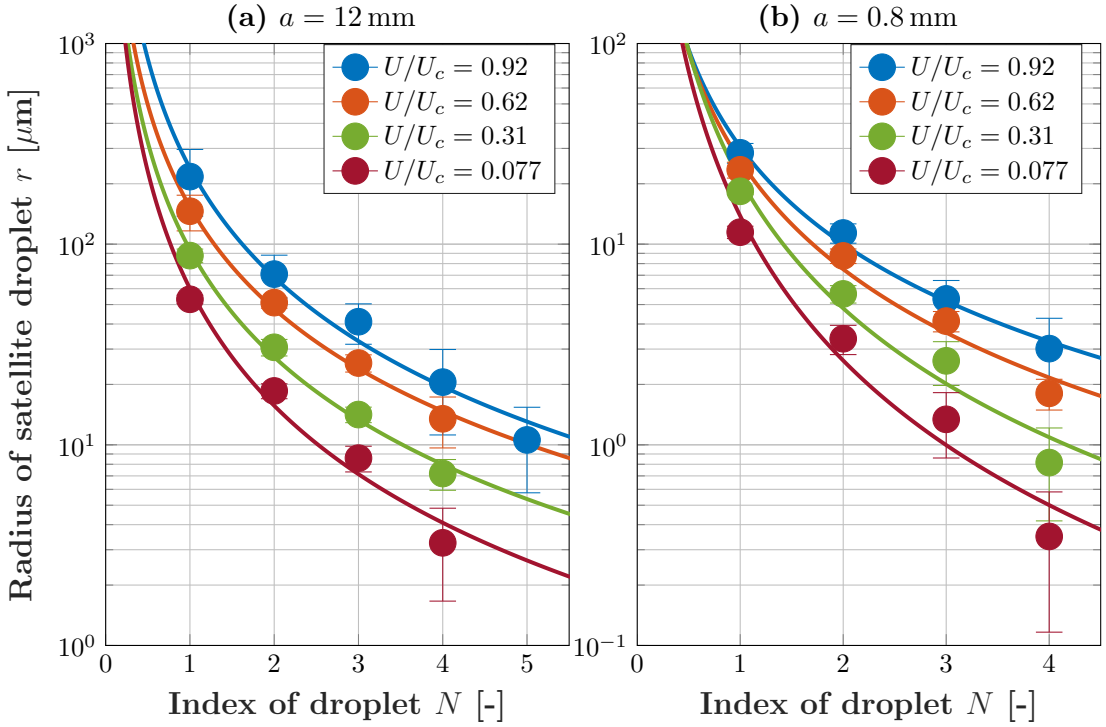

Figure 3.24: Radius of satellite droplet r as a function of the droplet index N for pattern dimensions $a = 12\,\text{mm}$ (a) and $a = 0.8\,\text{mm}$ (b). The power law fit parameters are given by $p' = 1.81$, 1.69, 1.78 and 1.94 from closest to the critical DC velocity $U/U_c = 0.92$ to $U/U_c = 0.077$ for pattern dimension $a = 12\,\text{mm}$. For pattern dimension $a = 0.8\,\text{mm}$ the fit parameters are given by $p' = 1.61$, 1.79, 2.13 and 2.39. Each point resembles an average of at least two measurements, where the errorbars denote the corresponding standard deviation plus droplet fit error. The critical DC velocity is given by $U_c = 6.5\,\text{mm/s}$.

3.3 Summary and conclusions

In this chapter the liquid entrainment process by a single heterogeneity on partially wettable substrates dip-coated from a liquid reservoir has been discussed. The heterogeneities consist of photo-lithography defined defects with a certain shape, and pattern dimension a. The meniscus pins onto the defect and liquid entrains. When the defects moves further up the entrained liquid forms a liquid bridge between the pattern which breaks due to the Rayleigh-Plateau instability leaving a trail of satellite droplets. Systematic experiments are done by varying the pattern shape (circles, squares and equilateral triangles), pattern dimensions a and dip-coating velocity U. The liquid entrainment process is studied by both quantifying the radius and distance of the biggest satellite droplet and capturing the dynamics of the break-up process with the camera. Also the decay in size of the trail of droplets is analysed.

For all shapes an increase dip-coating (DC) velocity or pattern dimensions results in a larger radius and distance of the satellite droplet. A transition occurs when the pattern dimension a approximately equals the capillary length l_c. For all shapes the radius and distance scale roughly linear ($\approx a^{0.9}$) with the pattern dimension for pattern dimensions smaller than the capillary length $a < l_c$. The only exception is the circular patterns where the distance scales with $d \sim a^{0.5}$. A possible cause for this is the different bottom shape for the circular patterns For pattern dimensions larger than the capillary length $a > l_c$ a decrease in dependence a^p is observed from roughly linear $p \approx 0.9$ to $p \approx 0.2$. The decrease in dependence is less distinct for larger dip-coating velocities $U/U_c \to 1$, i.e. closer to the critical DC velocity. Two possible causes are the retraction of liquid back onto the pattern after the liquid bridge breaks up, which is less distinct for larger DC velocities, and the bigger influence of gravity on the smaller DC velocities.

For all shapes the radius and distance scale roughly with $\sim U^{0.2}$ for smaller pattern dimensions $a \leq 3\,\text{mm}$ and small DC velocities $U/U_c < 0.4$. For larger DC velocities $0.4 < U/U_c < 1$ (and same small pattern dimensions) exponential behaviour is observed, where the radius and distance roughly scale with $\sim e^{0.14U}$. The decrease in scaling for pattern dimensions at low DC velocities $U/U_c < 0.4$ and large pattern dimensions $a > l_c$ is represented by the collapse of the distance and radius data for all patterns.

Comparing between shapes concludes that equilateral triangle and square defects leave bigger satellite droplets at a larger distance for same DC velocities and pattern dimensions than circular defects. The main cause is the gradual slope of the pattern edge versus the abrupt corner of the square and triangle patterns. The hypothesis is that the pattern area influences the volume of liquid while the shape of the bottom edge of the pattern determines the duration of the liquid bridge break-up. This would explain the data overlap for square and triangle shaped patterns when the radius and distance are plotted versus the pattern area. The lower values of radius and distances for same pattern areas or dimensions is then explained by the smooth bottom edge of the pattern which leads to a relatively longer stable liquid bridge compared to the other shapes with similar pattern dimensions or areas. Thus more entrained liquid is retracted back into the liquid reservoir before the break up of the liquid bridge. Since only three shapes are compared with the triangle and square having a similar bottom edge of the pattern, i.e. horizontal with sharp corners, more research is necessary to conclude the individual effects of the pattern area or dimensions versus the bottom edge of the pattern.

The decay of droplet radius in the trail below a circular pattern follows a power law given by $r \sim N^{-p'}$ with N the droplet index. The scaling magnitude p' increases for decreasing DC velocities.

Chapter 4

Numerical model for dip-coating

The goal of this chapter is to complement the dip-coating results with numerical simulations. First in section 4.1 an overview of the governing equations, the corresponding numerical setup is given and the validation of the model is discussed. In section 4.2 the influence of the geometrical parameters of the defect on the pinning and film pulling is studied by 1D models. In section 4.3 the numerical results of 2D dip-coating simulations are presented and discussed. Finally in section 4.4 a summary and conclusions are given.

4.1 Numerical setup

The dip-coating experiments are complemented by a numerical model based on the lubrication approximation (equation (2.45)) which yields the film thickness $h(x, y, t)$. Although the lubrication approximation is limited to small slopes of the liquid-air interface it can be used to study the break-up process caused by a surface heterogeneity on the dip-coated surface. A major advantage of using the lubrication approximation is that the model directly solves for the film thickness h, thus 3D information is given while two dimensions are solved. An illustration of the numerical domain is depicted in figure 4.1 with substrate (gray), meniscus (blue) and surface heterogeneity (red). The initial and boundary conditions will be discussed in the next paragraph 4.1.1. To model the topographic defect on the flat substrate the equation for the location of the liquid air interface $h'(x, y, t)$ is given by (equation (2.44)):

$$h'(x, y, t) = h(x, y, t) + s(x, y, t), \tag{4.1}$$

with $h(x, y, t)$ the film thickness and $s(x, y, t)$ the substrate height. The governing equation, i.e. the lubrication equation, is given by (equation (2.45)):

$$\frac{\partial h}{\partial t} + \frac{\partial}{\partial x}\left[\frac{-h^3}{3\mu}\left(\frac{\partial P}{\partial x}\right)\right] + \frac{\partial}{\partial y}\left[\frac{-h^3}{3\mu}\left(\frac{\partial P}{\partial y} + Uh\right)\right] = 0, \tag{4.2}$$

with μ the dynamic viscosity, U the dip-coating velocity and P the pressure defined by:

$$P = \left(\frac{\partial^2}{\partial x^2} + \frac{\partial^2}{\partial y^2}\right)\left(-\gamma h'\right) + \rho g y - \Pi. \tag{4.3}$$

Where γ denotes the surface tension, ρ the density, g the gravitational acceleration and Π the disjoining pressure. The relevant liquid parameters are set to $\mu = 1\,\mathrm{Pa}\cdot\mathrm{s}$, $\gamma = 64\,\mathrm{mN/m}$ and $\rho = 1.2\,\mathrm{g/cm^3}$. The disjoining pressure, discussed in (section 2.4) is implemented to model the

moving contact line. An empirical model composed of a long-range attractive and a short-range repulsive potential is used (equation (2.10)):

$$\Pi = \gamma\,(1-\cos\theta)\,\frac{(n-1)(m-1)}{n-m}\frac{1}{h^*}\left[\left(\frac{h^*}{h}\right)^n - \left(\frac{h^*}{h}\right)^m\right] \tag{4.4}$$

with n and m two constants and $\theta(x,y,t)$ the contact angle. The precursorlayer thickness h^* should be chosen much smaller than the thickness of the pulled film in the models. This precursorlayer h^* regularizes the stress singularity associated with a moving contact line. Which parameters are chosen for the disjoining pressure model will be discussed in the validation paragraph 4.1.2.

These governing equations are solved via a finite element discretization method (FEM) using COMSOL Multiphysics (version 3.5a). This means the computational domain is subdivided into finite elements of geometrically simple shapes (lines in 1D and triangles in 2D). The collection of these finite elements filling the computational domain is called the mesh, which will be further discussed in paragraph 4.1.2. The partial differential equations (PDEs) that describe the physics are then approximated for each element by polynomials. Due to the non-linearity of the governing equations it is important to find the right balance between computational time and model accuracy.

Two main models are used for the results in this thesis. The 1D model where the computational domain consists of a line in the y-direction (see figure 4.1) with length $L = 3\,\text{mm}$. In equations (4.2) and (4.3) all the terms involving the spatial coordinate x naturally are left out of this model. The 2D model consists of half the computational domain depicted in figure 4.1 by using the symmetry of the defect. Due to the symmetry boundaries in theory an array of defects is simulated with an center-to-center spacing $b = D$. To make sure the simulations of a single defect are not influenced by this the width of the computational domain $D/2$ has to chosen be sufficiently large. In this study the width of the computational domain is set to $D/2 = 4a$.

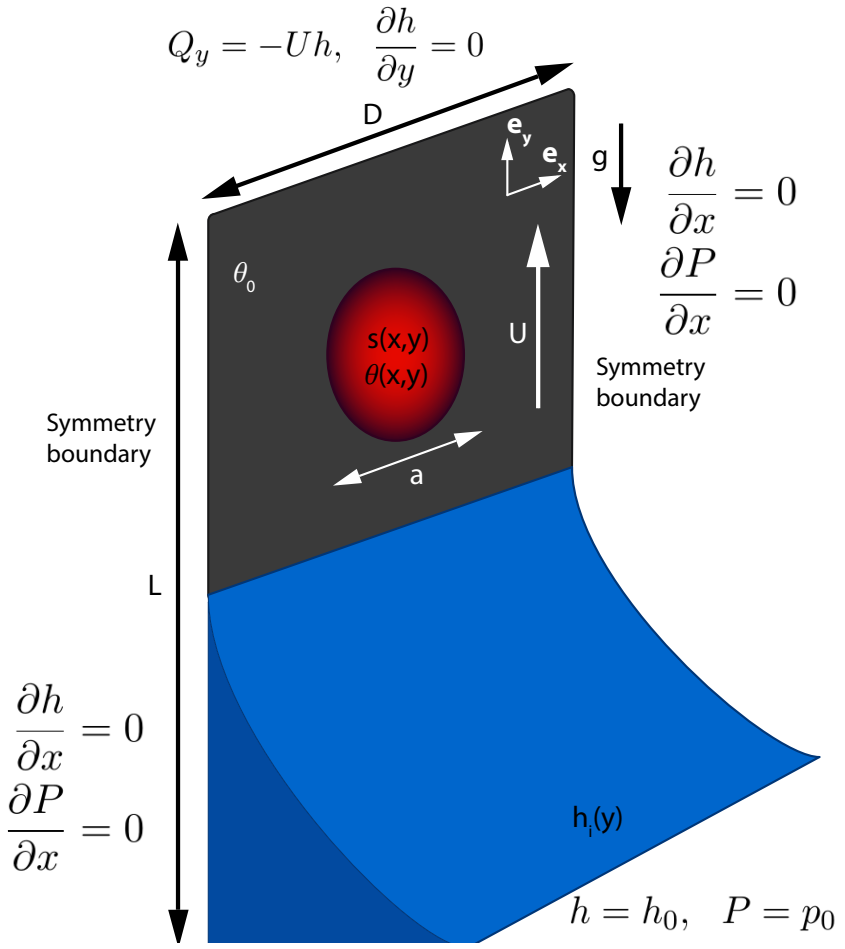

Figure 4.1: Illustration of the numerical domain for a typical 2D simulation showing the meniscus $h_i(y)$ in the bottom (blue), substrate (gray) and pattern (red). The substrate has a fixed contact angle of θ_0. The pattern can have a topographic $s(x, y)$ and a chemical $\theta(x, y) \leq \theta_0$ component with a pattern dimension of a. The boundaries and initial conditions are stated in equations (4.5a) - (4.9). For dip-coating gravity is directed in the negative y direction as indicated by the arrow.

4.1.1 Boundary & initial conditions

Now the physics for the model is set by equations (4.2) - (4.4) the boundary and initial conditions for the computational domain have to be implemented.

The boundary conditions are given per boundary as depicted in figure 4.1. The left and right ones are symmetry boundaries:

$$\frac{\partial h}{\partial x}(x = 0) = \frac{\partial h}{\partial x}(x = D/2) = 0, \tag{4.5a}$$

$$\frac{\partial P}{\partial x}(x = 0) = \frac{\partial P}{\partial x}(x = D/2) = 0. \tag{4.5b}$$

The top boundary represents a flat film leaving the numerical domain with a uniform speed along its film thickness direction:

$$Q_y(y = L) = -Uh, \quad \frac{\partial h}{\partial y}(y = L) = 0, \tag{4.6}$$

where the vertical influx is defined as $Q_y = -\frac{h^3}{3\mu}\frac{\partial P}{\partial y} - Uh$. The bottom boundary conditions set the local film thickness and local pressure, respectively:

$$h(y=0) = h_0 = 100\,\mu\text{m}, \quad P(y=0) = p_0. \tag{4.7}$$

The local pressure $P = p_0$ is given by the analytic result for a static meniscus adhering to a partially wetting wall inclined at an angle $\alpha = 90^o$ with respect to the horizontal:

$$p_0 = -\sqrt{2\gamma\rho g\,[1 - \cos(\alpha - \theta_0)]}. \tag{4.8}$$

From the edge of the bottom boundary the film thickness decays from the local film thickness h_0 to the precursorlayer thickness h^* as described by the stationary meniscus $h_i(y)$. The stationary meniscus $h_i(y)$ is initially determined, without influence of a defect, by the substrate velocity U, contact angle θ_0 and liquid parameters. For 1D simulations the initial meniscus profile is first given by a straight line, which estimates the meniscus in equilibrium:

$$h_i(y) = h_0 - \left(\frac{h_0 - h^*}{6 \cdot 10^{-4} \cdot y}\right) \cdot H(6 \cdot 10^{-4} - y) + h^*, \tag{4.9}$$

with $h_0 = 100\,\mu$m and $H(y)$ a smooth step function which arranges for a smooth transition between the contact line and substrate. The equilibrated state is reached in a few time steps maximum without much loss in computational time for the 1D models. To minimize computational time for the 2D models the equilibrated initial meniscus in a 1D models is imported. Since the equilibrated initial meniscus depends on the substrate velocity U several menisci shapes are extracted from 1D models as input for the 2D models, when the DC velocity U is varied.

The motion of the defect is represented by a time-dependent contact angle distribution $\theta(x, y - Ut)$ and time-dependent substrate height $s(x, y - Ut)$. Thus in each simulation the chemical $\theta(x, y - Ut)$ and topographic $s(x, y - Ut)$ component can individually be set. In this study two different defects are considered, namely the flat and Gaussian shaped defect. For the time-dependent substrate height $s(x, y - Ut)$ this is:

$$s(x, y - Ut) = s_0 \exp\left[-\frac{x^2 + (y - Ut)^2}{a^2}\right], \tag{4.10a}$$

$$s(x, y - Ut) = \frac{s_0}{2} + \frac{s_0}{2} \tanh\left[\frac{1}{c}\left(a - \sqrt{(x - x_0)^2 + (y - y_0 - Ut)^2}\right)\right], \tag{4.10b}$$

set for the Gaussian and flat bump, respectively. With the defect height s_0, defect width a and transition length c as defined in figure 4.2(a-b). For a flat substrate, i.e. no defect, the substrate height is set to $s = s_0 = 0$.

In the numerical work both topographic and topographic plus chemical defects are considered. For the Gaussian and flat defect the time-dependent contact angle distribution $\theta(x, y - Ut)$ is respectively set:

$$\theta(x, y - Ut) = \theta_0 - \frac{\theta_0}{2} \exp\left[-\frac{x^2 + (y - Ut)^2}{a^2}\right], \tag{4.11a}$$

$$\theta(x, y - Ut) = \theta_0 - \left(\frac{\theta_0}{4} + \frac{\theta_0}{4}\right) \tanh\left[\frac{1}{c}\left(a - \sqrt{(x - x_0)^2 + (y - y_0 - Ut)^2}\right)\right], \tag{4.11b}$$

with θ_0 substrate-liquid contact angle. The rest of the parameters such as the width a and transition length c correspond to the topographic substrate height distributions in equations and figure 4.2(c-d). When no defect is present or only a topographic defect is simulated the time-dependent contact angle distribution reduces to $\theta = \theta_0$.

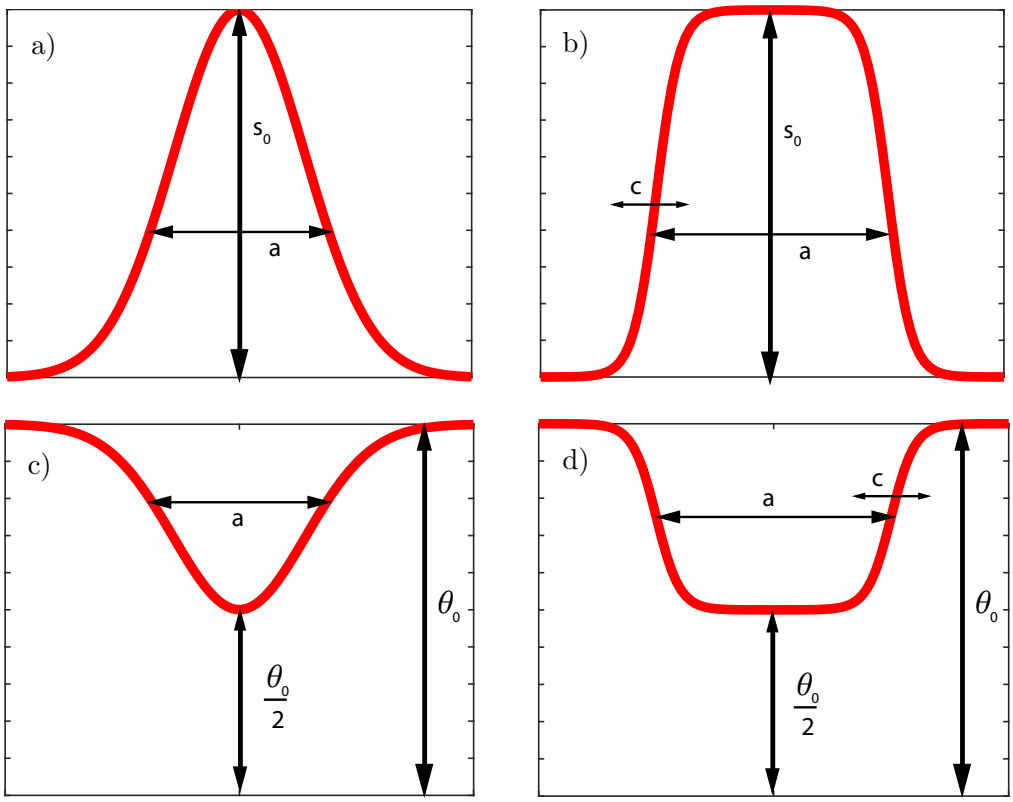

Figure 4.2: Cross sections of the substrate height distribution for a Gaussian (a) and flat (b) defect. The corresponding contact angle distributions are given by (c) and (d) for the Gaussian and flat defect, respectively. These are cross section plots from equations (4.10a) - (4.11b).

4.1.2 Validation

As with any numerical model its validity must be checked. The first question is if the physics is incorporated correctly in the model. The second if the model incorporates the physics correctly the discretization parameters must be set where a trade off between computational time and accuracy must be found. One can choose a very fine discretization, i.e. element size but this would lead to big computational times but very accurate results. As opposed to a coarse discretization which would lead to small computational times but less accurate results. So first the physics is validated by comparing the model to known laws and physics. Second the element size is varied and its influence on the results is tested.

To get an idea of the importance of the phenomenological disjoining pressure model the critical dip-coating velocity U_c is plotted non-dimensionalized by the critical capillary number $Ca_c = \mu U_c/\gamma$ versus the contact angle θ for different model parameters n, m and h^* in figure 4.3. The critical capillary number or critical dip-coating velocity is found by gradually increasing the dip-coating velocity till liquid is entrained by the moving substrate. Theoretically the critical capillary number Ca_c scales with (equation (2.8)):

$$Ca_c \sim \theta^3 \tag{4.12}$$

as predicted by Cox-Voinov law. The data is fitted with a similar power law, $Ca_c \sim \theta^{q'}$, with fit parameters q' in the legend. Although the differences between fit parameters q' is relatively small the choice of input parameters for the disjoining pressure model has an influence on the necessary minimum element size and computational time. A higher order polynomial will cost more computational time due higher non-linearity. A smaller precursorlayer h^* also results in an increase in computational time due to the smaller necessary discretization. Therefore the

model with the lowest order of polynomials is chosen ($n = 3$ and $m = 2$) with a precursorlayer of $h^* = 10\,\text{nm}$.

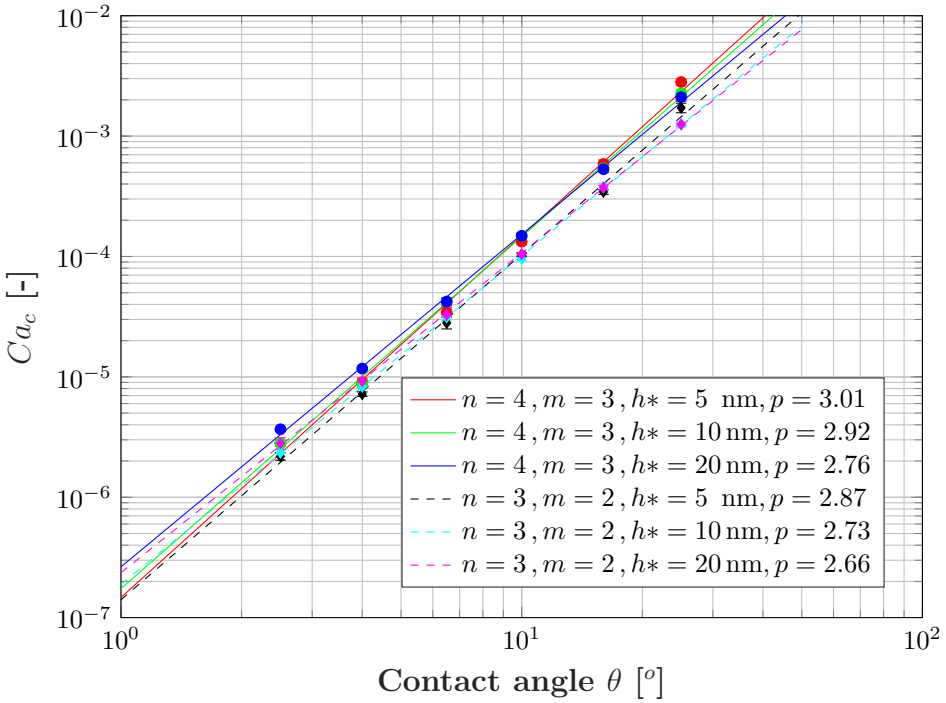

Figure 4.3: Logarithmic plot of the critical capillary number Ca_c versus contact angle θ for different disjoining pressure model parameters. The fits all resemble equation (4.12) with a mean $q' = 2.8 \pm 0.1$ for the lower order polynomials $n = 3$ and $m = 2$. For the higher order polynomials, $n = 3$ and $m = 2$, the mean is given by $q' = 2.9 \pm 0.1$. The error is the standard deviation.

Now that the model parameters for the disjoining pressure model are set, the mesh parameters are optimized. In figures 4.4 and 4.5 the film break up position and dewetting speed are plotted versus element size, respectively. In both figures all the data points represent a 1D dip-coating model of a topographic defect defined by equation (4.10a) with $s_0 = 1\,\mu$m and $a = 10\,\mu$m moving through the meniscus with super-critical velocity $U > U_c$, i.e. a film is pulled. For this model the element size is varied and the pulled film break up position and dewetting speed are analysed. The film break up position increases for smaller element sizes and converges for decreasing element sizes. The dewetting speed shows independence of element size, except for coarse discretization where film breaks up immediately after the defects moved through the meniscus. At this point it is hard to determine the dewetting speed since there is no film retracting, but a meniscus equilibrating after the defect moved through.

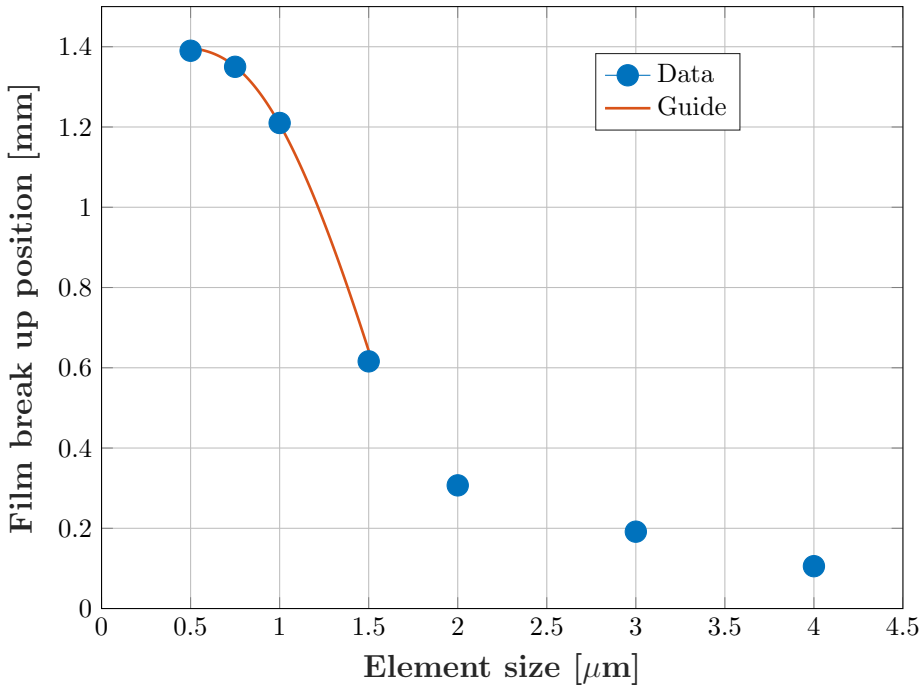

Figure 4.4: Plot of the film break up position of a pulled film for a super-critical ($U > U_c$) simulation, with a Gaussian shaped topographic defect moving through the meniscus, as a function of element size. The topographic defect is defined by equation (4.10a) with $s_0 = 1\,\mu$m and $a = 10\,\mu$m. The contact angle is given by $\theta = \theta_0 = 5^o$. The red line serves as a guide to the eye.

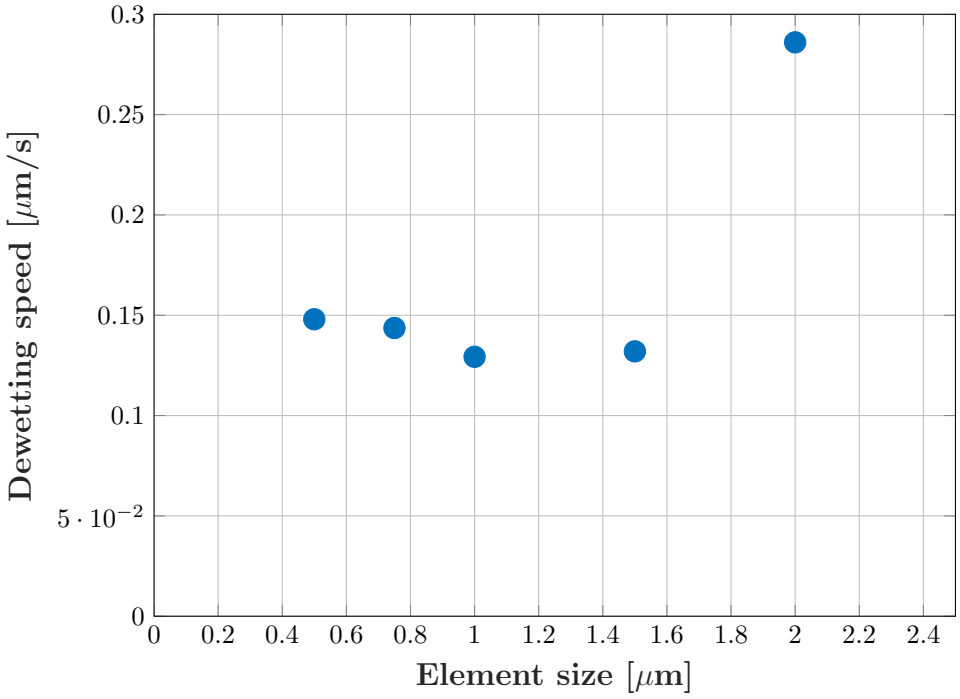

Figure 4.5: Dewetting speed after break up of the pulled film after the Gaussian shaped topographic defect moved through the meniscus, as a function of element size. The dewetting speed is analysed by extracting two coordinates of the film front at two different times during the retraction of the film. Dividing the displacement by the time difference gives the dewetting speed. The contact angle is given by $\theta = \theta_0 = 5^o$.

For the 1D simulations optimum element sizes $ES < 1\,\mu$m can be chosen without losing

much computational time. Having an element size of $ES < 1\,\mu$m for 2D simulations is not feasible, since this fine discretization together with the non-linearity of the governing equations results in huge computational times (months, years). Therefore the computational domain is divided in smaller areas where in each of these areas a mesh size is set. Around the regions of interest, i.e. the defect, the contact line and break up regions, a smaller element size is chosen as depicted in figure 4.6, where the different mesh domains are shown with corresponding element sizes. With a domain length $L = 900\,\mu$m and width $W/2 = 400\,\mu$m this results in a roughly in a number of 82000 elements and $DOF = 330000$ degrees of freedom.

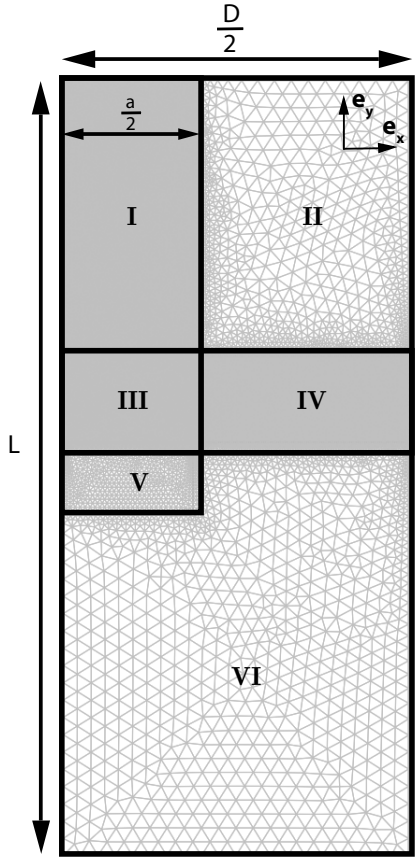

Mesh domain	Element size [μm]
I	1.8
II	20
III	1.4
IV	2.5
V	6
VI	20

Figure 4.6: Overview of different mesh domains for the 2D dip-coating model with corresponding element sizes given in the table. The predefined meniscus decays from the bottom, where $h = h_0$, of the domain till $h = h^*$ in mesh domains III and IV. The defect moves through domains V, III and I, respectively with width $a/2$. In domain I the liquid bridge breaks up and the formation of the satellite droplet is simulated.

4.2 Effect of geometrical parameters defect

In this section the influence of the defect shape is studied by letting 1D Gaussian shaped topographic defects move through the meniscus. The 1D defects are varied in height s_0, width a and orientation (bump $s_0 > 0$ or groove $s_0 < 0$). The maximum slope for the defect is then proportional to s_0/a. The effect of the (maximum) defect slope on the decrease in critical capillary number Ca_c and on the film thickness h for super-critical dip-coating velocities is studied.

First the effect on the decrease in critical capillary number Ca_c where for each variation in defect the critical dip-coating velocity U_c is found by iterating for different dip-coating velocities. Figure 4.7 illustrates the sub-critical $U < U_c$ and film pulling (super-critical) regimes $U > U_c$.

In all simulations the contact angle is set to $\theta = \theta_0 = 5^o$. For a flat surface the critical dip-coating velocity is found to be $U_c = 0.90\,\mu$m/s, which yields a critical capillary number of $Ca_c = 1.41 \cdot 10^{-5}$ (red line).

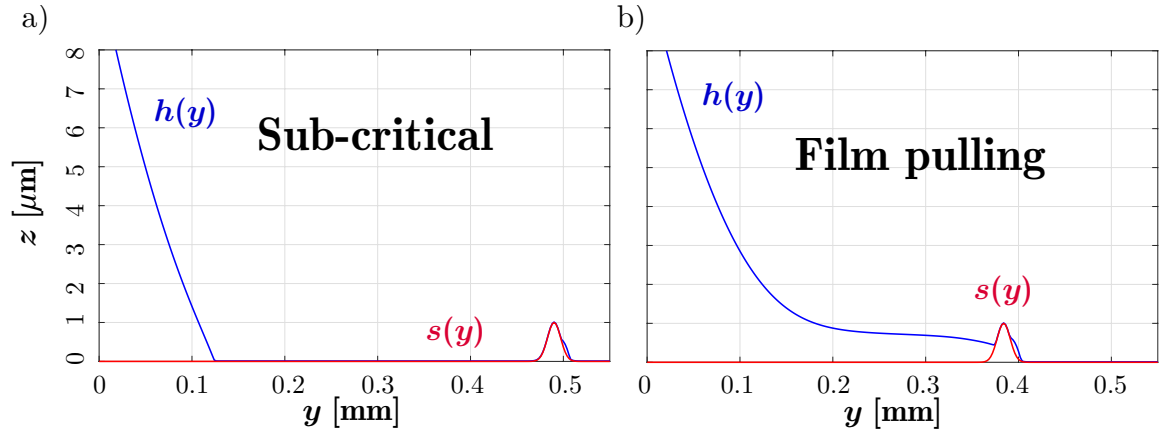

Figure 4.7: Illustration on sub-critical (a) and film pulling regimes (b) for dip-coating velocities U below and above the critical dip-coating velocity U_c. The blue lines corresponds to the film thickness $h(y)$ and red lines to the substrate height $s(y)$.

The critical dip-coating velocity U_c, for which pinning occurs and liquid entrains, is extracted and plotted non-dimensionalized by the capillary number Ca_c as a function of maximum slope s_0/a in figures 4.8 and 4.9, for the bump and groove, respectively. The blue squares and orange triangles correspond with Gaussian defects with constant height $s_0 = 1\,\mu$m and constant width $a = 10\,\mu$m, respectively. The errorbars correspond to the iterating step size with which U_c is identified. The extracted critical dip-coating velocities U_c are compared with the critical dip-coating velocity (red line) for which entrainment occurs even without a defect present on the substrate, i.e. flat surface.

For the Gaussian bump a decrease in critical capillary number Ca_c is observed between maximum slopes $0.06 < \frac{s_0}{a} < 0.15$. For maximum slopes $\frac{s_0}{a} > 0.15$ no further decrease in critical capillary number is observed. The slope of the peak influences the pinning feature since keeping the slope constant and varying the width and height gives similar critical capillary numbers Ca_c.

For the Gaussian groove also a decrease in critical capillary number Ca_c is observed however less distinct compared to the Gaussian bump, which is comparable with the smaller critical sliding angle of sliding droplets moving down an inclined surface with a Gaussian surface defect (theory section 2.7). The data does not show similar critical capillary numbers Ca_c for similar slopes magnitude but varying the width and height of the defect which might be caused by groove filling up quickly for small widths by the capillary action.

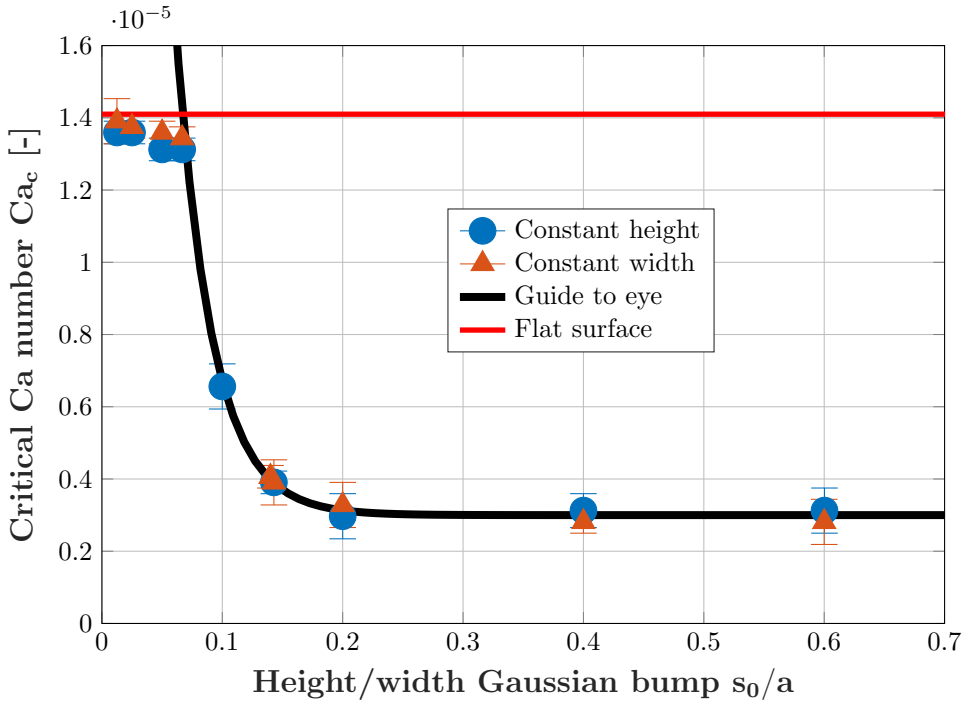

Figure 4.8: Critical Capillary number Ca_c as a function of the height over width of the positive Gaussian topographic defect (bump) s_0/w for which the height is held constant $s_0 = 1\,\mu$m (blue circles) and width $w = 10\,\mu$m is held constant (orange triangles). The topographic defect $s(y - Ut)$ is defined by equation (4.10a) with $x = 0$. The contact angle is given by $\theta = \theta_0 = 5^o$. The red horizontal line illustrated the critical capillary number for which entrainment occurs on a flat surface, i.e. without defect. The black line serves as a guide to the eye.

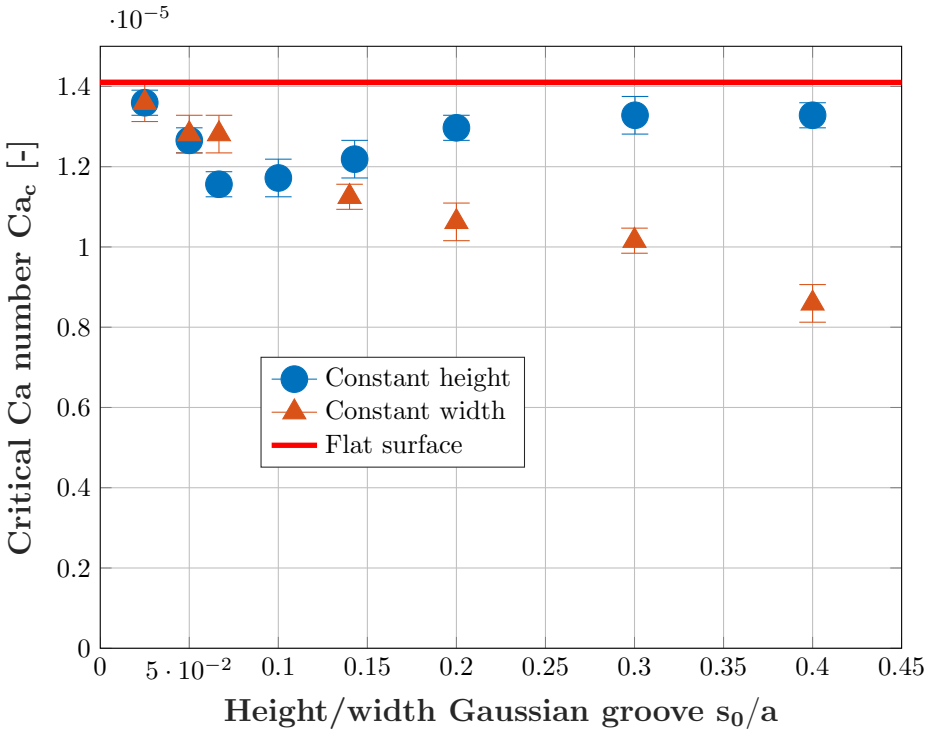

Figure 4.9: Critical Capillary number Ca_c as a function of the height over width of the negative Gaussian topographic defect (groove) s_0/w for which the height is held constant $s_0 = 1\,\mu$m (blue circles) and width $w = 10\,\mu$m is held constant (orange triangles). The topographic defect $s(y - Ut)$ is defined by equation (4.10a) with $x = 0$. The contact angle is given by $\theta = \theta_0 = 5^o$. The red horizontal line illustrated the critical capillary number for which entrainment occurs on a flat surface, i.e. without defect.

In figure 4.10 the film thickness is plotted versus the capillary number Ca for supercritical substrate velocities $U > U_c$, i.e. liquid entrains. The different data points represent simulations with a flat substrate or with a Gaussian peak with a certain slope. For supercritical substrate velocities the Gaussian peak does not have an influence on the thickness of the entrained film. Thus in this case, small contact angles θ and small capillary numbers $Ca \ll 1$, the film thickness h depends solely on the dip-coating velocity U and liquid properties. This relation is predicted by Landau Levich Derjaguin (equation (2.40)), given by:

$$h = 0.946 \cdot \sqrt{\gamma / (\rho g)} \cdot Ca^{2/3}, \tag{4.13}$$

which is plotted in black in figure 4.10.

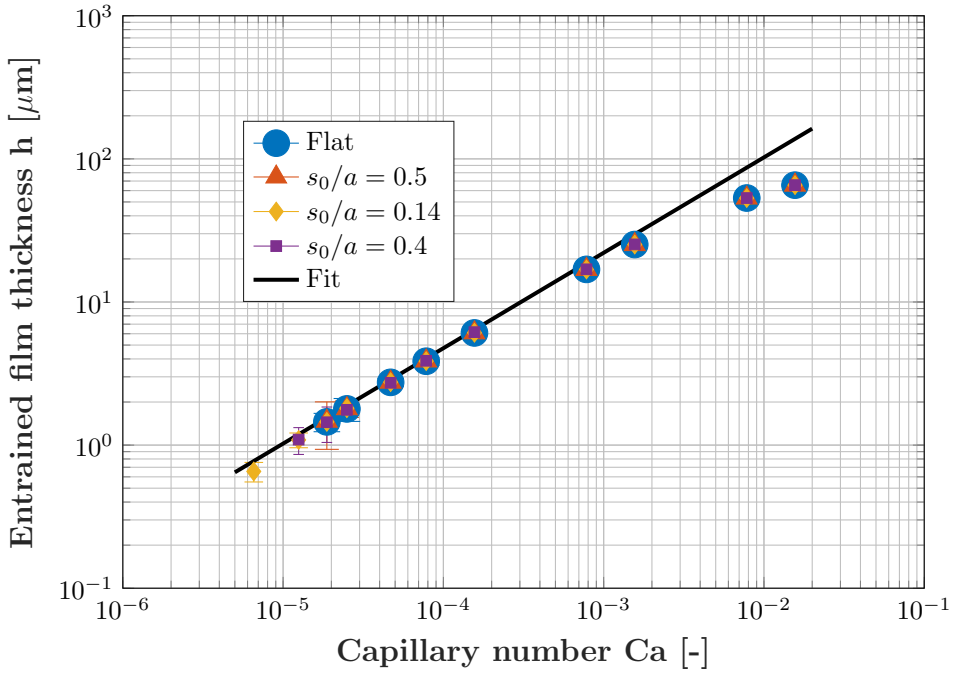

Figure 4.10: Entrained film thickness h as a function of capillary number Ca for supercritical substrate velocities $U > U_c$. The different marks correspond to a flat (blue circle) and Gaussian 1D defect with maximum slopes $s_0/a = 0.5$, 0.14 and 0.4 (orange triangle, yellow diamond and purple square, respectively). The contact angle is given by $\theta = \theta_0 = 5^o$. The black line is given by Landau-Levich Derjaguin (section 2.6), equation (4.13).

4.3 Dip coating of 2D flat defects

In this section the influence of a 2D flat circular defect dip-coated with constant velocity U is studied numerically. Again the effect of the dip-coating velocity U on the break up process and formation of satellite droplets is studied and compared to the experiments. Both topographic only and combined topographic plus chemical defects are considered. In all simulations the substrate contact angle is $\theta_0 = 5^o$. The topographic component, i.e. substrate height distribution, is described by equation (4.10b). The possible chemical component, i.e. contact angle distribution, is described by equation (4.11b). For topographic only defects the contact angle distribution reduces to $\theta(x, y, t) = \theta_0 = 5^o$. The defect parameters are for all 2D simulations given by the defect height $s_0 = 2\,\mu$m, width $a = 100\,\mu$m and transition length $c = 20\,\mu$m.

In figure 4.11 (a-f) snapshots are shown of a typical dip-coating simulation with a relative DC velocity $U/U_c = 0.74$. The defect has both a topographic plus chemical component. While the defect moves through the meniscus liquid places itself in the corners and on top of the defect [figure 4.11(b)]. This way the liquid minimizes its surface energy. The elongated liquid threads, i.e. rivulets, in the corners of the defects eventually breaks up as predicted due to the Rayleigh-Plateau instability [figure 4.11(b-c)]. A liquid bridge is formed, which narrows and elongates in the y-direction as the defect moves further [figure 4.11(c-d)]. When this thinned and elongated liquid bridge or rivulet breaks up the meniscus contact line resembles a sawtooth shape with an unstable rivulet attached [figure 4.11(e)]. A series of satellite droplets is formed at the tip of the unstable rivulet in a sequential, i.e. not simultaneously but one-by-one, fashion [figure 4.11(e-f)]. Finally the sawtooth shape becomes stable again and the meniscus contact line retracts without shedding more satellite droplets. Figure 4.11(g) shows a microscope image of a dip-coating experiment with a pattern dimension $a = 200\,\mu$m and relative DC velocity $U/U_c = 0.77$. Although the simulations are done with for low contact angles, smaller pattern dimension and small slopes many similarities between experimental and numerical satellite

droplets are observed in figures 4.11(f-g).

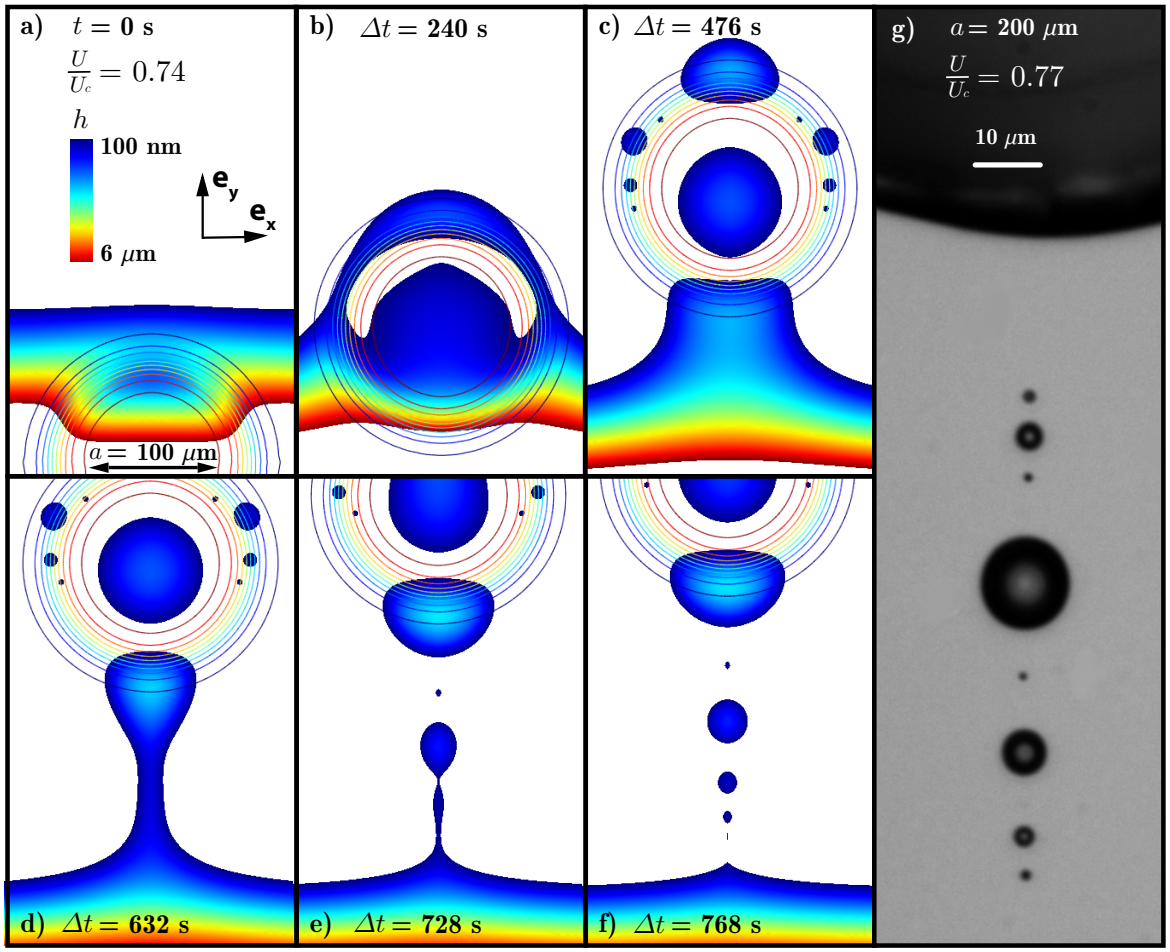

Figure 4.11: (a-f) Numerical simulation illustrating the dip-coating process of a topographic plus chemical defect for defect height $s_0 = 2\,\mu$m, width $a = 100\,\mu$m and transition length $c = 20\,\mu$m. The contact angle is given by $\theta_0 = 5^o$. The relative DC velocity is given by $U/U_c = 0.74$. The defect is illustrated by the contour plot and the film thickness h in color ranging from 100 nm(blue) to 6 μm (red). Time $t = 0$ does not correspond to the beginning of the simulation. (g) Microscope image of satellite droplets formed during dip-coating underneath a topographic and chemical circle defect of pattern dimension $a = 100\,\mu$m at relative DC velocity $U/U_c = 0.77$.

In figure 4.12 the volume of the biggest satellite droplet V is given as a function of dip-coating velocity U non-dimensionalized by the critical DC velocity U. This relative DC velocity U/U_c describes how close to the critical velocity the DC velocity is. The red data corresponds to a topographic plus chemical defect and the blue data to a topographic defect. The data is fitted with a similar power law function as given in the experimental part:

$$V \sim \left(\frac{U}{U_c}\right)^{3p_r}, \tag{4.14}$$

with U/U_c the relative DC velocity and p_r the fit parameter. The factor three is added to be able to directly compare between the experimental and numerical fit parameters ($V \sim r^3$). For a flat surface the critical dip-coating velocity is found to be $U_c = 0.90\,\mu$m/s, which yields a critical capillary number of $Ca_c = 1.41 \cdot 10^{-5}$. For the topographic defect $p_r = 4.6$ and for the topographic plus chemical defect $p_r = 1.89$. For the fit through the topographic plus chemical data the first data point is not taken into account. The scaling behaviour does not directly match when compared to the experimental data. Experimentally for such small pattern dimensions

or defect widths $a < l_c$ power law behaviour ($r \sim U^{0.28}$) was observed for small DC velocities $U/U_c < 0.5$ while for high DC velocities $0.6 < U/U_c < 1$ exponential increase was observed. The differences between experiments and simulations can be attributed to the differences in contact angle, pattern dimension and smaller slopes and capillary number. The simulations are restricted to small slopes and thus small contact angles $\theta_0 = 5^o$, which reduces to $\theta_0/2$ for the chemical component of the defect. The experimental receding contact angles are given by $\theta_{sr,sub} = 71^o$ which reduces to $\theta_{sr,res} = 12^o$ for the resist (defect). The maximum defect slopes in simulations $s_0/c = 0.1$ is slightly smaller compared to the experimental defects $s_0/c \approx 0.2 \pm 0.1$, which can also contribute to the observed differences. This however is hard to draw conclusions from since the experimental defects maximum slopes are possibly determined inaccurately.

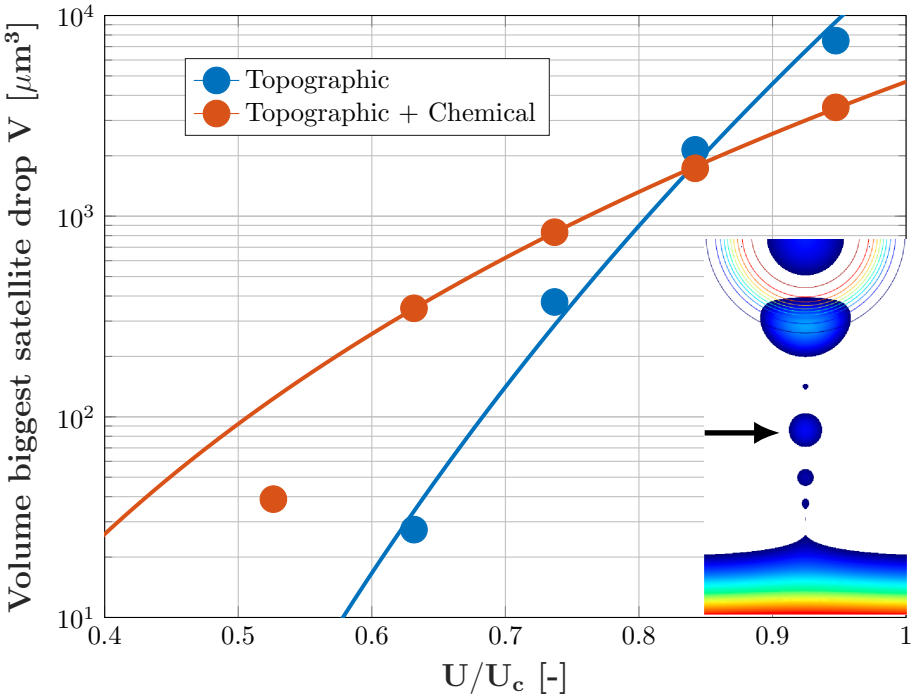

Figure 4.12: Volume of the biggest satellite droplet V versus the relative capillary number U/U_c for a topographic and topographic plus chemical defect. The inset shows a typical simulation where film thickness h is represented in color. The flat defect is illustrated in the top of the inset by the contour plot which moved through the now retracting meniscus (bottom). The flat shaped defects have a width of $a = 100\,\mu$m, transition length of $c = 20\,\mu$m and height of $s_0 = 2\,\mu$m. The contact angle is given by $\theta_0 = 5^o$. The analysed droplet is marked by the arrow.

Figure 4.13 the total volume of the biggest satellite droplets TV is given as a function of the relative DC velocity U/U_c. In all simulations the droplets that contribute less than 1% to the total volume of water-loss TV are neglected. The red data corresponds to a topographic plus chemical defect and the blue data to a topographic defect. The data is again fitted with the power law given by equation (4.14). For the topographic defect $p_r = 4.73$ and for the topographic plus chemical defect $p_r = 2.23$. For the topographic plus chemical the first data point is not taken into account. The fit parameters are roughly equal to the fit parameters for the volume of the biggest satellite droplet data. This means that the volume of the biggest satellite droplet is a reliable estimate of the total volume of water-loss.

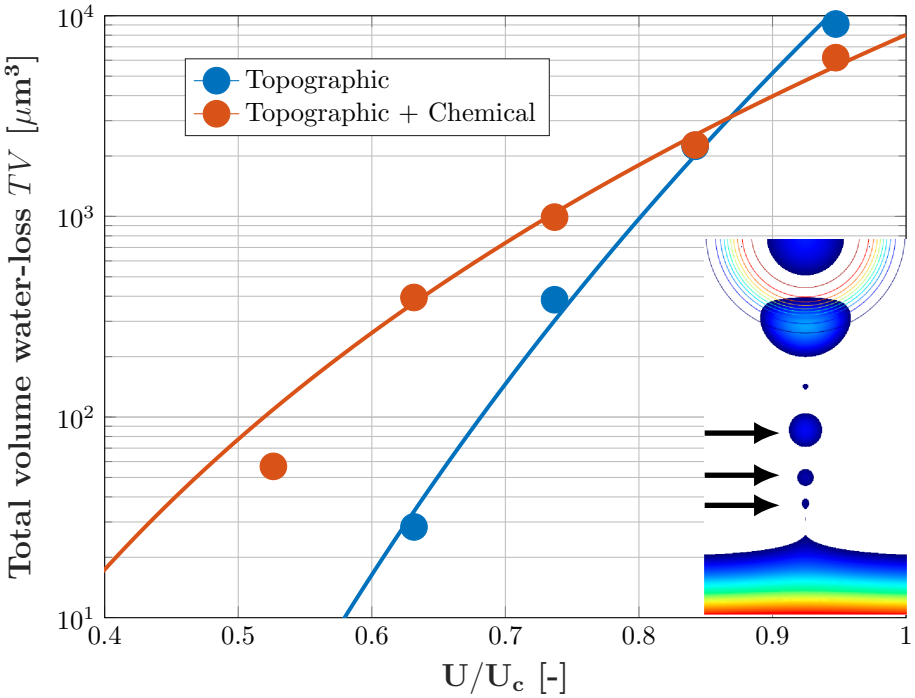

Figure 4.13: Total volume of water-loss TV versus the relative DC velocity U/U_c for a topographic and topographic plus chemical defect. The inset shows a typical simulation where film thickness is represented in color. The flat defect is illustrated in the top of the inset by the contrast plot which moved through the now retracting meniscus (bottom). The flat shaped defects have a width of $a = 100\,\mu$m, transition length of $c = 20\,\mu$m and height of $s_0 = 2\,\mu$m. The contact angle is given by $\theta_0 = 5^o$. The analysed droplets are marked by the arrow. In all simulations the droplets that contribute less than 1% to the total volume of water-loss TV are neglected. Only satellite droplets not attached to the defect itself are analysed.

Figure 4.14 shows the decay in droplet volume as a function of the droplet index N for different relative DC velocities U/U_c for both a topographic plus chemical defect (a) and topographic defect (b). In figure 4.13 the sum of these droplets for each relative DC velocity is added and plotted as the total volume of water-loss. Only the satellite droplets not attached to the defect itself are analysed. The fits resemble a power law given by:

$$V \sim N^{-3p'}, \tag{4.15}$$

with p' the fit parameter. The power law fit parameters are given by $p' = 0.64$, 0.96, 1.11 and 1.16 from closest to the critical DC velocity $U/U_c = 0.95$ to $U/U_c = 0.63$ for the topographic plus chemical defect. For the topographic defect the fit parameter is given by $p' = 0.85$ for the highest DC velocity $U/U_c = 0.95$. Thus an increase in scaling magnitude is observed for decreasing dip-coating velocities. Also the topographic defect satellite droplets have a higher scaling magnitude, i.e. faster decay, compared to the topographic plus chemical defect satellite droplets. For the topographic defect simulation with relative DC velocity $U/U_c = 0.53$ no satellite droplet was observed.

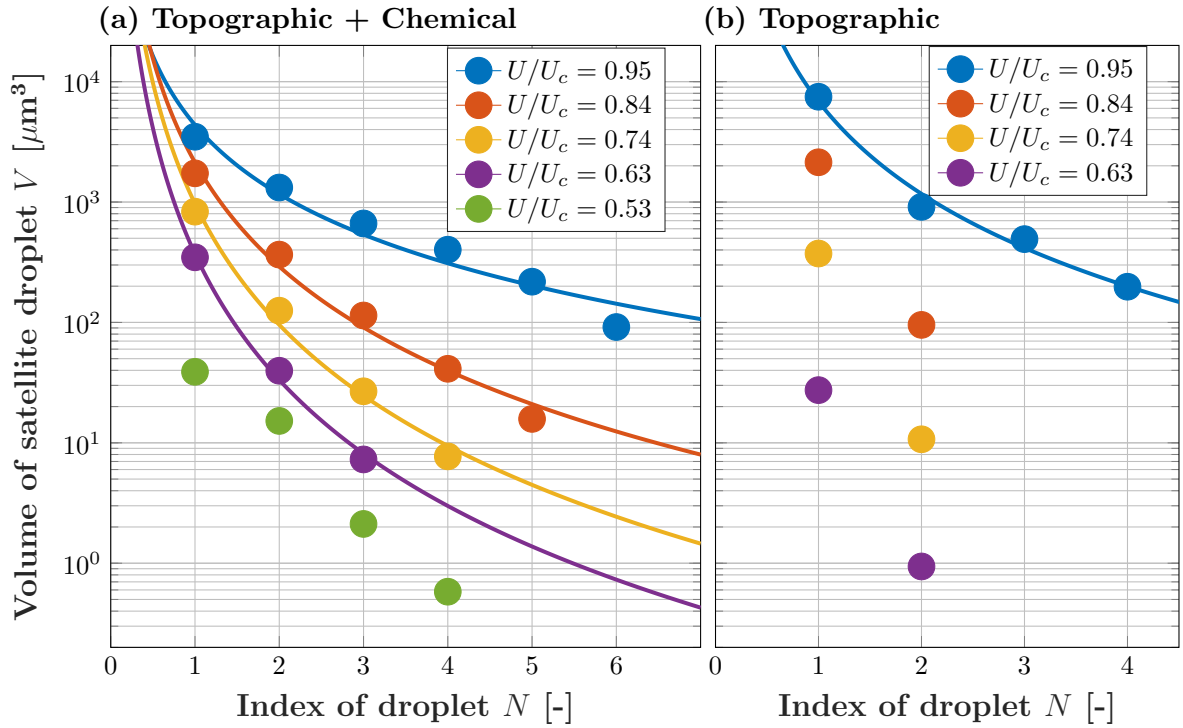

Figure 4.14: Volume of satellite droplet V as a function of the droplet index N for both topographic plus chemical defects (a) and topographic only defects (b). The flat dip-coated defects have a width of $a = 100\,\mu$m, transition length $c = 20\,\mu$m and height of $s_0 = 2\,\mu$m. The contact angle is given by $\theta_0 = 5^o$. In all simulations the droplets that contribute less than 1% to the total volume of water-loss TV are neglected. Only satellite droplets not attached to the defect itself are analysed. The power law fit parameters are given by $p' = 0.64$, 0.96, 1.11 and 1.16 from closest to the critical DC velocity $U/U_c = 0.95$ to $U/U_c = 0.63$ for the topographic plus chemical defect. For the topographic defect the fit parameter is given by $p' = 0.85$ for the highest DC velocity $U/U_c = 0.95$.

In figure 4.15 the distance of the biggest satellite droplet d is given as a function of relative DC velocity U/U_c. This distance is defined by the center-to-center distance of the satellite droplet and defect. The red data corresponds to a topographic plus chemical defect and the blue data to a topographic defect. The data is fitted with a similar power law function given in the experimental part:

$$d \sim \left(\frac{U}{U_c}\right)^{p_d}, \tag{4.16}$$

with q the fit parameter. For the topographic defect $p_d = 0.75$ and for the topographic plus chemical defect $p_d = 1.22$. For the fit through the topographic plus chemical data the first data point is not taken into account. Also different behaviour is observed when compared to the experimental data. Experimentally for such small pattern dimensions or defect widths $a < l_c$ power law behaviour $d \sim U^{0.18}$ was observed for small DC velocities $U/U_c < 0.5$ while for high DC velocities $0.5 < U/U_c < 1$ exponential increase is observed. The differences between experiments and simulations can be attributed to the differences in pattern dimensions and contact angles. The simulations are restricted to small slopes and thus small contact angles $\theta_0 = 5^o$, which reduces to $\theta_0/2$ for the chemical component of the defect. The experimental receding contact angles are given by $\theta_{sr,sub} = 71^o$ which reduces to $\theta_{sr,res} = 12^o$ for the resist (defect). The maximum defect slopes in simulations $s_0/c = 0.1$ is slightly smaller compared to the experimental defects $s_0/c \approx 0.2 \pm 0.1$, which can also contribute to the observed differences. This however is hard to draw conclusions from since the experimental defects maximum slopes might be determined inaccurately.

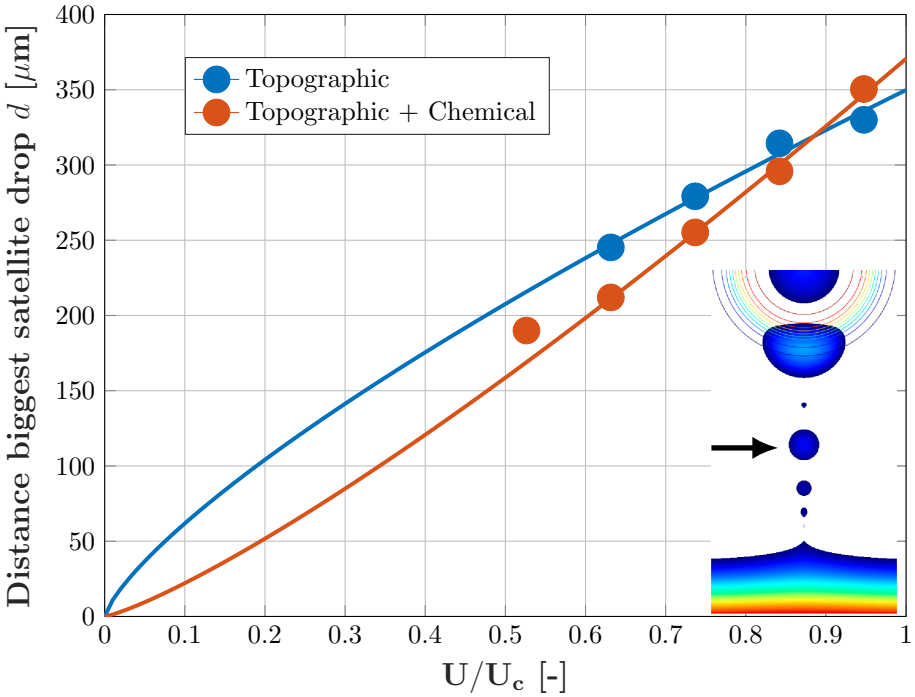

Figure 4.15: Distance of the biggest satellite droplet d versus the relative DC velocity U/U_c for a topographic (blue) and topographic plus chemical (red) defect. The inset shows a typical simulation where film thickness h is represented in color. The flat defect is illustrated in the top of the inset by the contrast plot which moved through the now retracting meniscus (bottom). The flat shaped defects have a width of $a = 100\,\mu$m, transition length of $c = 20\,\mu$m and height of $s_0 = 2\,\mu$m. The contact angle is given by $\theta_0 = 5^o$. The analysed droplet is marked by the arrow. The distance d is defined by the center-to-center distance of satellite droplet and defect.

4.4 Summary and conclusions

In this chapter the dip-coating of defects and formation of satellite droplets is studied numerically.

First the model is validated by showing its results are predicted by the Cox-Voinov and Landau-Levich laws. The influence of the geometrical properties of the defect is studied in a 1D model by varying the width a and height s_0 of a Gaussian shaped defect and identifying the critical velocity. For a Gaussian bump the critical velocity decreases abruptly for a slope around $s_0/a \approx 0.1$. Only the slope of the defect influenced the pinning feature since keeping the slope constant and varying the width and height gives similar critical velocities. The decrease in critical velocities is less distinct for the groove. For the groove the critical velocity does not solely depend on the slope but varies for different widths and slopes. This might be caused by the groove filling up quickly for small widths by the capillary action. These findings are in line with the influence of the geometrical parameters of Gaussian surface defect on a droplet moving down an inclined surface. The slope of the defect only lowers the critical velocities but does not increase the entrained film thickness.

In the 2D dip-coating models simulate the actual dip-coating experiment, i.e. with a 2D heterogeneity on the substrate. Qualitatively for small contact angles the formation and trail of satellite droplets show many similarities with the experiments. However the fitted scaling relations when varying the DC velocity U while analysing the radius and distance of the biggest satellite droplets do not resemble the experimental data. The experiments yield that the radius of the biggest satellite droplet scales with $r \sim U^{0.28}$ for the small pattern dimensions $a \leq 3\,$mm, circular patterns and small DC velocities $0.04 < U/U_c < 0.31$. The simulations yield that

the volume of the biggest satellite droplet scales with $V \sim U^{3 \cdot 1.89}$ for a pattern dimension $a = 100\,\mu$m and DC velocities $0.6 < U/Uc < 1$. In a similar fashion scales the distance of the biggest satellite droplet experimentally with $d \sim U^{0.18}$ for the small pattern dimensions $a \leq 3\,$mm, circular patterns and small DC velocities $0.04 < U/U_c < 0.31$. The simulations yield that the distance of the biggest satellite droplet scales with $d \sim U^{1.22}$ for a pattern dimension $a = 100\,\mu$m and DC velocities $0.6 < U/Uc < 1$. The difference in scaling could be due to the contact angle difference, the smaller pattern dimensions or slopes in the simulations. For a topographic only defect the volume of the biggest satellite droplet increases in scaling with DC velocity while the distance decreases. The total volume of waterloss shows the same scaling behaviour as the biggest satellite droplet. The volume of the trail of droplets decays via a power law with the exponent increasing in magnitude for decreasing DC velocities.

Chapter 5

Conclusions

Experiments and numerical simulations have been performed to study the formation of satellite droplets under a single heterogeneity or defect on a partially wettable substrate dip-coated from a liquid reservoir. In this chapter the overall conclusions are given and the results of both experiments and numerical work are compared. In section 5.1 an outlook is given.

For all shapes of defects the radius and distance of the biggest satellite droplet roughly scale with the pattern dimension $a^{0.9}$ for pattern dimensions smaller than the capillary length $a < l_c$. For pattern dimensions bigger than the capillary length $a > l_c$ the dependence decreases for smaller DC velocities from roughly $a^{0.9}$ to $a^{0.2}$. Possible causes are the more dominant role of gravitational forces due to which more liquid flows back into the liquid meniscus or the observed retraction back onto the pattern for smaller DC velocities. The effect of pattern dimension is studied only experimentally.

Experimentally for all shapes the radius and distance scale roughly with $U^{0.2}$ for smaller pattern dimensions $0.2 < a < 6\,\text{mm}$ and small DC velocities $U/U_c < 0.4$. Closer to the critical DC velocity $0.4 < U/Uc < 1$ the radius and distance roughly scale with $e^{0.14U}$. Numerically a 2D model based on the lubrication equation with a disjoining pressure component to regulate the moving contact line is used to simulate the dip-coating of circular defects with pattern dimension $a = 0.1\,\text{mm}$. The simulations and experimental dynamics of the break-up show many similarities. The volume of the biggest satellite droplet scales with $U^{3 \cdot 1.89}$ for a topographic plus chemical and with $U^{3 \cdot 4.6}$ for a topographic only defect close to the critical DC velocity $0.6 < U/Uc < 1$. The difference in scaling could be caused by the difference in pattern dimension, contact angle and smaller slopes and capillary number. In the simulation the contact angle of the substrate $\theta_0 = 5^o$ reduces to $\theta_0/2 = 2.5^o$ on the defect while in the experiments the (static receding) contact angle of the substrate $\theta_{sr,sub} = 71^o$ reduces to $\theta_{sr,pr} = 12^o$. Comparing the effect of the pattern dimension and DC velocity on the formation of the satellite droplets yields that the pattern dimension is the dominant factor.

The influence of the shape of the defect is studied experimentally by comparing between equilateral triangles, squares and circles. Equilateral triangles and square defects leave bigger satellite droplets at a larger distance for the same DC velocities and pattern dimensions than circular defects. Data for triangles and square patterns overlap when plotted versus pattern area A as opposed to the pattern dimension a. Although more research is necessary to conclude on the effect of the shape, the hypothesis is that the pattern area influences the volume of liquid while the shape of the bottom edge of the pattern determines the duration of the liquid bridge break up.

In the experiments the decay of satellite droplet radius in the trail below a circular pattern scales with $r \sim N^{-p'}$ with N the droplet index. The scaling magnitude p' increases from $p' = 1.81$ to 1.94 for $a = 12\,\text{mm}$, and from $p' = 1.61$ to 2.39 for $a = 0.8\,\text{mm}$ for decreasing DC velocities $U/Uc = [0.92 \rightarrow 0.077]$. Numerically the volume of the satellite droplet decays via $V \sim N^{-3p'}$ where the scaling magnitude p' increases from $p' = 0.64$ to 1.16 for decreasing DC velocities $U/U_c = [0.95 \rightarrow 0.5]$. The size of the biggest satellite droplet scales similar with the DC velocity when compared to the total waterloss of the trail of droplets. This means that the analysis of the biggest satellite droplet is a good indication of the total waterloss.

Numerically a 1D dip-coating model is used to study the influence of the geometrical properties of a Gaussian defect with height s_0, width a and slope s_0/a on the contact line pinning. For a bump the critical velocity decreases abruptly for a slope around $s_0/a \approx 0.1$. Only the slope of the defect influenced the pinning feature since keeping the slope constant and varying the width and height gave similar critical velocities. For the Gaussian groove also a decrease in critical velocity is observed but less distinct compared to the Gaussian bump. The Gaussian defect has no influence on the thickness of the pulled film.

5.1 Outlook

There are many opportunities for future research. For instance in immersion lithography water is used and besides high velocities also high accelerations of the wafer have an effect on the meniscus stability. In both cases the inertial effects play a more dominant role which is not taken into account in this study. To incorporate higher Reynolds numbers in the numerical model, it is possible to implement an extra term for the inertial effects in the lubrication equation. Experimentally this is more difficult since either a change of liquid or a translation stage which accurately operates at higher velocities and accelerations is necessary. Another feature in immersion lithography is the use of airflow to thin the pulled film and improve meniscus stability. This effect could be studied both experimentally and numerically. Experimentally by including an array of gas jets perpendicular to the sample surface. And numerically by decoupling the air jets and dip-coating. The pressure and shear stress distribution could then be implemented on the liquid-air interface.

Another promising non-intrusive technique to measure the film thickness in real time is by use of fluorescence. A light source illuminates a liquid with a fluorescent dye as solute. The captured intensity of the light then gives the local film thickness.

So far the influence of a single defect has been studied but also the influence of multiple defects is interesting, as illustrated in figure 5.1(a). What is the minimum spacing b between defects to have an effect on the critical velocity? Figures 5.1(b-e) show snapshots of a dip-coating simulation with pattern dimension $a = 100\,\mu\text{m}$ and spacing $b = 150\,\mu\text{m}$ where film pulling or entrainment occurs for a sub-critical dip-coating velocity due to the array of defects.

To elucidate the formation of the satellite droplets is most dominantly influenced by the pattern dimension, also the viscosity of the liquid can be varied.

An interesting phenomenon was observed during the dip-coating experiments, which is illustrated by the snapshots in figure 5.2. Just before the square pattern of pattern dimension $a = 2\,\text{mm}$ moves through the meniscus with DC velocity $U/U_c = 0.95$ the contact line retracts locally. No clear explanation is yet available for this phenomenon.

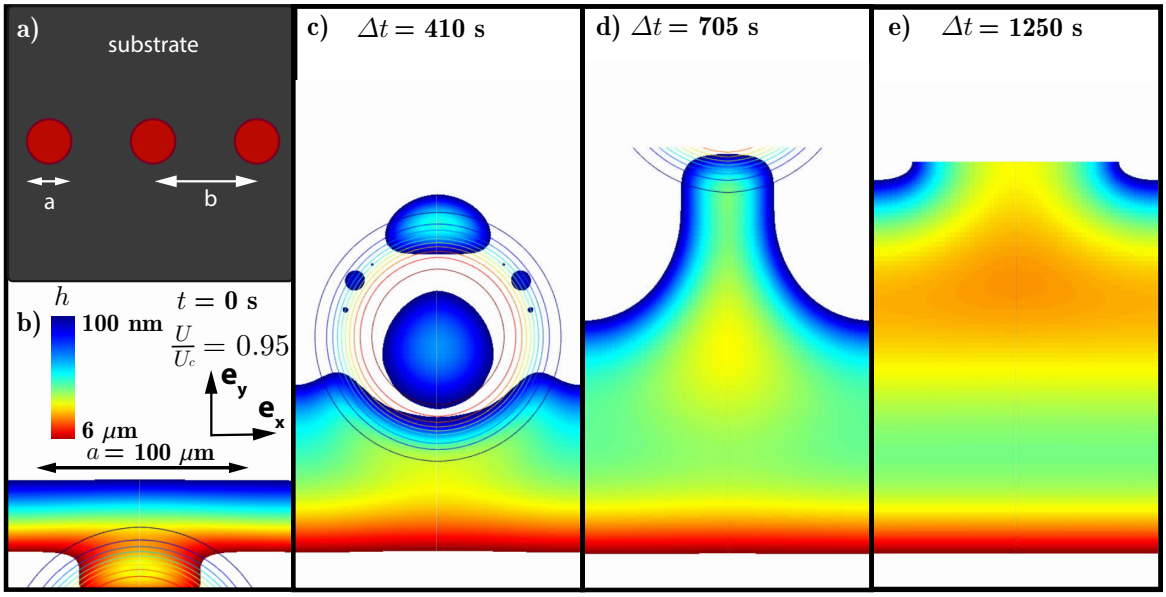

Figure 5.1: (a) Illustration on array of defects on a substrate with pattern dimension a and spacing b. (b-e) Snapshots of dip-coating simulation with pattern dimension $a = 100\,\mu$m and $b = 150\,\mu$m showing film pulling or entrainment for a sub-critical dip-coating velocity due to the array of defects. The defects have both a topographic and chemical component. The other relevant parameters are the transition length $c = 20\,\mu$, contact angle $\theta_0 = 5^o$ and defect height $s_0 = 2\,\mu$m.

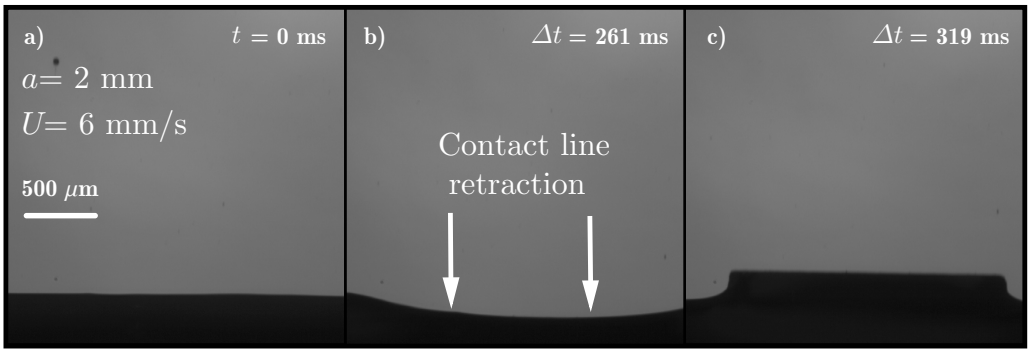

Figure 5.2: Snapshots of contact line retraction observed in experiments.

Appendices

Appendix A

Error analysis

In this appendix the relevant error analyses are presented where the error propagation, errors in average measurements and fitting procedures are described [51].

A.1 Error propagation

When calculating physical quantity (for example the surface tension γ) through a measured physical quantity the measurement error needs to be included in the result. Consider a function $f = f(x, y, ...)$ which includes the variables $x, y, ...$ with measured errors $\Delta x, \Delta y, ...$ The standard deviation in f is then given by:

$$\Delta f = \sqrt{\left(\frac{\partial f}{\partial x}\Delta x\right)^2 + \left(\frac{\partial f}{\partial y}\Delta y\right)^2 + ...}, \tag{A.1}$$

with Δf the standard deviation in f.

A.2 Errors in average measurements

Experimental results such as the radius and distance of the biggest satellite droplet, are presented as a mean value $\bar{x}$ of a N observations given by:

$$\bar{x} = \frac{1}{N}\sum_{i=1}^{N} x_i. \tag{A.2}$$

The error in this mean is given by the standard deviation σ defined by:

$$\sigma = \sqrt{\frac{1}{N-1}\sum_{i=1}^{N} |x_i - \bar{x}|^2}. \tag{A.3}$$

A.3 Least-squares fitting procedure

Experimental measurements are sometimes analysed by a fit function to quantitatively describe the relation between independent x_i and dependent,i.e. measured, variables y_i. Consider the function $f(x_i, z_i)$ describing a set of n data points, where z_i correspond to the m unknown

parameters. To find the set of unknown parameters z_i, for which f best describes or fits the given data points, the sum of squared residuals has to be minimized:

$$SS = \sum_{i=1}^{n} R_i^2, \tag{A.4}$$

with $R_i = y_i - f(x_i, z_i)$ the residuals. Finding the best fit requires an iterative procedure where the initial parameters z_i are guessed and improved while keeping track of the residuals. All fitting procedures are done with MATLAB.

Appendix B

Sample manufacturing recipe

B.1 General information

- Always wear (clean) gloves and keep sample in the sample-box as much as possible to protect the sample from contamination.
- Preferred way of moving sample from the sample-box to setup is with gloves touching the side of the sample (preferred over a tweezer which touches the clean surface of the sample).
- Preferred way of cleaning sample is with clean water to rinse first. Then keep it wet and lie the sample down on a clean paper towel. Blow the water from the middle of the sample top down with the nitrogen jet.

B.2 Spin coating

(i) Turn on vacuum pump (green knob on the ground), spin coating machine (I 0 knob), heat supplier and wait till ready (Spin coating machine takes 1 minute, heat supply 10 minutes).

(ii) Prepare sample for spin coating

  (a) First rinse the sample with the ultra-clean water to remove a possible coating from the manufacturer.

  (b) Blow the water off with some compressed air (do not hold sample too close to the blower because the air is dirty), and to get rid of the last small droplets bake (on heat element of 110^{o}C) the sample (90s should be enough to evaporate).

  (c) Let the sample cool down to room temperature before putting it in the spin coating machine. Possibly by blowing air on the bottom side.

(iii) Spin coating machine

  (a) Turn on machine → Run spin process

  (b) Load recipe (best to take 2 steps with first one with small angular acceleration), possibly check with edit details of recipe the steps, (4000 RPM 60s).

  (c) Center the sample; 'vacuum hold' → 'start center' → 'release' → displace sample in spin coating machine → repeat till sample is centred.

  (d) Carefully put photoresist with pipette on the sample.

(e) If lid is closed and substrate is present (indicated by the signs) press 'Start process'.

(iv) Bake sample for 90s at 110^{o}C and check for comets or inhomogeneities in reflections by light

(v) Shut spin coating machine off by turning off spin-coating machine (keep lid open), heating element for baking and vacuum.

B.3 Exposure

(i) Turn on machine (green button on panel), 2 levers for nitrogen (above panel) and check if machine beneath table is also on. Let machine (lamp) warm up for 30m or so.

(ii) Put sample + mask + glass plate (in that order) onto the red drawer to the right.

(iii) Use the lever on the left side to lift the sample (check if it shows contact, otherwise move horizontal lever).

(iv) Push vacuum mask button on the panel.

(v) Push discharge on the machine on the bottom (top right corner).

(vi) Check the time on the bottom right corner (38 seconds) and press exposure.

(vii) When finished turn off machine and 2 levers for nitrogen (possibly after 10-20m or so).

B.4 Development

(i) Put on heater at 115 ^{o}C.

(ii) Make sure there are 3 reservoirs filled with 1. Pure developer 2. 1:10 diluted with distilled water developer 3. Big one with distilled water. Developer solution can be found in yellow drawer beneath ventilation shaft on other side of the room (AR300-26).

(iii) Put sample in diluted developer solution until you see the exposed photoresist rinsed off. Then wait for 5-10s more and pull it out.

(iv) Clean sample in big distilled water reservoir.

(v) After this blow the residual liquid off and bake the sample in 115^{o}C for $\sim$90s. This is to make sure the photoresist adheres to the substrate again.

B.5 UV Cleaner

(i) Open drawer, turn on machine and put sample in

(ii) Enter time (15m).

(iii) Press start; will actually start by lifting drawer up until sign (white led) switches on.

B.6 PFOTS layer

To make the sample hydrophobic again.

(i) This step is done inside the nitrogen glass box because otherwise the PFOTS will polymerize due to reactions with water damp. Put heater on (115 ^{o}C).

(ii) Put left glove on and give sample with right hand inside the box. Let sample in sample-box acclimate for 15 minutes (remove sample-box lid).

(iii) Open the PFOTS (make sure no metal touches PFOTS), put sample in and close lid.

(iv) After 120 min open again and get sample out.

(v) Briefly (10s or so) put sample in Hexon to remove all the residual PFOTS not attached to the surface. Again use plastic tweezers and close lid on PFOTS.

(vi) Check if sample shows polymerization (white stuff on sample).

(vii) Let sample rest in nitrogen environment for 15m.

(viii) Bake in ventilation shaft heater (115^{o}C for 30s) to get rid of the rest of PFOTS and Hexon.

(ix) Blow nitrogen to clean sample and afterwards put sample in big distilled water (make sure it is fresh since any trace amounts of developer destroys PFOTS layer) and clean again.

Appendix C

Image analysis scripts

First the to be analysed images are loaded in MATLAB where ellipses and lines are drawn to measure the droplet radius and distance from the pattern edge to the middle of the droplet, respectively.

```
%% First load the images in matlab
myfo = 'C:\Users\s106601\Documents\MATLAB\Codes\Testing\Data\
    ↪ UUID018_21Sep_DC_Circles_4\';   % foldername
myfn = '';                                                  % Startfilename
sampleshape = 'Cir';
    ↪                                                                % Shape of
    ↪ sample
samplesize= {'0.6','0.8'}; %,'5','6','7'};                                  %
    ↪ size of sample
samplespeed = {'0.25','0.5','1','2','3','4','5','6'}; %
    ↪                                                  % dip coating speed
zoom = {'1.25','2.5','5','10','20','50','100'};
    ↪                                                          % magnification
    ↪  microscope
repeat = 4;
    ↪                                                                      %
    ↪ repetitions of experiment
con = 1;
    ↪
    ↪ % Number of maximum consectutive images

n= 1;
for i = 1:length(samplesize)
for j = 1:length(samplespeed)
for k = 1:length(zoom)
for l = 1:repeat
for m = 1:con                       % ONly for the extra images
        fullfn = sprintf('%s%s%s_%smm_%smms_Dipcoat_%sx_%d_%d.BMP', myfo, myfn,
            ↪ sampleshape, samplesize{i}, samplespeed{j}, zoom{k}, l, (-m+(con+1)))
            ↪ ;
            if exist(fullfn, 'file')

                if m==1
                    imagedata.image{n} = imread(fullfn);
                    imagedata.path{n} = sprintf('%s%s_%smm_%smmsDipcoat_%sx_%d.%
                        ↪ d.BMP', myfn, sampleshape, samplesize{i}, samplespeed{j},
                        ↪  zoom{k}, l, (-m+(con+1)));
                    imshow(imagedata.image{n})
                elseif m==2
                    imagedata.image2{n} = imread(fullfn);
```

```
                imagedata.path2{n} = sprintf('%s%s_%smm_%smmsDipcoat_%sx_%d.%
                    ↪ d.BMP', myfn, sampleshape, samplesize{i}, samplespeed{j},
                    ↪  zoom{k}, l, (-m+(con+1)));
                imshow(imagedata.image2{n})
            end
        %frame_h = gcf;
        %frame_h.Position = [-1600 0 1600 1000];  % Left extra screen
        %frame_h.Position = [0 0 1600 1000];  % main laptop screen
        imagedata.shape{n} = sampleshape;
        imagedata.size{n} = str2num(samplesize{i});
        imagedata.speed{n} = str2num(samplespeed{j});
        imagedata.zoom{n} = zoom{k};
        imagedata.rep{n} = l;


        d = imline;
        wait1=wait(d);
                if m==1
                    imagedata.line{n}=getPosition(d);
                elseif m==2
                    imagedata.line2{n}=getPosition(d);
                end

        s = imellipse;
        wait2 = wait(s);
                if m==1
                    imagedata.pos{n} = getPosition(s); % xtopleft ytopleft
                        ↪ diamhorizontal diavertical
                elseif m==2
                    imagedata.pos2{n} = getPosition(s);
                end


            if m==1      % After all images of one experiment are quantified
                ↪ move to the next experiment (index)
                n = n+1
            end

        end


end
end
end
end
end
```

Second the analysed images are checked, equivalent radius, distance are computed and these values are converted from pixels to meters via the calibration values.

```
for i = 1:length(imagedata.image)
    if 0 %~isempty(imagedata.image2{i})
        % Check image 2
        imshow(imagedata.image2{i})
        d = imline(gca,imagedata.line2{i});
        wait1=wait(d);
        imagedata.line2{i}=getPosition(d);

        s=imellipse(gca, imagedata.pos2{i});
        wait2=wait(s);
        imagedata.pos2{i}=getPosition(s);
```

```
        % Check image 1
        imshow(imagedata.image{i})
        d = imline(gca,imagedata.line{i});
        wait1=wait(d);
        imagedata.line{i}=getPosition(d);

        s = imellipse(gca, imagedata.pos{i});
        wait2 =wait(s);
        imagedata.pos{i}=getPosition(s);

    else
        % Check image 1 when there is no image 2
        imshow(imagedata.image{i})
        d = imline(gca,imagedata.line{i});
        wait1=wait(d);
        imagedata.line{i}=getPosition(d);

        s = imellipse(gca, imagedata.pos{i});
        wait2 =wait(s);
        imagedata.pos{i}=getPosition(s);
    end

end

%% Calculate the equivalent radius, area and distances and save these in the
    ↪ imagedata structure.
   for n=1:length(imagedata.image)
        if 0 %~isempty(imagedata.line2{n})
            %Compute both distances and add them together in structure entry
            dis(1)=sqrt((imagedata.line{n}(2)-imagedata.line{n}(1))^2+(
                ↪ imagedata.line{n}(4)-imagedata.line{n}(3))^2);
            dis(2)=sqrt((imagedata.line2{n}(2)-imagedata.line2{n}(1))^2+(
                ↪ imagedata.line2{n}(4)-imagedata.line2{n}(3))^2);
            imagedata.dis{n}=dis(1)+dis(2);

            %Compute both areas and add the maximum in the structure array
            AR(1)= pi*imagedata.pos{n}(3)/2 * imagedata.pos{n}(4)/2;
            AR(2)= pi*imagedata.pos2{n}(3)/2 * imagedata.pos2{n}(4)/2;
            imagedata.area{n}=max(AR);
            imagedata.radius{n}=sqrt(max(AR)/pi);

        else
            imagedata.dis{n}=sqrt((imagedata.line{n}(2)-imagedata.line{n}(1))^2+(
                ↪ imagedata.line{n}(4)-imagedata.line{n}(3))^2);
            imagedata.area{n}= pi*imagedata.pos{n}(3)/2 * imagedata.pos{n}(4)/2;
            imagedata.radius{n}=sqrt(imagedata.area{n}/pi);
        end
   end

%%    Convert all the quantities from pixels to meters by using the calibration of
    ↪ the microscope

%meter per pixels for microscope by calibration + errors
% var   m/pixels    magnification
cali(1)=3.733e-6;   % 1.25
cali(2)=0.003e-6;   % 1.25  error
cali(3)=1.859e-6;   % 2.5
cali(4)=0.002e-6;   % 2.5   error
cali(5)=9.279e-7;   % 5
cali(6)=0.001e-6;   % 5     error
cali(7)=4.652e-7;   % 10
cali(8)=0.003e-7;   % 10    error
```

```
cali(9)=2.330e-7;    % 20
cali(10)=0.002e-7;   % 20    error
cali(11)=9.30e-8;    % 50
cali(12)=0.03e-8;    % 50    error
cali(13)=4.65e-8;    % 100
cali(14)=0.02e-8;    % 100   error



% Loop over all experiments to change all data
for i=1:length(imagedata.image)
    if str2num(imagedata.zoom{i})==1.25
      imagedata.fdis{i}(1)=imagedata.dis{i}*cali(1);         % distance in meters
      imagedata.fdis{i}(2)=imagedata.dis{i}*cali(2);         % distance error
      imagedata.farea{i}(1)=imagedata.area{1}*cali(1)^2;     % area in meters^2
      imagedata.farea{i}(2)=imagedata.area{1}*cali(2)^2;     % area error
      imagedata.fradius{i}(1)=imagedata.radius{i}*cali(1);   % radius in meters
      imagedata.fradius{i}(2)=imagedata.radius{i}*cali(2);   % radius error
    elseif str2num(imagedata.zoom{i})==2.5
      imagedata.fdis{i}(1)=imagedata.dis{i}*cali(3);         % distance in meters
      imagedata.fdis{i}(2)=imagedata.dis{i}*cali(4);         % distance error
      imagedata.farea{i}(1)=imagedata.area{1}*cali(3)^2;     % area in meters^2
      imagedata.farea{i}(2)=imagedata.area{1}*cali(4)^2;     % area error
      imagedata.fradius{i}(1)=imagedata.radius{i}*cali(3);   % radius in meters
      imagedata.fradius{i}(2)=imagedata.radius{i}*cali(4);   % radius error
    elseif str2num(imagedata.zoom{i})==5
      imagedata.fdis{i}(1)=imagedata.dis{i}*cali(5);         % distance in meters
      imagedata.fdis{i}(2)=imagedata.dis{i}*cali(6);         % distance error
      imagedata.farea{i}(1)=imagedata.area{1}*cali(5)^2;     % area in meters^2
      imagedata.farea{i}(2)=imagedata.area{1}*cali(6)^2;     % area error
      imagedata.fradius{i}(1)=imagedata.radius{i}*cali(5);   % radius in meters
      imagedata.fradius{i}(2)=imagedata.radius{i}*cali(6);   % radius error
    elseif str2num(imagedata.zoom{i})==10
      imagedata.fdis{i}(1)=imagedata.dis{i}*cali(7);         % distance in meters
      imagedata.fdis{i}(2)=imagedata.dis{i}*cali(8);         % distance error
      imagedata.farea{i}(1)=imagedata.area{1}*cali(7)^2;     % area in meters^2
      imagedata.farea{i}(2)=imagedata.area{1}*cali(8)^2;     % area error
      imagedata.fradius{i}(1)=imagedata.radius{i}*cali(7);   % radius in meters
      imagedata.fradius{i}(2)=imagedata.radius{i}*cali(8);   % radius error
    elseif str2num(imagedata.zoom{i})==20
      imagedata.fdis{i}(1)=imagedata.dis{i}*cali(9);         % distance in meters
      imagedata.fdis{i}(2)=imagedata.dis{i}*cali(10);         % distance error
      imagedata.farea{i}(1)=imagedata.area{1}*cali(9)^2;     % area in meters^2
      imagedata.farea{i}(2)=imagedata.area{1}*cali(10)^2;     % area error
      imagedata.fradius{i}(1)=imagedata.radius{i}*cali(9);   % radius in meters
      imagedata.fradius{i}(2)=imagedata.radius{i}*cali(10);   % radius error
    elseif str2num(imagedata.zoom{i})==50
      imagedata.fdis{i}(1)=imagedata.dis{i}*cali(11);         % distance in meters
      imagedata.fdis{i}(2)=imagedata.dis{i}*cali(12);         % distance error
      imagedata.farea{i}(1)=imagedata.area{1}*cali(11)^2;     % area in meters^2
      imagedata.farea{i}(2)=imagedata.area{1}*cali(12)^2;     % area error
      imagedata.fradius{i}(1)=imagedata.radius{i}*cali(11);   % radius in meters
      imagedata.fradius{i}(2)=imagedata.radius{i}*cali(12);   % radius error
    elseif str2num(imagedata.zoom{i})==100
      imagedata.fdis{i}(1)=imagedata.dis{i}*cali(13);         % distance in meters
      imagedata.fdis{i}(2)=imagedata.dis{i}*cali(14);         % distance error
      imagedata.farea{i}(1)=imagedata.area{1}*cali(13)^2;     % area in meters^2
      imagedata.farea{i}(2)=imagedata.area{1}*cali(14)^2;     % area error
      imagedata.fradius{i}(1)=imagedata.radius{i}*cali(13);   % radius in meters
      imagedata.fradius{i}(2)=imagedata.radius{i}*cali(14);   % radius error
   end
```

```
end
```

After this the data is exported and saved in a file. For each plot this file is opened, the data is sorted and then plotted.

Appendix D

Die-coating of Gaussian bumps

In the 2D COMSOL models the experiments are complemented by moving an axisymmetric Gaussian defect through the predefined meniscus. The Gaussian peak is both an topographic and chemical defect since also the contact angle $\theta(x, y - Ut)$ decreases to $\theta = 2.5°$ to simulate the experiments.

In figure D.1 the radius of the biggest satellite drop R is plotted versus the substrate velocity U.

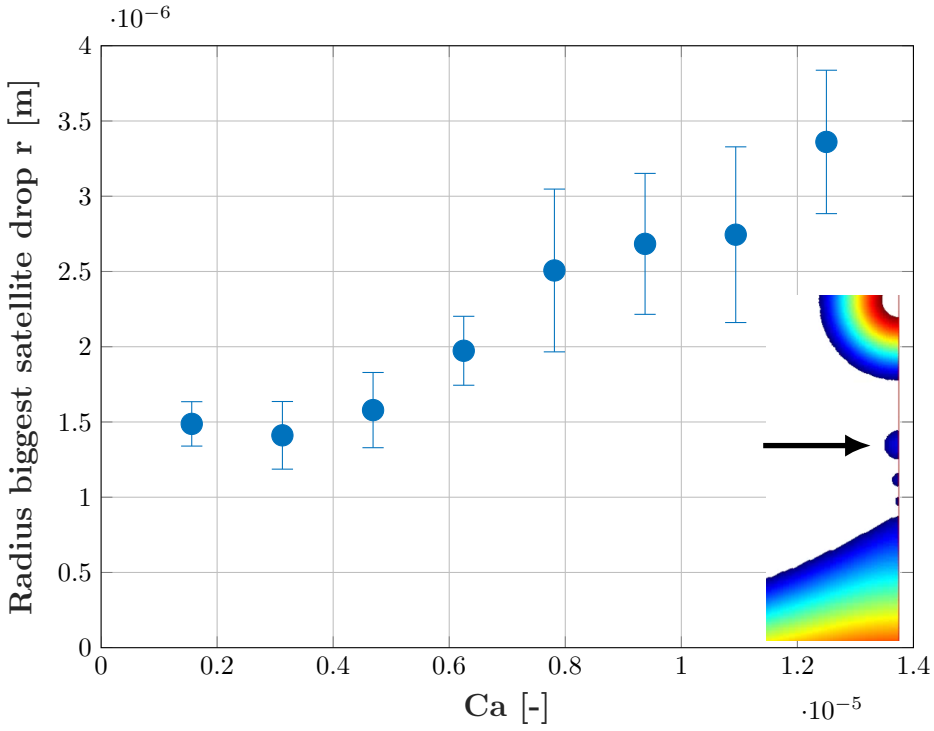

Figure D.1: Radius of the biggest satellite droplet d versus the substrate velocity U. The inset shows a typical simulation where film thickness is represented in color. The top shows the Gaussian shaped defect which moved through the now retracting meniscus (bottom). The Gaussian shaped defect has a width of $w = 10$ μm and height of $s_0 = 1$ μm. The analysed droplet is marked by the arrow.

In figure D.2 the distance of the biggest satellite droplet d is plotted versus the substrate velocity U.

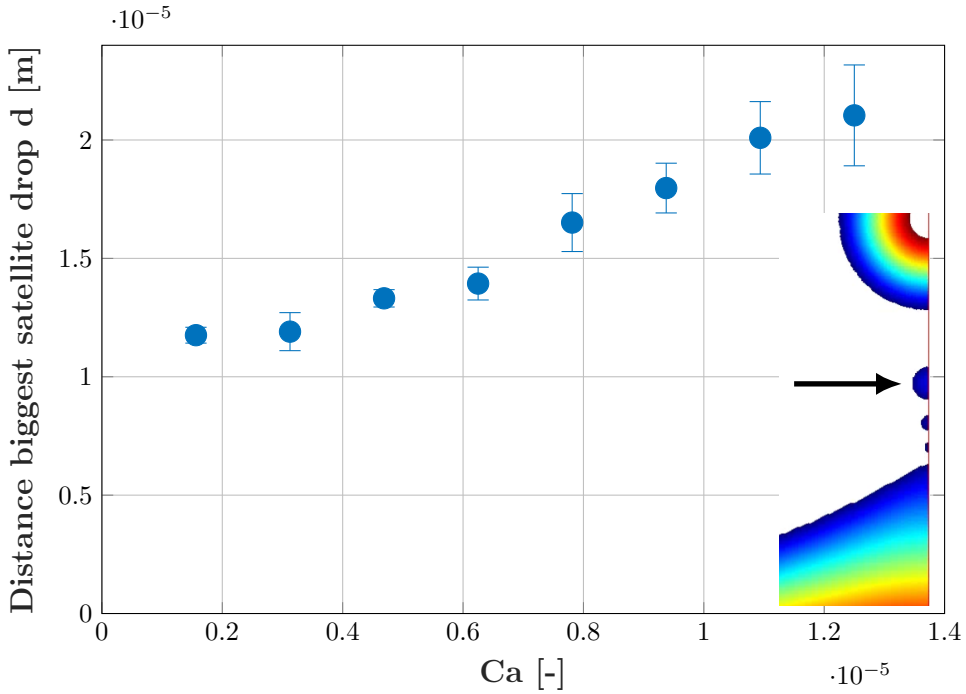

Figure D.2: Distance of the biggest satellite droplet d versus the substrate velocity U. The inset shows a typical simulation where film thickness is represented color. The top shows the Gaussian shaped defect which moved through the now retracting meniscus (bottom). The Gaussian shaped defect has a width of $w = 10$ μm and height of $s_0 = 1$ μm. The analysed droplet is marked by the arrow.

Bibliography

[1] G. E. Moore, "Cramming more components onto integrated circuits", *Proceedings of the IEEE*, vol. 86, no. 1, pp. 82–85, 1998.

[2] B. Disco, C. van der Meulen, *Getting New Technologies Together: Studies in Making sociotechnical Order*. 1998.

[3] K. Winkels, "Fast contact line motion: Fundamentals and applications", PhD thesis, 2013.

[4] H. Xiao, *Introduction to Semiconductor Manufacturing Technology*, 2nd. SPIE, 2012.

[5] C. Wagner and N. Harned, "EUV lithography: Lithography gets extreme", *Nature Photonics*, 2010.

[6] C. Mack, *Fundamental Principles of Optical Lithography: The Science of Microfabrication*. 2007.

[7] S. Owa and H. Nagasaka, "Advantage and feasibility of immersion lithography", *Journal of Microlithography, Microfabrication, and Microsystems*, 2004.

[8] B. J. Lin, "Immersion lithography and its impact on semiconductor manufacturing", *Journal of Micro/Nanolithography, MEMS, and MOEMS*, 2004.

[9] Y. Wei and R. L. Brainard, *Advanced Processes for 193-nm Immersion Lithography*. 2009.

[10] B. J. Lin, *Making lithography work for the 7-nm node and beyond in overlay accuracy, resolution, defect, and cost*, 2015.

[11] T. Takahashi, B. Shimura, S. Kawasaki, "Transfer mechanism of defects on topcoat to resist pattern in immersion lithography process and effects on etching process", *Proc. SPIE 6519, Advances in Resist Materials and Processing Technology*, vol. XXIV, 2007.

[12] S. K. Oh, J. Y. Kim, Y. H. Jung, J. W. Lee, D. B. Kim, J Kim, G. S. Lee, S. K. Lee, K. D. Ban, J. C. Jung, C. K. Bok, and S. C. Moon, "Studies on leaching of photoresist components by water", in *Advances in Resist Technology and Processing XXII, Pt 1 and 2*, 2005.

[13] W. Conley, R. J. LeSuer, F. F. Fan, A. J. Bard, C. Taylor, P. Tsiartas, G. Willson, A. Romano, and R. Dammel, "Understanding the photoresist surface-liquid interface for ArF immersion lithography", in *Proceedings of the SPIE, Volume 5753, p. 64-77 (2005).*, 2005.

[14] M. Sado, T. Teratani, H. Fujii, R. Iikawa, and H. Iida, "Influences of water on photoresist surface in immersion lithography technology", *Applied Surface Science*, 2008.

[15] N. Belmiloud, A. H. Tamaddon, P. W. Mertens, and H. Struyf, "Leaching and drying marks on photoresist-coated substrates", *Microelectronic Engineering*, 2014.

[16] M. Switkes, M. Rothschild, T. a. Shedd, H. B. Burnett, and M. S. Yeung, "Bubbles in immersion lithography", *Journal of Vacuum Science & Technology B: Microelectronics and Nanometer Structures*, 2005.

[17] A. Wei, A. Abdo, G. Nellis, R. L. Engelstad, J. Chang, E. G. Lovell, and W. Beckman, "Modeling fluid thermomechanical response for immersion lithography scanning", in *Microelectronic Engineering*, 2004.

[18] H. Burnett, T. Shedd, G. Nellis, M. El-Morsi, R. Engelstad, S. Garoff, and K. Varanasi, "Control of the receding meniscus in immersion lithography", *Journal of Vacuum Science & Technology B: Microelectronics and Nanometer Structures*, vol. 23, no. 6, p. 2611, 2005.

[19] S. Schuetter, T. Shedd, K. Doxtator, G. Nellis, C. V. Peski, A. Grenville, S.-H. Lin, and D. C. Owe-Yang, "Measurements of the dynamic contact angle for conditions relevant to immersion lithography", *Journal of Microlithography, Microfabrication, and Microsystems*, vol. 5, no. 2, p. 023 002, 2006.

[20] X. Fu, Y. Huang, L. Hu, H. Xie, and W. Chen, "Flow behavior control in immersion lithography", *Flow Measurement and Instrumentation*, 2017.

[21] H. Nakagawa, A. Nakamura, H. Dougauchi, M. Shima, S. Kusumoto, and T. Shimokawa, "Improvement of Watermark Defect in Immersion Lithography: Mechanism of Watermark Defect Formation and its Reduction by Using Akaline Soluble Immersion Topcoat", vol. 6153, no. 2006, 61531R–61531R–8, 2006.

[22] B. Chang, C. Yu, D. Lin, J.C.H. Lin, "Watermark defect formation and removal for immersion lithography", *Proc. SPIE 6154, Optical Microlithography XIX*, 2006.

[23] C. Streefkerk, B. Mulkens, J. Moerman, R. Stavenga, M. van der Hoeven, J. Grouwstra, "A dive into clear water: Immersion defect capabilities", *Proceedings Volume 6154, Optical Microlithography XIX*, 2006.

[24] S. D. Schuetter, T. A. Shedd, and G. F. Nellis, "A correlation for predicting film-pulling velocity in immersion lithography", vol. 6, pp. 1–8, 2006.

[25] C. W. Berendsen, J. C. Zeegers, G. C. Kruis, M. Riepen, and A. A. Darhuber, "Rupture of thin liquid films induced by impinging air-jets", *Langmuir*, vol. 28, no. 26, pp. 9977–9985, 2012.

[26] W. Chen, X. Fu, J. Zou, H. Yang, X. Ruan, and G. Gong, "Investigation on the critical velocity for liquid loss in immersion lithography", *Microelectronic Engineering*, vol. 87, no. 5-8, pp. 1070–1073, 2010.

[27] K. G. Winkels, I. R. Peters, F. Evangelista, M. Riepen, A. Daerr, L. Limat, and J. H. Snoeijer, "Receding contact lines: From sliding drops to immersion lithography", *European Physical Journal: Special Topics*, 2011.

[28] A. Gnanappa, E. Gogolides, F. Evangelista, and M. Riepen, "Contact line dynamics of a superhydrophobic surface: Application for immersion lithography", *Microfluidics and Nanofluidics*, 2011.

[29] B. J. Brasjen, A. W. van Cuijk, and A. A. Darhuber, "Dip-coating of chemically patterned surfaces", *Chemical Engineering and Processing: Process Intensification*, 2011.

[30] B. J. Brasjen, H. M. Wedershoven, A. W. van Cuijk, and A. A. Darhuber, "Dip- and die-coating of hydrophilic squares on flat, hydrophobic substrates", *Chemical Engineering Science*, 2017.

[31] J. H. Snoeijer, J. Ziegler, B. Andreotti, M. Fermigier, and J. Eggers, "Thick films of viscous fluid coating a plate withdrawn from a liquid reservoir", *Physical Review Letters*, 2008.

[32] P. K. Kundu, I. M. Cohen, and D. R. Dowling, *Fluid mechanics*. 2012, p. 891.

[33] Y. Pomeau and E. Villermaux, "Two hundred years of capillarity research", *Physics Today*, 2006.

[34] T. Young, "An Essay on the Cohesion of Fluids", *Philosophical Transactions of the Royal Society of London*, 1805.

[35] R. E. Johnson and R. H. Dettre, "Contact Angle Hysteresis. III. Study of an Idealized Heterogeneous Surface", *The Journal of Physical Chemistry*, 1964.

[36] J. H. Snoeijer and B. Andreotti, "Moving Contact Lines: Scales, Regimes, and Dynamical Transitions", *Annual Review of Fluid Mechanics*, 2013.

[37] L. W. Schwartz and R. R. Eley, "Simulation of droplet motion on low-energy and heterogeneous surfaces", *Journal of Colloid and Interface Science*, vol. 202, no. 1, pp. 173–188, 1998.

[38] U. Thiele, M. G. Velarde, K. Neuffer, M. Bestehorn, and Y. Pomeau, "Sliding drops in the diffuse interface model coupled to hydrodynamics", *Physical Review E - Statistical Physics, Plasmas, Fluids, and Related Interdisciplinary Topics*, 2001.

[39] Y. Pomeau and M. G. Velarde, "Film rupture in the diffuse interface model coupled to hydrodynamics", *Physical Review E - Statistical Physics, Plasmas, Fluids, and Related Interdisciplinary Topics*, 2001.

[40] B. Levich, L. Landau, "Dragging of a liquid by a moving plate", *Acta Physicochem*, vol. 17, 42, 1942.

[41] B. Derjaguin, "On the thickness of the liquid film adhering to the walls of a vessel after emptying", *Acta Physicochem*, vol. 20, 349, 1943.

[42] B. Derjaguin, "Thickness of a liquid layer adhering to walls of vessels on their emptying and the theory of photo- and motion picture coating", *Acad. Sci. URSS*, vol. 39:13-16, 1943.

[43] P.-G. de Gennes, F. Brochard-Wyart, and D. Quéré, *Capillarity and Wetting Phenomena*. 2004, p. 292.

[44] L. E. Stillwagon and R. G. Larson, "Fundamentals of topographic substrate leveling", *Journal of Applied Physics*, 1988.

[45] J. Eggers, "Nonlinear dynamics and breakup of free-surface flows", *Reviews of Modern Physics*, 1997. arXiv: `0804.2586`.

[46] G. Ghigliotti, C. Zhou, and J. J. Feng, "Simulations of the breakup of liquid filaments on a partially wetting solid substrate", *Physics of Fluids*, 2013.

[47] J. Park and S. Kumar, "Droplet Sliding on an Inclined Substrate with a Topographical Defect", *Langmuir*, 2017.

[48] Sigma-Aldrich, "Certificate of Analysis Fluka Glycerol 49770", Tech. Rep., 2007.

[49] M. Butt, H. Graf, K. Kappl, *Physics and Chemistry of Interfaces*. Wiley-VCH, 2003.

[50] D. R. Lide, *CRC Handbook of Chemistry and Physics, 84th Edition, 2003-2004*. 2003.

[51] J. R. Taylor, *An Introduction to Error Analysis*. 1997, vol. 101, p. 140.

[52] A. Oron, S. H. Davis, and S. G. Bankoff, "Long-scale evolution of thin liquid films", *Reviews of Modern Physics*, 1997.

[53] L. Champougny, E. Rio, F. Restagno, and B. Scheid, "The break-up of free films pulled out of a pure liquid bath", *Journal of Fluid Mechanics*, 2017.